UNIVERSITY OF CALIFORNIA

Santa Barbara

Development of Arbitrarily Shaped Pulses for Optimization of Pulsed Dipolar Spectroscopy

A dissertation submitted in partial satisfaction of the

requirements for the degree Doctor of Philosophy

in Chemistry

by

Timothy John Keller

Committee in charge:

Professor Rick Dahlquist, Chair

Professor Songi Han

Professor Bernie Kirtman

Professor Mark Sherwin

December 2018

The dissertation of Timothy John Keller is approved.

_____
Songi Han

_____
Bernie Kirtman

_____
Mark Sherwin

_____
Rick Dahlquist, Committee Chair

December 2018

Development of Arbitrarily Shaped Pulses for Optimization of Pulsed Dipolar Spectroscopy

by

Timothy John Keller

ACKNOWLEDGEMENTS

I would like to thank my PI Dr. Songi Han for her dedicated support, guidance, and encouragement throughout my Ph.D. My committee members, Dr. Rick Dahlquist, Dr. Bernie Kirtman, and Dr. Mark Sherwin were helpful in giving me guidance and feedback throughout my advancement to candidacy and Ph.D. work. During my earlier years as a graduate student, I greatly benefited and appreciated the dedicated support of Dr. John Franck who helped particularly with developing my understanding of magnetic resonance instrumentation. In my later graduate student years, Dr. Ilia Kaminker was a great mentor and his expertise in EPR was invaluable in developing my understanding of more complex pulsed EPR experiments. I would also like to mention the entire Han lab including undergraduates, graduate students, post docs, and assistants who were both my friends and colleagues as I worked throughout my Ph.D. In addition, the instrumental support from Ralph Weber and Chuck Hanson at Bruker BioSpin was incredibly helpful. Last but not least, I would like to thank my family. This work could not have been possible without the love and support of my dad, Richard, my mom, Rebecca, and my two sisters, Stephanie and Kirsten.

Curriculum Vitae of Timothy John Keller
December 2018

Education

- BS Chemistry from Saint Cloud State University, May 2011, magna cum laude
- Ph.D. Physical Chemistry from University of California Santa Barbara (2011-2018)

Research Experience and Skills

- Intern for Fluorescence Innovations, Inc. (summer of 2010 and 2011)
- Teaching Assistant for General Chemistry, Biophysical Chemistry, Magnetic Resonance in Biological Systems, and Physical Chemistry

Awards

1.) Colorado Protein Stability Conference Poster Award (2nd place, 2011)
2.) Dean's Fellowship (Fall 2014)
3.) Award for service to Chemistry Department
4.) Rocky Mountain Conference on Magnetic Resonance Poster Award (2015)

Presentations

1) Colorado Protein Stability Conference (2011), poster, "Direct Waveform Recording for High Throughput Time-Resolved Fluorescence Measurements"
2) Rocky Mountain Conference on Magnetic Resonance (2013), poster, "High Fidelity Excitation with a DAC-board based X-band EPR Spectrometer"
3) IDBR NSF Collective IP Conference (2014), poster, "DAC-Board Based X-band EPR Spectrometer with Arbitrary Waveform Control"
4) Rocky Mountain Conference on Magnetic Resonance (2014), talk, "Complementary Overhauser DNP and ESEEM approach to measure surface water dynamics and accessibility"
5) Rocky Mountain Conference on Magnetic Resonance (2015), poster, "ESEEM Study of the Initial Stages of Tau Protein Aggregation" (Poster Award)
6) Rocky Mountain Conference on Magnetic Resonance (2016), talk, "Optimization of Pulsed EPR Distance Measurements for Tau Protein Aggregation"
7) International Society of Magnetic Resonance Conference (2017), poster, "Study of Aggregation of Intrinsically Disordered Proteins by Pulsed Dipolar EPR Spectroscopy"

Publications

1.) **T.J. Keller**, T. Kaufmann, J.M. Franck, R.P. Barnes, S.J. Glaser, J.M. Martinis, S. Han. "DAC-board based X-band EPR spectrometer with arbitrary waveform control." *J. Magn. Reson.* **235** (2013) 95-108. (audioslides presentation available)
2.) R. Barnes, J.M. Franck., **T.J. Keller**, S. Han. "Active Cancellation - A Means to Zero Dead-Time Pulse EPR" *J. Magn. Reson.* 261 (2015) 199-204.
3.) J.H. Ortony, B. Qiao, C.J. Newcomb, **T.J. Keller**, L.C. Palmer, E. Deiss-Yehiely, M.O. Cruz, S. Han, S.I. Stupp, "Water Dyamics from the Surface to the Interior of a Supramolecular Nanostructure" *J. Am. Chem. Soc.*, 139 (2017) 8915-8921.
4.) Y. Fichou, N.A. Eschmann, **T.J. Keller**, S. Han, "Chapter 5 - Conformation-based assay of tau protein aggregation", *Methods Cell Biol.* 141 (2017) 89-112.
5.) A.M. Schrader, J.I. Monroe, R. Sheil, H.A. Dobbs, **T.J. Keller**, Y. Li, S. Jain, M.S. Shell, J.N. Israelachvili, S. Han, "Hydration and chemical heterogeneity of silica surfaces: a hydration dynamics, surfaces forces, and simulation study", *Proc. Natl. Acad. Sci.* 115 (2018) 2890-2895.

ABSTRACT

Development of Arbitrarily Shaped Pulses for Optimization of Pulsed Dipolar Spectroscopy

by

Timothy John Keller

Pulsed dipolar EPR spectroscopy offers the ability to measure distances between spin labels in the 1-8 nm distance range. The pulsed EPR technique DEER is particularly useful for highly disordered systems where x-ray crystallography and NMR cannot yet be applied. By modeling the dipolar coupling between two spin labels, we can obtain a distance distribution across the biomolecule. The main disadvantage of DEER is that it is common for experiments to require more than 24 hours of averaging to achieve reasonable signal to noise. In this work, we utilize the recent development of high-speed (>1GHz) DAC boards which now operate at high enough frequencies to offer significant performance increases to pulsed EPR experiments. By using shaped microwave pulses instead of rectangular pulses, one can demonstrate (1) dramatically increased excitation bandwidth, (2) increased selectivity of excitation, and (3) calibration of pulses for resonator bandwidth compensation. We demonstrate the performance improvement of arbitrarily shaped pulses for various pulsed EPR applications on a home-build AWG spectrometer as well as commercial spectrometers. In addition, we apply arbitrarily shaped pulses to study tau protein aggregation, which is involved in Alzheimer's disease and particularly difficult to study because of its broad distance distribution and short spin-spin relaxation times. Other methods to offer signal to noise improvements to the DEER experiment including denoising and alternative methods for calculating the distance distribution are investigated.

TABLE OF CONTENTS

Table of Contents

1) Introduction....1

2) Hardware Development and Design of Arbitrary Waveform Generator Based Electron Paramagnetic Resonance Spectrometer 3

a) Historical Perspective 3

b) A New Paradigm - Arbitrary Waveform Generator Based Pulsed EPR Spectrometers 4

c) DAC Based Spectrometer Design Philosophy 6

d) Characterization of SNR....8

e) Calculation of Signal 9

f) Receiver Noise Figure Measurements 11

g) Gain and Noise Figure of Heterodyne Detector 12

h) Expected SNR....15

i) Experimental Signal-to-Noise 15

j) Signal-to-noise comparison with commercial spectrometers 17

k) Suppression of IQ Mixer Leakage 18

l) Characterization of the Microwave Resonator Transfer Function ..20

m) Example of Resonator Transfer Function....23

n) Formal Definition of Transfer Function 24

o) Experimental Determination of Transfer Function....25

p) Calibration of Pulse Shapes – Solid state amplifier (10 W) 25

q) Correcting for the Resonator Transfer Function.....26

r) First and zeroth order phase optimization 29

s) Physical origin of phase offsets 30

t) Experiments with High Power Amplifier (1 kW TWT).....35

u) Development of Software for Home-Built Spectrometer.....40

3) Effect of Bandwidth compensation on pulsed EPR experiments with shaped pulses 43

a) Introduction.....43

b) DEER Theory 45

i) Hamiltonian for weakly coupled electron spins. 45

ii) Pulse Sequence 47

c) SIFTER Theory 49

d) Methods 49

i) Instrument.....49

ii) Materials 50

e) Results.....50

i) Resonator Transfer Function 50

ii) Measurement of Excitation Profiles 54

iii) Broadband Echo Measurements.....58

iv) DEER with Broadband Pulses.....60

v) SIFTER with Broadband Pulses 63

vi) DEER vs SIFTER on realistic samples 67

f) Discussion.....68

g) Conclusion 72

4) Optimization of Q-band DEER Experiments 73

a) Excitation Scheme for Q-band DEER 73

b) Optimization of Tuning Procedure 75

c) Optimization of Pulse Shape 76

d) Reliability of Distance Distributions 78

e) Optimization of protein concentration 79

f) Increasing Maximum Dipolar Evolution Time 80

5) ODNP and ESEEM Water Accessibility Measurements 83

a) Introduction 84

b) Theory 88

i) ODNP 88

ii) ESEEM 90

c) Experimental 94

i) Chemicals 94

ii) Pulsed EPR 94

iii) ODNP 95

d) Results 96

i) ESEEM 96

ii) ODNP 97

e) Discussion 100

f) Conclusions 101

6) Wavelet Denoising and SVD for Improved Pulsed EPR Distance Distributions 103

a) Tikhonov Regularization 103

b) Wavelet Denoising 105

c) Validation of Wavelet Denoising 105

d) Details about background correction 107

e) Introduction to SVD based PICASSO Method 109

f) Conclusion 113

7. Conclusion 114

References 117

LIST OF FIGURES

Figure 2.1 Schematic overview of the pulse forming unit of the AWG system.....7

Figure 2.2 Overview of the AWG pulsed EPR spectrometer.....8

Figure 2.3 Gain for the receiver as a function of frequency.....12

Figure 2.4 Schematic showing block A and block B of the heterodyne detector.....14

Figure 2.5 Comparison of noise level from the TWT and solid state amplifier.....16

Figure 2.6 Signal to noise comparisons for certain experiments.....18

Figure 2.7 Characterization of IQ mixer leakage 19

Figure 2.8 Schematic diagram of the receiver.....20

Figure 2.9 Lumped circuit equivalent of resonator 21

Figure 2.10 Example transfer function distorting the shape of a pulse. 23

Figure 2.11 Example of field sweep to obtain excitation profile 26

Figure 2.12 Excitation profiles for 10 ns square and 50 ns sinc pulses.....27

Figure 2.13 Fourier transforms and observed spin response 29

Figure 2.14 Image plot showing the cost function 33

Figure 2.15 100 ns square pulse after transfer function correction 34

Figure 2.16 Image plot of the data before and after phase optimization 34

Figure 2.17 Oscilloscope trace of pulse from TWT amplifier.....35

Figure 2.18 Excitation profiles for various pulses.....36

Figure 2.19 Off-resonance FID with BDPA standard 37

Figure 2.20 Nutation curve from BDPA standard.....37

Figure 2.21 2-pulse ESEEM data 38

Figure 2.22 3-pulse ESEEM data 39

Figure 2.23 HYSCORE data from AWG system 39

Figure 2.24 HYSCORE data from ELEXSYS 40

Figure 2.25 Example of pulse program used for performing a Hahn echo. 41

Figure 2.26 Graphical User Interface for updating pulse parameters. 42

Figure 3.1 Energy level diagram for two weakly dipolar coupled spins 48

Figure 3.2 Definition of θ and r and angular dependence of ωee 48

Figure 3.3 Pulse sequence for transient nutation experiment 53

Figure 3.4 Adiabatic pulse and the experimental response 57

Figure 3.5 Bohlen Bodenhausen excitation scheme for Hahn echo 60

Figure 3.6 Pulse sequence for 4-pulse DEER experiment 61

Figure 3.7 DEER traces for 2.8 nm standard ruler 63

Figure 3.8 DEER experiment showing calibrated and uncalibrated pulses 66

Figure 3.9 DEER and SIFTER on tau187 G272C S285C 71

Figure 4.1 Q-band field swept echo for typical nitroxide spectrum 74

Figure 4.2 Frequency domain Q-band nitroxide spectrum 74

Figure 4.3 Bruker QT-II resonator transfer function 76

Figure 4.4 Bar graph showing SNR for each tuning procedure 77

Figure 4.5 Pulse shapes chosen for optimization of DEER experiment 77

Figure 4.6 Bar graph showing SNR for various DEER pump pulses 78

Figure 4.7 Maximum dipolar evolution time for distance distribution 79

Figure 4.8 Optimum protein concentration for a desired dipolar evolution time 80

Figure 4.9 Hahn echo decays for difference concentrations of deuterated glycerol ... 81

Figure 4.10 Hahn echo decays for different extent of deuteration 82

Figure 5.1 Pulse sequence for 3-pulse ESEEM measurement.....90

Figure 5.2 Simplified representations of model system 96

Figure 5.3 Fit of spherical shell model.....98

Figure 5.4 Parameter from the ESEEM spherical shell model and ODNP 99

Figure 6.1 Simulated data to demonstrate the inverse problem.....104

Figure 6.2 Tau 272/285 before aggregation 106

Figure 6.3 Tau 272/285 demonstrating the denoising method 107

Figure 6.4 Standard ruler molecule 108

Figure 6.5 Tau protein 272/285 before, after (heparin), and after (seeded) 111

Figure 6.6 Tau protein 351/373 before, after (heparin), and after (seeded) 112

LIST OF TABLES

Table 2.1 Noise figure and noise temperature calculations. 14

Table 2.2 Definition of variables for phase optimization algorithm 32

Table 5.1 ESEEM and ODNP parameters from surfaces 100

1) Introduction

The field of electron paramagnetic resonance (EPR) has remained far less developed than the closely related field of nuclear magnetic resonance (NMR). This is primarily due to technical limitations associated with working at higher frequencies. Electron spins have a magnetic moment approximately 660 times greater than a proton, which makes typical EPR experiments performed in the microwave frequency range and typical NMR experiments performed in the radio frequency range. Many NMR experiments are not practically feasible in EPR despite the two fields being governed by much the same physics. In EPR, we often suffer from insufficient excitation bandwidth and fast relaxation times. In recent years, the development of faster electronics has introduced the potential for arbitrary waveform generation on timescales relevant for pulsed EPR experiments. Shaped pulses offer the ability to excite much broader spectral bandwidth, sharper spectral slices, and much more precisely manipulate spin systems than rectangular pulses of comparable power. The increased bandwidth capabilities of shaped pulses are particularly relevant for pulsed dipolar spectroscopy experiments such as double electron-electron resonance (DEER), single frequency technique for refocusing dipolar couplings (SIFTER), and double quantum coherence (DQC). In addition, shaped pulses enhance the performance and signal to noise of already standard pulsed EPR experiments such as DEER and hyperfine sub-level correlation spectroscopy (HYSCORE). The high amplitude and phase resolution of recent arbitrary waveform generators can also output pulses calibrated for the transfer function of the microwave resonator, so that spins observe the desired pulse instead of the pulse distorted by the resonator transfer function. By compensating for the resonator bandwidth, it is possible to excite spin systems with even higher fidelity.

Pulsed dipolar spectroscopy techniques such as DEER, SIFTER, and DQC offer the ability to measure distances in the 1.5 to 8 nm range. These distances are particularly relevant for measuring the distances across proteins. However, we are strongly limited in signal to noise for the most challenging – and often most interesting – samples which can often require greater than 24 hours of experiment time to acquire even mediocre signal to noise. In such cases, improving the signal to noise by a factor of 2 would dramatically reduce the acquisition time. An example of a system of interest which poses a challenge for DEER is tau protein. Tau protein is an intrinsically disordered protein which form amyloid beta-sheet fibrils characteristic of certain neurodegenerative diseases (e.g. Alzheimer's disease). This protein is especially challenging because of its broad distance distribution and fast relaxation times. For this system we would like to investigate the intermediate states on-route to aggregation to better understand the mechanism behind the formation of amyloid fibrils.

In addition to advancements in hardware and pulse shaping, the method for obtaining a distance distribution can be investigated to increase the reliability of pulsed EPR experiments like DEER. Tikhonov regularization is currently the most common method for obtaining a distance distribution from time-domain pulsed dipolar spectroscopy experiments and it is based on the assumption that the distance distribution is required to be smooth. A new method, which is based on singular value decomposition (SVD) has been termed, Piccard Sliding Scale Optimized (PICASSO) shows potential in obtaining distance distributions without the underlying assumptions made in Tikhonov regularization.

2) Hardware Development and Design of Arbitrary Waveform Generator Based Electron Paramagnetic Resonance Spectrometer

a) Historical Perspective

The first rudimentary microwave spectrometer was built in 1934 by Cleeton and Williams where they were able to measure the inversion of the ammonia molecule. The earlier Stern-Gerlach experiment inspired attempts at measuring the magnetic resonance in solids, but current equipment was not sensitive enough to measure magnetic resonance.[1]

During WWII, the development of microwave radar equipment enabled the widespread availability of microwave sources and components. Technical problems, such as the development of high-power microwave sources and more sensitive detection electronics were solved. To this day, the commonly chosen microwave frequencies for EPR are those developed for purposes of radar. The microwave bands X-band (8-12 GHz), Q-band (33-50 GHz), and W-band (75-110 GHz) were developed because they correspond to dips in the absorption of air and are therefore more useful for long distance radar applications.[2]

The first detection of EPR signal was in 1944 by Yevgeny Zavoisky at Kazan State University in the former Soviet Union on several transition metal salts, including copper chloride ($CuCl_2 \cdot 2H_2O$). The resonance occurred at a magnetic field of 4.76 mT and a frequency of 133 MHz, giving roughly a g-factor of 2. This breakthrough was in large part due to improved detection sensitivity by exchanging calorimetric detection with a diode detector and applying external field modulation. Previous attempts at detection of electron paramagnetic resonance lacked the sensitive electronics necessary to detect signal. This method of detection is remarkably similar to modern field-swept cw-EPR spectrometers

which utilize a lock-in amplifier and modulation coils to modulate the external magnetic field. The modulation of external field dramatically improves the sensitivity of detection by isolating and detecting the signal frequency (eliminating the problem of $1/f$ noise in diode detectors).[3]

The first electron spin echo was measured in 1958 by R.J. Blume using solvated electrons in a sodium and ammonia solution at the freezing point. The first direct detection of time-domain EPR signal was done in 1958 by Gordon and Bowers on donor electrons in silicon. In the 1960's the field of pulsed EPR was greatly developed at Bell laboratories by W.B. Mims, but the initial expense of microwave components prevented the field from expanding.[4]

The field of EPR grew rapidly in the 1970's and 1980's after chemists realized it could be used to investigate physical properties of matter and particularly the local structure around the unpaired electron. To this day the field of EPR continues to grow and has numerous commercial and medical applications including protein structure and dynamics, geological dating, radiometry dosing, detection of short-lived radicals through spin trapping, etc.[5–9]

b) A New Paradigm - Arbitrary Waveform Generator Based Pulsed EPR Spectrometers

Starting from the early 1960's, the general design of a pulsed EPR spectrometer consisted of a continuous wave (cw) microwave source with a microwave switch opening and closing rapidly to form pulses. Fast microwave switches typically have rise-times of 2-4 ns and with high power amplifiers, inversion pulse lengths less than 10 ns can be achieved (120 MHz). As experiments became more complicated and phase cycling[10,11] was desired to

be implemented, pulsed EPR spectrometers consisted of multiple pulse forming units (MPFU). For each individual pulse phase that is desired, a separate channel is required each consisting of a phase shifter, variable attenuator, and microwave switch. For a full 16-step phase cycle with a Hahn echo experiment a total of 4 separate channels was required. There even exist commercial pulsed EPR spectrometers with 8 separate channels to perform DEER with equal length observe pulses.

The recent development of faster electronics, particularly field programmable gate array (FPGA) boards operating in the GHz frequency range, has recently presented an alternative to pulsed EPR spectrometer design. In recent years, fast FPGA boards have been implemented in commercial arbitrary waveform generators (AWG) and enable shaped pulses on a sub-nanosecond resolution. The new AWGs now offer bandwidths and sampling rates large enough to be incorporated into pulsed EPR spectrometers. The incorporation of these AWG units into pulsed EPR spectrometers offers several advantages: (1) dramatically simplified pulse forming unit in spectrometer design[12] (2) broadband excitation far exceeding capabilities with square pulses alone[13–18] (3) highly uniform excitation even in the presence of B_1 inhomogeneities[19,20] (4) selective and or narrowband excitation excitation.[21,22]

The first AWG EPR spectrometers were add-on units to existing spectrometers. These units took an external trigger from the spectrometer and used an external microwave source which was incoherent with the detection source. This limited the application of AWG to wideband inversion applications where phase coherence isn't necessary, for example, double electron-electron resonance (DEER).[13]

c) DAC Based Spectrometer Design Philosophy

The versatility of AWG units allows for a more modern philosophy of spectrometer design. In this work, we demonstrate a stand-alone, home-built, AWG X-band EPR spectrometer designed to precisely manipulate spin systems. A 1 GHz digital-to-analog converter (DAC) board serves as the central control and timing unit of the spectrometer. With this methodology, we completely eliminate the need for multiple pulse forming channels each consisting of a phase shifter, attenuator, and microwave switch. The FPGA based DAC board features a number of trigger outputs, each of which can be programmed independently to control switches, gate amplifiers, and trigger detection electronics.[12]

The overview of our DAC based EPR spectrometer philosophy is shown in Figure 2.1. A microwave IQ mixer is added to replace the microwave switch and the two outputs of the DAC feed into the in-phase and quadrature channels of the mixer. The mixer allows for complete phase and amplitude control over the pulse. Our DAC board is capable of 14-bit (42 dB) amplitude resolution and 0.007° phase resolution. A complete schematic and overview of the spectrometer can be found in Figure 2.2.

The microwave source, a YIG oscillator, outputs 8-10 GHz at 10 dBm which then passes through an 18 dBm preamplifier. Pulses are formed in the IQ mixer. The YIG source is fed into the local oscillator channel, and the two output channels of the DAC are fed into the I and Q channels of the mixer. The RF output of the mixer is pre-amplified again to 14 dBm before going through either a 10 W solid state amplifier, or a 1 kW TWT amplifier. A circulator directs microwave pulses to either a Bruker MD5 dielectric resonator or Bruker MS3 split-ring resonator. The reflected pulses and signal travel back through the circulator to the receiver. The receiver is protected by a limiter which prevents the low noise amplifier

from being damaged by the high-power pulse reflections from the microwave resonator. After the low noise amplifier, the signal travels through another mixer where it is downconverted to < 1 GHz. The signal then is amplified again by video amplifiers and detected with an oscilloscope.[12]

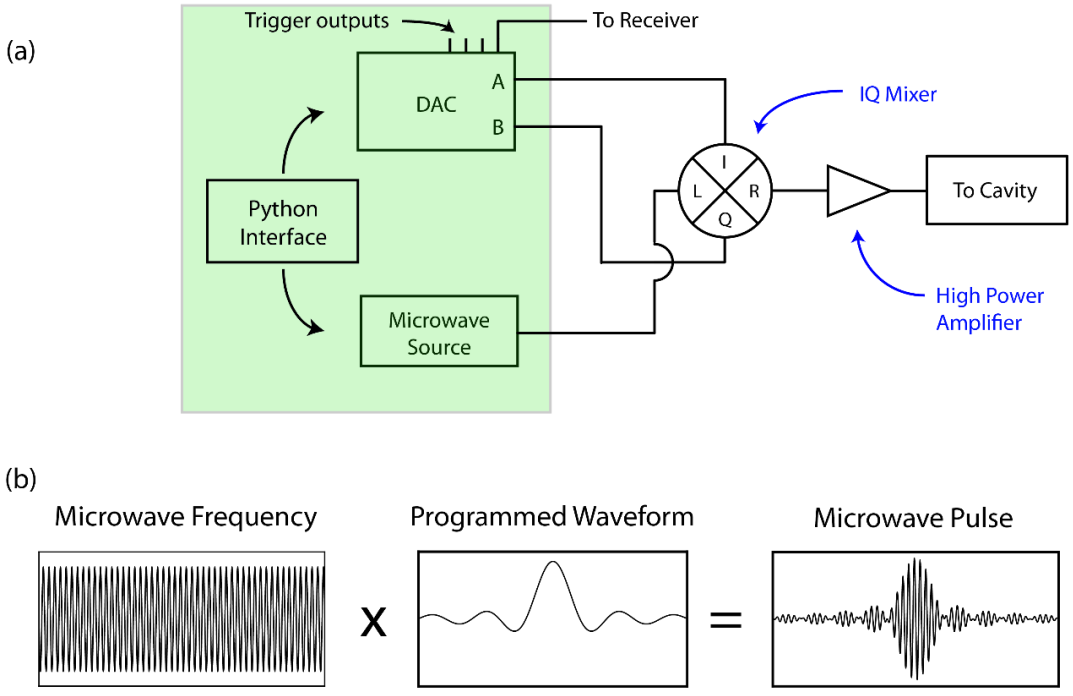

Figure 2.1 (a) Schematic overview of the pulse forming unit of the AWG system. The DAC board outputs two channels of DC-1GHz waveforms which are mixed up to X-band (~9.6GHz) frequencies by an IQ mixer (b) The output of the IQ mixer is a product of the microwave frequency and the shaped waveform.

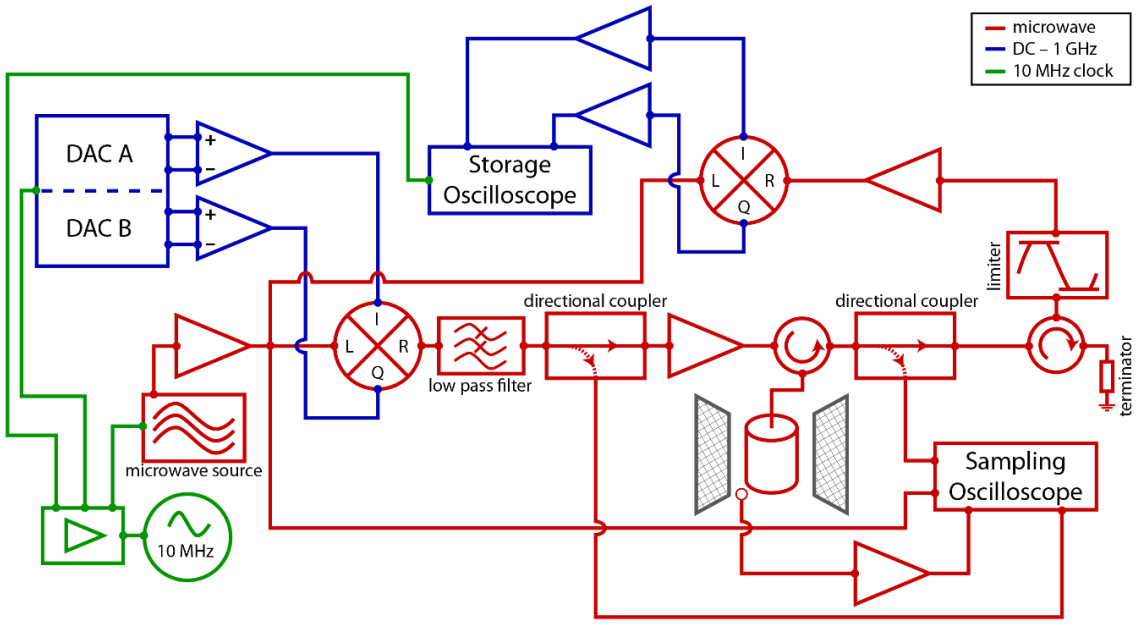

Figure 2.2 Overview of the AWG pulsed EPR spectrometer.[12]

d) Characterization of SNR

All microwave components will have intrinsic thermal-Johnson noise due to statistical fluctuations of charge in conductors which produces random potential fluctuations at the ends of a conductor. The thermal noise power density, P_n, can be calculated from the absolute temperature of the device by:

$$P_n = k_B T \tag{2.1}$$

Calculation of the noise level is less trivial when the noise passes through amplifiers, attenuators, and other components. The noise figure, NF – given in dB – is a commonly specified figure of merit for indicating the signal-to-noise degradation.

$$NF = 10 \log\left(\frac{SNR_{in}}{SNR_{out}}\right) \tag{2.2}$$

However, the noise temperature, T_e, can be more convenient for calculations.

$$T_e = T_0\left(10^{NR/10} - 1\right) \tag{2.3}$$

Where T_0 is the temperature of the device. For any given component, the output noise power density can be calculated from

$$P_n = g k_B (T_0 + T_e) \tag{2.4}$$

Where k_B is Boltzmann's constant and g is the gain of the component. For components in series we can calculate the effective noise temperature of a network by using the Friis' equation:

$$T_{e,total} = T_{e,1} + \frac{T_{e,2}}{g_1} + \cdots + \frac{T_{e,n}}{g_1 g_2 \cdots g_{n-1}} \tag{2.5}$$

Where $T_{e,n}$ is the noise temperature of the nth component in the network, and g_n is its gain. In addition to amplifiers, any lossy component (e.g. an attenuator) also has a noise temperature which is[2]

$$T_e = T_0\left(\frac{1}{g} - 1\right); 0 < g \leq 1 \tag{2.6}$$

e) Calculation of Signal

To calculate the signal intensity, we assume that the pulse completely converts the thermal equilibrium magnetization (M_0) to transverse magnetization, which gives the maximum possible observable signal. The equilibrium magnetization can be calculated from:

$$M_0 = N_0 \frac{\gamma_e^2 \hbar^2 B_0 S(S+1)}{3 k_B T} \tag{2.7}$$

Where N_0 is the number of spins per unit volume, γ is the gyromagnetic ratio, $\hbar$ is Planck's constant divided by 2π, B_0 is the static magnetic field, and S is the spin quantum number which in our case is 1/2 (note that $\gamma_e \hbar = \mu_B g$, where μ_B is the Bohr magneton and g is the electronic g-factor).

The precession of the macroscopy magnetic moment induces a voltage in the resonator, V_E, which can be calculated by integrating over the sample volume

$$V_E = \omega_0 \int_{sample} \vec{M} \cdot \frac{\overrightarrow{B_1}}{I} dV \tag{2.8}$$

Where ω_0 is the Larmor precession frequency, $\vec{M}$ is the magnet moment of the sample, $\overrightarrow{B_1}$ is the magnetic field from the sample, I is the induced current, and V is the sample volume.

Assuming that the induced field, B_1, is orthogonal to the magnetic moment of the spins and uniform over the sample volume, the signal voltage is:

$$V_E = \omega_0 \frac{B_1}{I} V_{sample} \tag{2.9}$$

By definition, the conversion factor of a critically coupled (matched) resonator, $C_{critical}$ is

$$C_{critical} = \frac{B_1}{\sqrt{P}} \tag{2.10}$$

Where P is the power incident on the cavity, so that

$$C_{critical} = \frac{B_1}{I\sqrt{R}} \tag{2.11}$$

And

$$V_E = \omega_0 M_0 C_{critical} \sqrt{R}\, V_{sample} \tag{2.12}$$

However, when the resonator is overcoupled, as is typically the case in pulsed EPR, only a portion of this signal voltage is transmitted from the resonator into the 50 Ohm waveguide leading to the spectrometer. The output voltage, $V_{E\beta} = \frac{\sqrt{\beta}}{1+\beta}\sqrt{\frac{Z_0}{R}}V_E$

Where Z_0 is the characteristic impedance of the waveguide and coaxial cable, i.e., 50 Ohm, and

$$\beta = \frac{2Q_H}{Q} - 1 \tag{2.13}$$

Is calculated from the critically coupled Q-factor (Q_H) and the overcoupled Q-factor (Q). We combine these equations to calculate, $V_{E\beta}$ to be

$$V_{E\beta} = \sqrt{Z_0}\frac{\sqrt{\beta}}{(1+\beta)}\omega M_0 C_{critical} V_{sample} \tag{2.14}$$

Finally, we can translate this into a more useful form by noting that

$$V_{E\beta} = \sqrt{Z_0}\frac{\beta}{(1+\beta)}\omega_0 C_{critical}\left(\frac{M_0}{N_0}\right)\left(N_0 V_{sample}\right) \tag{2.15}$$

Where we have noted that M_0/N_0 is approximately the same for all room temperature measurements of spin ½ samples at X-band, and $N_0 V_{sample}$ is the number of spins in the active volume of the resonator.[23,24]

f) Receiver Noise Figure Measurements

The Agilent scope at the end of the detector train acquired a series of 100 separate (un-averaged) shots of noise. The average voltage was subtracted from each waveform and then calculated the absolute value of the Fourier transform for each scan to generate a power

spectral density of the noise, which was then signal averaged across the 100 acquisitions. Since the Agilent scope observes noise voltages that have been amplified, to compare the theoretical thermal noise levels, we must convert these values to an input-referred noise level. For this, we must measure the exact gain of the various components.

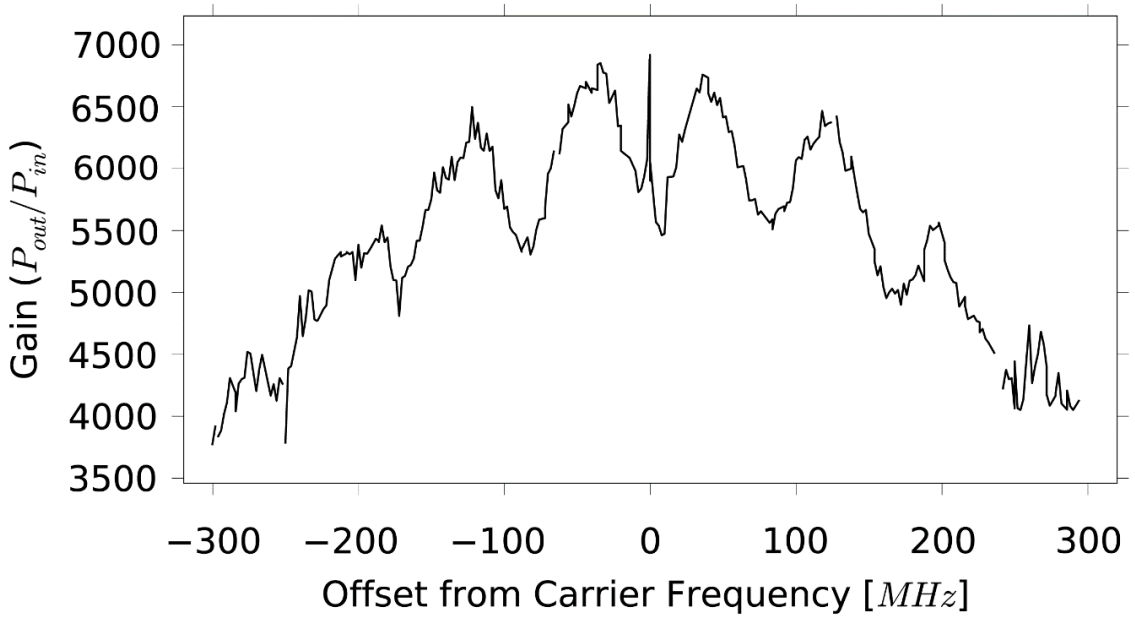

Figure 2.3 Gain for the detector as a function of frequency.

g) Gain and Noise Figure of Heterodyne Detector

To measure the noise figure for the heterodyne detector, we must measure the gain and the noise power density. The gain (P_{out}/P_{in}) of the heterodyne detector was found by inputting a test signal of known power into the detector. The final output power was measured on the Agilent scope ($P_{out} = \frac{V_{rms}^2}{R} = \left(V_{pp}/2\sqrt{2}\right)^2/R$, R = 50 Ohm). The frequency of the test signal was varied using the DAC board (to overcome the 50 kHz low frequency cutoff of the video amplifiers) and its power, P_{in}, was simultaneously measured, via a

splitter, with a Giga-tronics 8541C Universal Power Meter with a 0.01-18 GHz Power Sensor Model 80401A.

The detection system is considered in two parts, block A and block B. We measure the gain of block A, block B, and block A + B (Figure 2.4). To measure the gain of block A, we use the power meter instead of the Agilent oscilloscope because we have not downconverted with the IQ mixer to 0-500 MHz at this point. The gain of block A was found to be 889.2 (29.49 dB), the gain of block B was found to be 6.2 (7.9 dB), and the gain of block A + B was found to be 4000 (36 dB). To verify that the gain measurement was performed in the linear regime of the detector, the DAC output power was varied to confirm the gain was consistent. The gain was flat (+/- 10%) over a 200 MHz range.

The noise figure for the detection system was calculated from taking the ratio of the input referred noise power density (N_{out}/g) and the thermal-Johnson noise power density (N_{in}).

$$NF = 10 \log\left(\frac{N_{out}/g}{N_{in}}\right) \tag{2.16}$$

The noise figure for the entire detection system (block A + block B) was measured to be 10 dB, which is much higher than the expected 2.51 dB based on component specifications.

The relatively high noise figure of the block B portion of the detector, (NF=20 dB, corresponding to T_e = 29700 K) that follows the LNA is higher than expected based on device specifications. The loss of the mixer upon conversion from RF to IF is specified as ~10 dB. The noise figure for the mixer is calculated based solely on the attenuation (NF = 10 dB, T_e=2682). Combined with the specified noise figure and gain of the IF amplifiers (5.3 dB or 711.7 K and 10 $log_{10}(g)$=20 dB), this yields a predicted noise figure of 15.3 dB (Te=9800 K) for block B.

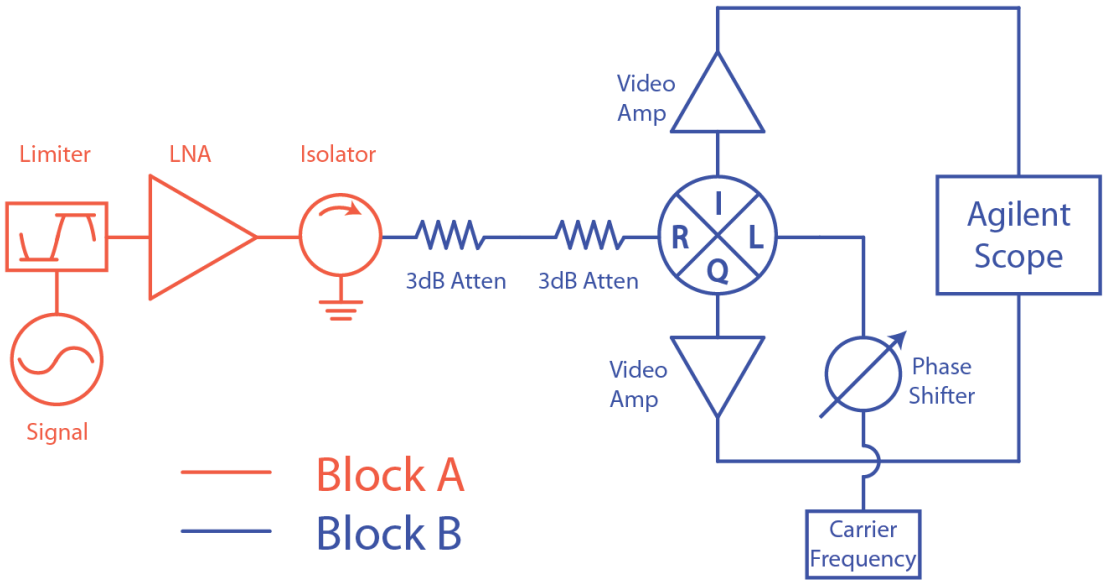

Figure 2.4 Schematic showing block A and block B of the heterodyne detector used for noise characterization.

Table 2.1 Noise figure and noise temperature calculations from device specifications as well as noise figure measurements for block A+B, block A, and block B of heterodyne detector.

Component	Gain [dB]	Accumulated gain [dB]	NF [dB]	Noise Temp [K]	Accumulated Noise Temp. [K]	Accumulated NF [dB]	Measured Accumulated NF [dB]	Bandwidth
Limiter	-1	-1	1	77.160	77.160	1.00	-	GHz
LNA	34	33	1.3	103.991	208.077	2.30	9.7 +/- 0.1	1 GHz
Isolator	-1	32	1	77.160	208.115	2.30	-	GHz
3dB atten	-3	29	3	296.588	208.302	2.30	-	GHz
3dB atten	-3	26	3	296.588	208.676	2.31	-	GHz
IQ	-10	16	10	2682.000	215.413	2.36	-	500 MHz
Video Amp	20	36	5.3	711.756	233.291	2.51	9.80	500 MHz
Block A								
Component	Gain [dB]	Accumulated gain [dB]	NF [dB]	Noise Temp [K]	Accumulated Noise Temp. [K]	Accumulated NF [dB]	Measured Accumulated NF [dB]	Bandwidth
Limiter	-1	-1	1	77.160	77.160	1.00	-	GHz
LNA	34	69	1.3	103.991	208.077	2.30	9.7 +/- 0.1	1 GHz
Isolator	-1	68	1	77.160	208.077	2.30	-	GHz
Block B								
Component	Gain [dB]	Accumulated gain [dB]	NF [dB]	Noise Temp [K]	Accumulated Noise Temp. [K]	Accumulated NF [dB]	Measured Accumulated NF [dB]	Bandwidth
IQ	-10	-10	10	2682.000	2682.000	10.00	-	500 MHz
Video Amp	20	10	5.3	711.756	9799.556	15.30	15.40	500 MHz

h) Expected SNR

For our sample of 4.6 mol/kg BDPA-PS, the number of spins, $N_0 V_{sample}$, was calculated to be 7×10^{18} spins (8.4×10^{-8} m^3 packed solid sample). Yielding a predicted magnetization of 0.587 J/Tm^3 and an RMS signal voltage of 0.269 V. Combined with our expected noise level of 8.68×10^{-4} V (RMS voltage with 500 MHz bandpass filter), this yields a predicted spin-echo SNR of 687.

i) Experimental Signal-to-Noise

The signal-to-noise for our instrument with a single shot is 1-2 from the echo experiment with a BDPA-PS sample does not match our expected SNR, nor standard literature values. The (input referred) experimental signal to noise was found to be 8.29×10^{-6} V. The signal level, even after compensating for relaxation, is lower than the estimated 0.269 V from the macroscopic magnetization by 5 orders of magnitude.

The work by Eaton[23] quotes a signal-to-noise ratio of ~25 for a homebuilt and two commercial X-band spectrometers with resonators operating at a Q of ~400 and containing a 1.00 kGy irradiated fused quartz rod with 3.15×10^{14} spins in the active volume. This sample has 4 orders less magnitude less spins, so we would expect a much higher order of magnitude signal-to-noise than this standard.

A receiver train noise figure of 1-2 dB would be acceptable, however, our noise figure was found to be 10 dB. This is problematic; however, it doesn't nearly account for the extremely low signal voltage we observe. In the setup where these measurements were made, a high-power solid-state amplifier is turned on during acquisition. If a microwave blanking switch was added after the high-power amplifier, we would expect to reduce the noise power by 4 orders of magnitude based on the gain of the solid-state amplifier and pre-

amplifier. An alternative to reduce the noise power density would be to use a gated TWT amplifier which is effectively off while the amplifier is not gated. Because state-of-the-art pulsed EPR measurements require the highest possible amplifiers possible, our strategy to reduce the noise at the receiver is to implement a high-power (1kW) TWT amplifier into the spectrometer.

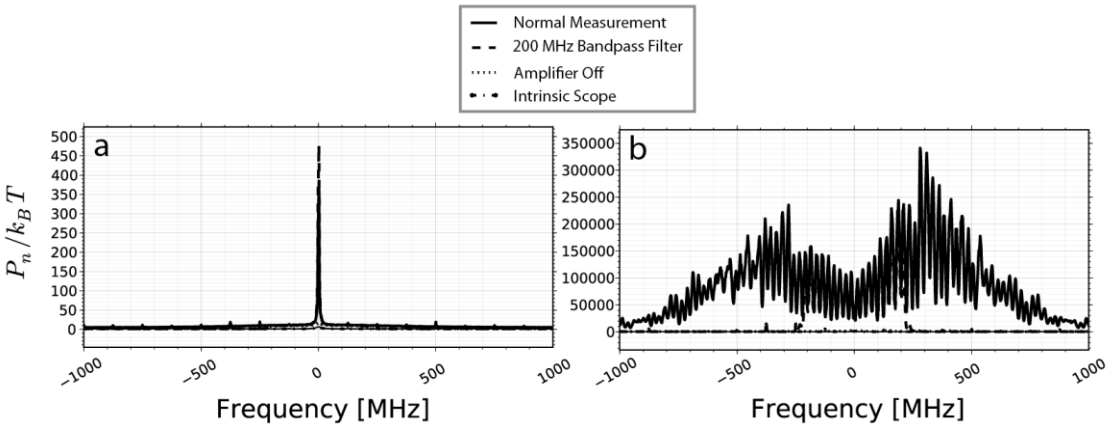

Figure 2.5 Comparison between the noise level from the (a) TWT and (b) solid state amplifier as measured. “Normal Measurement” signifies the noise level for a typical experiment. The “200 MHz Bandpass Filter” is the noise level with a 200 MHz bandpass filter directly connected to the detection oscilloscope. The 200 MHz bandpass filter is used to ensure that there is no aliasing which would increase the noise level of the measurement. “Amplifier Off” is the noise level of the system with the high-power amplifier off, but still all other active microwave components powered (e.g. receiver low noise amplifier and video amplifiers). “Intrinsic Scope” is the noise level when the oscilloscope is terminated with 50 Ohm loads and should be equal to the thermal Johnson noise generated by a 50 Ohm resistor. (a) the spike at zero frequency is caused by measuring the noise directly after the pulse so that the noise level is comparable to an actual pulsed EPR experiment. (b) The noise from the solid-state amplifier. The noise is a combination of noise from the pre-amplifier and solid-state amplifier.

Figure 2.5 shows the noise power density relative to thermal noise for the TWT amplifier and the solid-state amplifier. As suggested earlier, we observe a dramatic reduction in noise power at the receiver with the TWT due to noise only occurring during the pulse gate. During detection, when the TWT is no longer gated, the noise level approaches thermal noise levels. In this instance, we measure the noise power directly after the microwave pulses. This produces a large peak at zero frequency which comes from baseline fluctuations. If the noise power density is measured further away from the pulses, the peak at zero frequency vanishes.

j) Signal-to-noise comparison with commercial spectrometers

Commercial Bruker X-band spectrometers also use a 1 kW TWT amplifier. It is therefore important to compare the performance of our home-built spectrometer to a commercial spectrometer. Figure 2.6 shows a signal to noise ratio comparison for a series of pulsed EPR experiments on a series of spectrometers with the same Bruker coal standard. The absolute echo signal to noise for our home-built AWG spectrometer is approximately 3 times less than the best commercial spectrometer. We must be careful comparing the signal to noise ratios for the 4 different spectrometers because the tuning of the microwave resonators may be slightly different. This is in good agreement with our calculated noise figure for our heterodyne detector which was approximately 10 dB. For our home-built spectrometer, our deadtime can be seen from the Hahn echo experiment to be approximately 40 ns larger than the commercial spectrometers. For our home-built spectrometer, we observe larger fluctuations in the baseline for individual shots, however, this averages out with 100 or more shots.

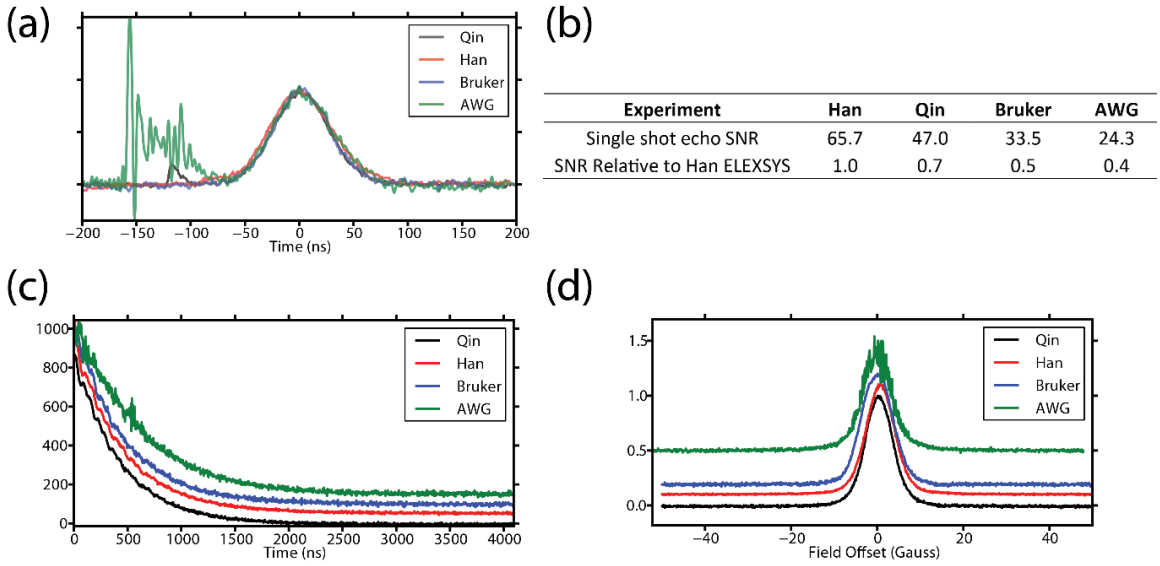

Experiment	Han	Qin	Bruker	AWG
Single shot echo SNR	65.7	47.0	33.5	24.3
SNR Relative to Han ELEXSYS	1.0	0.7	0.5	0.4

Figure 2.6 (a) Single shot Hahn echo experiment using 16 ns and 32 ns pulses and 150 ns delay between pulses. (b) Table with signal to noise ratios for part (a). (c) 10 shot Hahn echo decay experiment. (d) Single shot field swept echo experiment.

k) Suppression of IQ Mixer Leakage

Mixers are for both upconversion and downconversion of a local oscillator (LO) frequency (ω_{LO}) by an amount equal to the intermediate frequency (IF). In the ideal case, the output channel (RF for radio frequency) of a mixer contains no original local oscillator, but in reality the isolation between the LO and RF is not zero resulting what is called LO leakage. Typical values for the LO leakage at X-band frequencies are in the 20 to 30dB isolation. For pulsed EPR applications, this can result in unwanted saturation of the electron spins.

$$\cos(\omega_{LO}t)\cos(\omega_{IF}t) = \frac{1}{2}(\cos([\omega_{LO} + \omega_{IF}]t) + \cos([\omega_{LO} - \omega_{IF}]t)) \qquad (2.17)$$

The high dynamic range of 42 dB allows us to apply a constant offset to the mixer and dramatically decrease the amount of LO leakage.

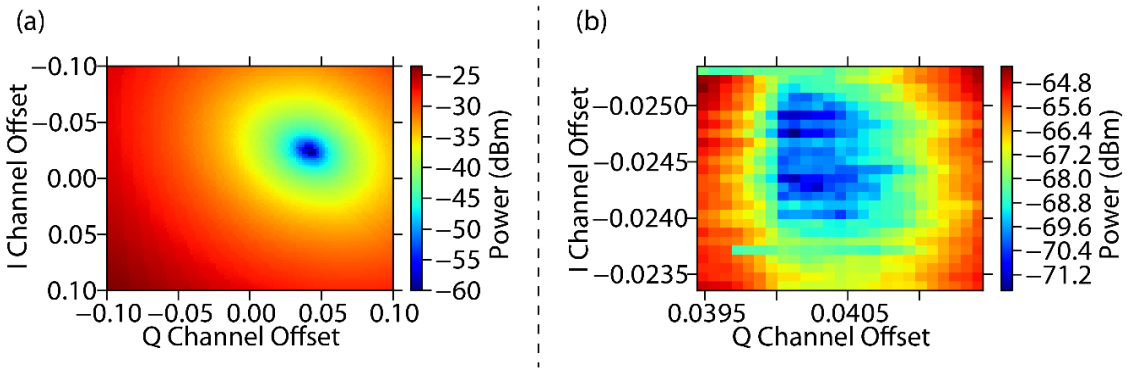

Figure 2.7 One of the specifications of mixers is LO to RF isolation. This is the measure of how much LO (~9.5GHz) signal will leak through, even though no intermediate frequency (IF; DC-500MHz) is applied. Our IQ mixer has a specified LO-RF isolation of minimum 25 dB and maximum 35 dB. We can improve the IQ LO-RF isolation by destructively interfering with mixer leakage. Our current strategy is to correct for this digitally by applying a DC offset to the I and Q channels which minimizes the power output of the RF signal. This could also be corrected for in hardware using a variable phase shifter and variable attenuator to destructively cancel out the leakage at the output of the IF.[25] (a) Power leakage through the IQ mixer acquired with a Gigatronics powermeter via a directional coupler. The power leakage is minimized at I offset of -0.02451 and Q offset of +0.0402688. Notice that the minimum is slightly diagonal; this would be caused by isolation between the I and Q channels or by the quadrature phase deviation between the I and Q channels. (b) Zoomed in on minimum region of (a). The isolation of the IQ mixer has been improved by ~30 dB by applying the calibration. The isolation between pulse and delay is close to 20 dB.

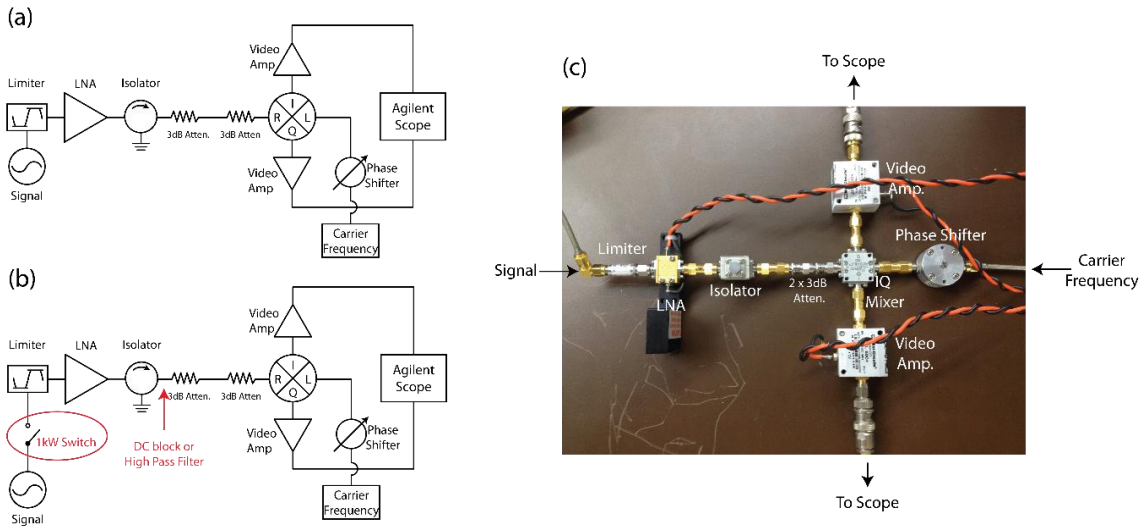

Figure 2.8 (a) Schematic diagram of the receiver. (b) Schematic diagram of the receiver with position of a 1kW peak power tolerance microwave switch. The switch would reflect the 1kW pulses from the TWT amplifier, but allow the signal to pass through. The limiter would still be included to add a second layer of protection at least until we have verified the switch is working properly. The suggested position of a DC block is also included. The DC block is essentially a high frequency pass filter that ideally prevents DC offsets reaching the IQ mixer and video amplifiers where they would show up on the detection oscilloscope as a large baseline. (c) Picture of the receiver with all components labelled.

l) Characterization of the Microwave Resonator Transfer Function

In liquid state NMR, the bandwidth of the resonator is usually not a concern, because chemical shifts are typically parts per million of the resonance frequency, however in EPR, we deal with much larger spectral bandwidths. For instance, at X-band the hyperfine anisotropy is 1% of the resonance frequency. Therefore, it is typical in pulsed EPR to overcouple the resonator to increase the resonator bandwidth by overcoupling the resonator as much as possible.

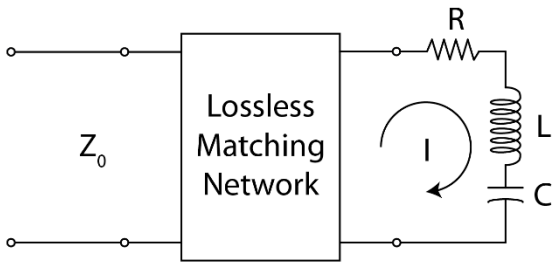

Figure 2.9 Lumped circuit equivalent of resonator. $\boldsymbol{Z_0}$ (usually 50 Ohm) is the characteristic impedance of the transmission line coupled to the resonator.

The effect of the resonator on the pulse can qualitatively be understood by modeling it as a series RLC circuit. A rectangular microwave pulse of length, t_p, starting at $t = 0$ with a carrier frequency of ω_{mw} has a complex driving voltage, $v(t)$, of

$$v(t) = \begin{cases} \exp[i(\omega_{mw}t + \theta)] & \text{if } t \geq 0 \text{ and } t \leq t_p \\ 0 & \text{if } t < 0 \text{ or } t > t_p \end{cases} \tag{2.18}$$

The time response of the RLC circuit, as given by Kirchhoff's current and voltage laws, is

$$LC\frac{d^2I(t)}{dt^2} + RC\frac{dI(t)}{dt} + I(t) = C\frac{dv(t)}{dt} \tag{2.19}$$

Using standard notation we define

$$\omega_0^2 = \frac{1}{LC} \tag{2.20}$$

$$\Delta\omega = \frac{1}{RC} = \omega_0/Q \tag{2.21}$$

$$\omega_r^2 = \omega_0^2 - \left(\frac{1}{2}\Delta\omega\right)^2 \tag{2.22}$$

$$\delta = \omega_r - \omega_{mw} \tag{2.23}$$

$$\epsilon = \delta/\Delta\omega \tag{2.24}$$

The solution, $I(t) = I_h(t) + I_s(t)$, of equation is the sum of the homogenous and steady state parts, where $I_h(t)$ is the homogeneous solution and $I_s(t)$ is the steady state solution. The steady state solution is an oscillation at the pulse frequency

$$I_s = I_0 \exp[i(\omega_{mw} t + \theta - \phi)] \tag{2.25}$$

With

$$I_0 = V_0 \cos(\phi) / R \tag{2.26}$$

$$\tan \phi = Q(\omega_{mw}^2 - \omega_0^2)/(\omega_{mw}\omega_0) \tag{2.27}$$

And the homogenous solution is analogous to the solution for a damped harmonic oscillator

$$\begin{aligned} I_h = I_0 \exp\left(-\frac{1}{2}\Delta\omega t\right)\Bigg[-\frac{1}{2}\left(\frac{\omega_r + \omega_{mw}}{\omega_r} - i\frac{\Delta\omega}{2\omega_r}\right) \\ \times \exp[i(\omega_r t - \theta - \phi)] + \frac{1}{2}\left(\frac{\omega_r + \omega_{mw}}{\omega_r} - i\frac{\Delta\omega}{2\omega_r}\right) \\ \times \exp[-i(\omega_r t + \theta - \phi)] - \exp[-i(\omega_r t - \theta + \phi)]\Bigg] \end{aligned} \tag{2.28}$$

The homogenous solution consists of three parts: (1) An exponential decay with a time constant of $t_r = 2/\Delta\omega = 2Q/\omega_0$, (2) an oscillation at the resonator free-ringing frequency, ω_r, and (3) an oscillation at minus the free-ringing frequency.

If the resonator is critically coupled, oscillations from (2) and (3) are critically damped and the result is a cavity ringdown which can be approximated as an exponential decay. In most pulsed EPR applications, we overcouple the resonator to a Q-factor of ~100, or as much as required to reduce the experimental dead-time, however the cavity Q-factor is high enough to approximate the ringdown as an exponential decay. Thus, the resonator has a ring-up and ring-down period that is exponential in character. This assumption is equivalent to assuming the resonator dip is a complex Lorentzian function in frequency domain.

m) Example of Resonator Transfer Function

We may summarize the results above as follows: the resonator convolves the pulse in time-domain with a function that depends on the resonator Q-factor. The simplest model for this function is a mono-exponential decay given by $h(t) = e^{-\frac{1}{2}t/\tau} = e^{-\frac{1}{2}t(\omega_0/Q)} = e^{-\frac{1}{2}t\Delta\omega}$, where $h(t)$ is the transfer function of the resonator, τ is the cavity ringdown time-constant, and $\Delta\omega$ is the bandwidth of the resonator response. An example of a pulse convolved with this model is given in Figure 2.10. In reality, the simple model given above is often not sufficient and the transfer function is experimentally determined.

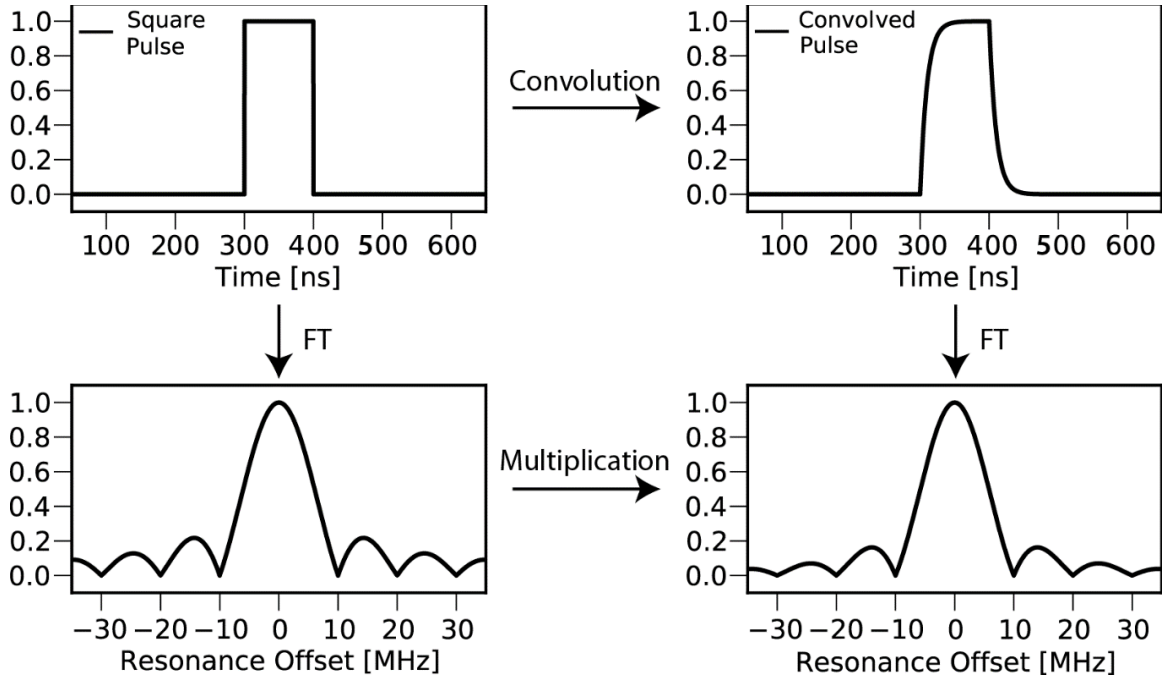

Figure 2.10 Example transfer function distorting the shape of the pulse.

n) Formal Definition of Transfer Function

To calculate the transfer function, we will use the experimental excitation profile and the excitation profile of the pulse determined by Fourier-transform of the pulse. The transfer function to be determined is defined by a convolution integral in time-domain:

$$y(t) = h(t) * x(t) = \int_{-\infty}^{\infty} h(t-\tau)x(\tau)d\tau \tag{2.29}$$

Where $y(t)$ is the convolved pulse, $h(t)$ is the transfer function, and $x(t)$ is the original pulse shape. Our calculations are more convenient in frequency domain because the convolution theorem allows us to write a convolution in the time-domain as multiplication of the Fourier-transformed functions:

$$F\{y(t)\} = F\{h(t)\}F\{x(t)\} \tag{2.30}$$

Or

$$Y(\omega) = H(\omega)X(\omega) \tag{2.31}$$

Where capitalized variables, $Y(\omega)$, $H(\omega)$, and $X(\omega)$ now represent the Fourier transforms of $y(t)$, $h(t)$, and $x(t)$, respectively.

Thus, we have a simple expression for the transfer function in frequency space given by:

$$H(\omega) = Y(\omega)/X(\omega) \tag{2.32}$$

$X(\omega)$ is known based on the original pulse waveform and $Y(\omega)$ can be determined experimentally.

If a pulse is defined as

$$X'(\omega) = X(\omega)/H(\omega) \tag{2.33}$$

We have cancelled out the effects of the transfer function from the original waveform and the pulse inside the resonator will have the frequency profile of the desired pulse.

o) Experimental Determination of Transfer Function

The transfer function of the resonator can be found in three ways: (1) by monitoring the magnetic field inside the cavity with a pickup coil,[17] (2) by varying the resonance offset (e.g. sweeping the magnetic field) to map out the response to a pulse in the linear tip angle regime,[12] and (3) measure the transient nutation as a function of frequency while sweeping the field to maintain "on-resonance" condition to map out the ν_1 nutation frequency.[13]

p) Calibration of Pulse Shapes – Solid state amplifier (10 W)

To obtain excitation profiles, we acquire FIDs over a desired field range (resonance offset). We take the time axis to be the direct dimension and the field axis to be the indirect dimension. The field axis can be converted to units of MHz by assuming a g-factor of 2.00 which gives 2.8 MHz = 1 G. If we Fourier transform the FIDs, we obtain a two-dimensional array with frequency offset (direct dimension) and resonance offset (indirect dimension converted from field) as axis. The signal is down the main diagonal of the data. Next, if we desire phase information, we can perform a linear and zeroth order phase optimization, otherwise we can take the absolute value. We apply a bandpass filter along the main diagonal to remove excess noise and sum along the frequency offset dimension. The result is the excitation profile for the pulse.

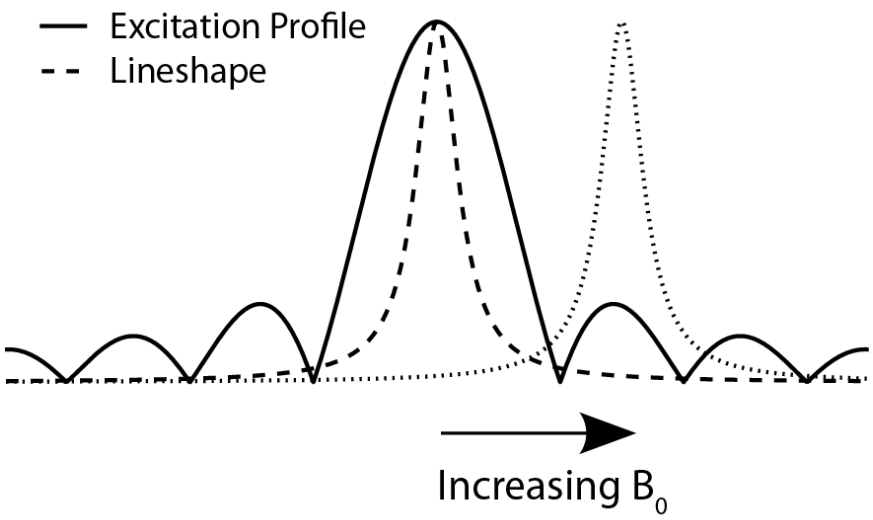

Figure 2.11 Example of field sweep to obtain excitation profile.

q) Correcting for the Resonator Transfer Function

Using the excitation profiles of very short pulses (e.g. 50 ns sinc and 10 ns square), it allows us to more accurately determine the transfer function of the resonator over a wide range of frequencies.

The excitation profile from the short pulses is highly structured due to reflections of microwaves at the intersection of various microwave components. The similarities between the excitation profiles of the sinc and square pulses indicate that the structure is physical and, as expected, the transfer function is independent of pulse shape.

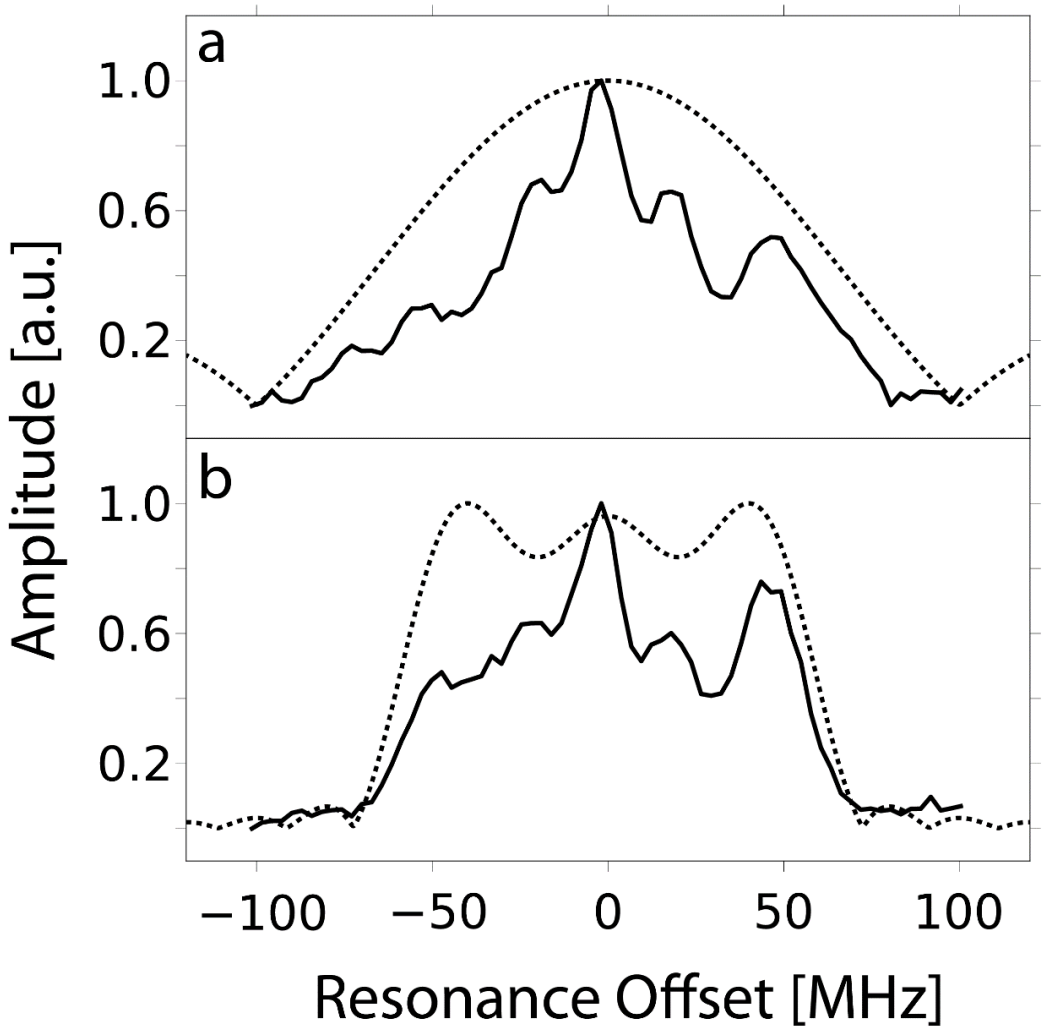

Figure 2.12 Excitation profiles for (a) 10 ns square and (b) 50 ns sinc pulses. Solid lines are the experimental excitation profiles, dashed lines are Fourier transform of pulses.[12]

Once we have determined the transfer function accurately with a short, broad bandwidth pulse, we can apply this transfer function to different pulses and observe the intended excitation profile. Improvement in the excitation profile was observed for 100 ns square, 250 ns Gaussian, and 250 ns truncated sinc pulses.

More technical details will be laid out in this section which are necessary to consider for the transfer function correction. Once we obtain the frequency domain corrected pulse, we

must inverse Fourier transform this to get ta time-domain pulse. The inverse Fourier transformed pulse is not always the same length as the original pulse, often it is longer than the original pulse. Truncating the pulse has several effects: (1) broaden the excitation profile (2) remove noise from the excitation profile (smoothing the excitation profile) and (3) create sinc ringing in the excitation profile. Despite this, it can be verified that the integrity of the pulse wasn't changed appreciably by truncation the pulse.

Sometimes it was necessary to perform multiple iterations to obtain the desired improvement in the excitation profile. Successive transfer functions we calculated based on the difference between the previous pulse and the Fourier transform of the desired excitation profile. The need to perform multiple iterations shouldn't be necessary, but is due to experimental noise and uncertainty in the transfer function.

Improvement of the excitation profiles after the transfer function correction is clearly shown in figure 2.13. By correcting for the resonator we show that we can not only generate arbitrarily shaped pulses, but we can use the arbitrary pulses to gain substantially more control over the spin system. All pulsed experiments would certainly benefit from having greater control over the spin system.

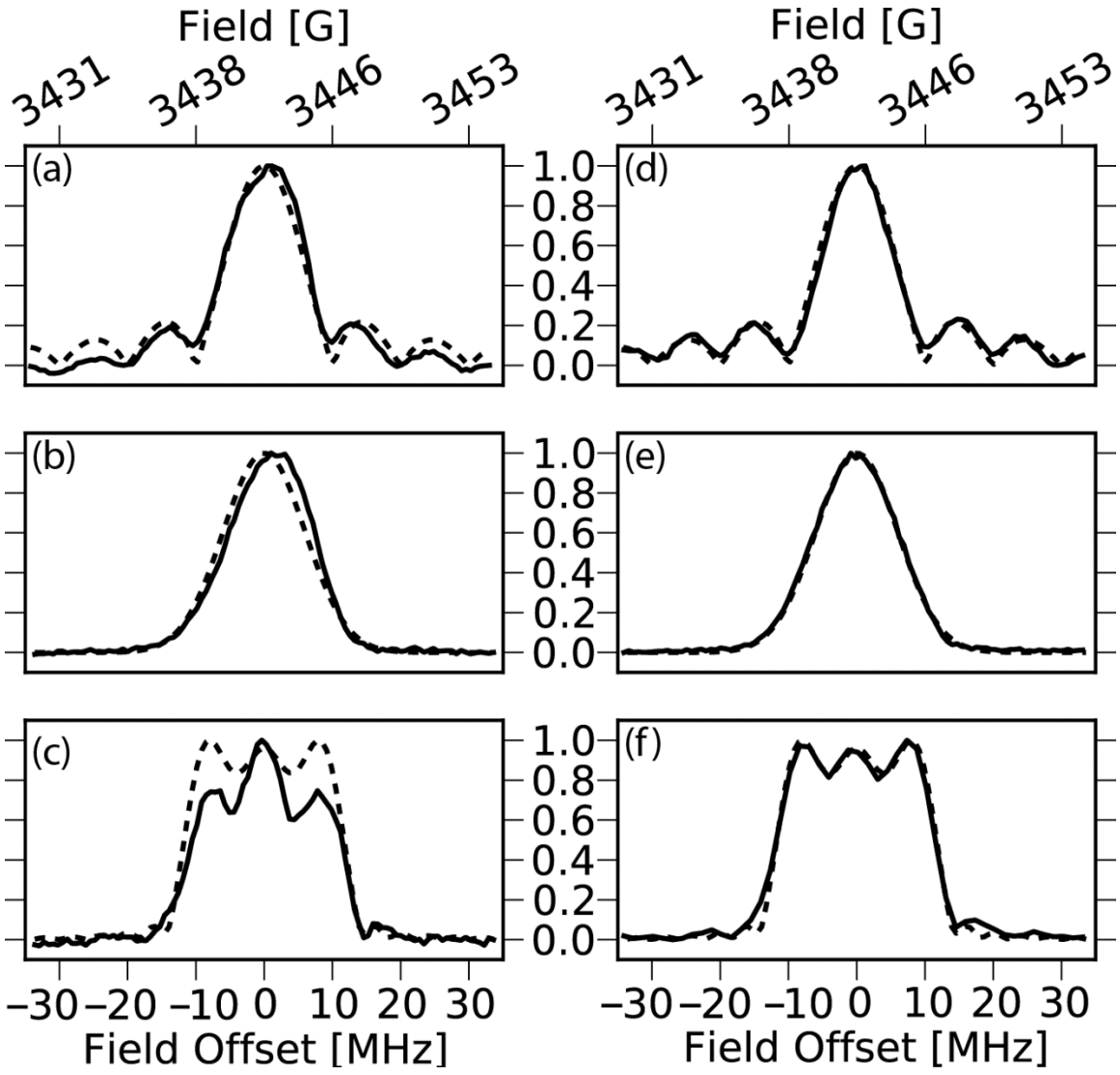

Figure 2.13 (a)-(c) show the Fourier transforms and observed spin response from 100 ns square, 250 ns Gaussian, and 250 ns truncated sinc pulses. (d)-(e) show the same pulses with the transfer function correction.[12]

r) First and zeroth order phase optimization

To obtain valuable phase information from our excitation profiles, we must first phase optimize the data. Phase optimization is the process of demixing the real and imaginary components in the complex Fourier transformed data. If we are dealing with a two-dimensional data set, we have 3 potential phase offsets: (1) a zeroth order phase offset, ϕ_0,

(2) a first order phase offset down the direction dimension, $\phi_{1,direct}$, and (3) a first order phase offset down the indirect dimension, $\phi_{1,indirect}$. These phase offsets can be combined into a single phase offset at each point in the 2-d array.

Thus a phase shift for the ϕ_{ij} is the optimal phase for the ith row and the jth column of a $n \times m$ dimensional array.

$$\phi_{ij} = \phi_0 + \frac{i}{n}\phi_{1,direct} + \frac{j}{m}\phi_{1,indirect} \tag{2.34}$$

Where ϕ_{ij} is the optimal phase for the ith row and the jth column of an n×m dimensional array. Here we have expressed the linear – first order – phases in terms of the total phase variation over each dimension.

s) Physical origin of phase offsets

The deadtime of our instruments prevents us from capturing the entire FID. This causes a phase roll in the Fourier transformed data. This phase roll can be corrected for by using the shift algorithm

$$F\{h(t-\tau)\} = e^{i\omega\tau}H(\omega) \tag{2.35}$$

Where we can see that the effect of a time-domain shift is a phase roll in the frequency domain. This induced a linear shift in the direct dimension.

Another potential linear phase shift comes from the resonance offset (indirect dimension). As we sweep the field, we change the Larmor precession frequency of the spins while keeping the frequency of the source fixed. This is equivalent to changing the resonance offset $\Omega_S = \omega_S - \omega_{mw}$. We must therefore deal with any effects that off-resonance pulses have on the spin system. The effect of an off-resonance pulse is more complicated and causes the spins to acquire a phase as they are rotated into the transverse

plane. The phase is proportional to – or linear in – resonance offset and results in a linear phase roll along the resonance offset dimension.

Additionally, the data may not have the correct zeroth order phase. This results from the real and imaginary channels of the IQ mixer not corresponding to the real and imaginary signal. This is corrected for by multiplying the entire data array by a complex number in the form $e^{i\theta}$.

From this point on, we will assume that we have an $n \times m$ data array, with n the number of points in the direct dimension (Fourier transformed FID) and m the indirect dimension. A linear phase correction will be performed down the indirect dimension. Furthermore, we will decide a set of test zeroth order and linear phase optimizations, $\{\phi_0\}$ and $\{\phi_1\}$, respectively, to apply to the data. As of now, we manually decide a reasonable range of phase optimizations.

Using these sets, we construct a 4-d phase optimization array. Φ_{01} with elements ϕ_{nmjk} defined by:

$$\phi_{nmjk} = \{\phi_0\}[k] + \frac{m}{len(\{\phi_1\})}\{\phi_1\}[j] \tag{2.36}$$

Where square brackets ([ ]) indicate index and len( ) represents the length of a set or array. A summary of the arrays used in the algorithm are shown in Table 2.2.

Table 2.2 Definition of variables for first order and zeroth order phase optimization algorithm.

Variable	Description	Dimensions			
		Frequency	Field	Φ_1	Φ_2
D	Data Matrix	n	m	-	-
C	Corrected Data	n	m	j	k
Φ_{01}	Zeroth and First Order Phase Correction	-	m	j	k
S	Cost Function	-	-	j	k

The algorithm minimizes the absolute value of the real part. We will present $\circ$ as element-wise (Hadamard) matrix multiplication. In pythonian form, where the arrays are automatically tiled down the direct dimension, the algorithm can be summarized as

1.) $C = D \circ \Phi_{01}$ # Calculate corrected data matrix

2.) $S = \text{abs}\big(\text{real}(C)\big).\text{sum}(\text{axis} = 0).\text{sum}(\text{axis} = 0)$ # Find minimum down first order optimization dimension

3.) $\text{where}(S == S.\min(\quad))[0][0]$ # Find minimum down first order optimization dimension

4.) $\text{where}(S == S.\min(\quad))[1][0]$ # Find minimum down zeroth order optimization dimension

The real part of the signal is minimized when the linear phase is optimized, provided that absolute value is taken making negative peaks positive. This algorithm provides a global minimum for the optimal phase, unlike alternative algorithms which would optimize the ratio of the power of the real to the power of the imaginary.

Without phase correction, we can only obtain absolute value spectra which are broader and include a baseline offset. Once the data for a square pulse is properly phased, we can clearly see the sinc lobes which oscillate between positive and negative.

The phase optimization allows us to obtain phase information from our excitation profiles thus also obtain a complex transfer function. A complex transfer function is expected because a Lorentzian cavity dip contains both real and imaginary parts. This is especially important as we approach the edges of the resonator dip and the imaginary part dominates the transfer function.

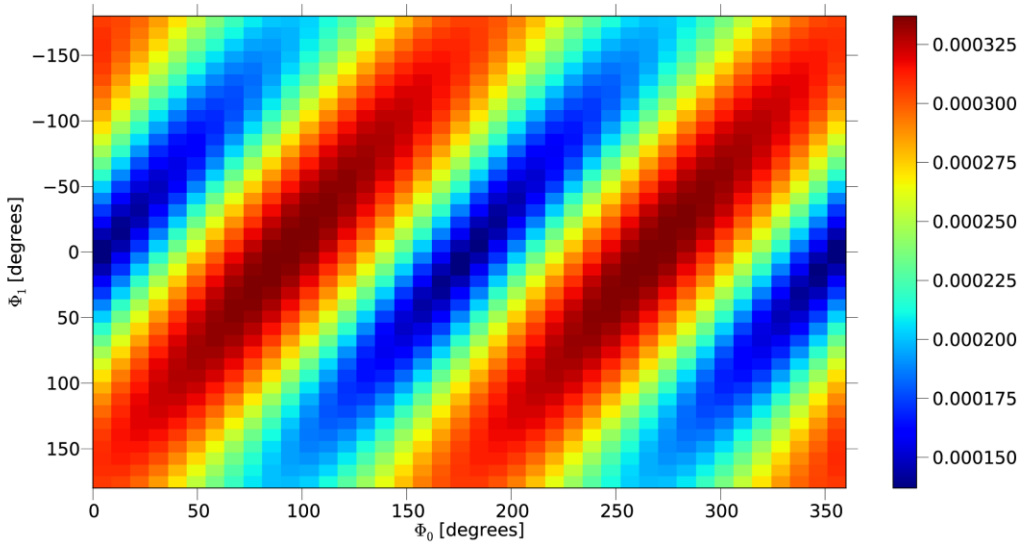

Figure 2.14 Image plot showing the cost function which minimizes the absolute value of the real part. The two minima correspond to zeroth order phase optimizations which are 180 degrees out of phase.

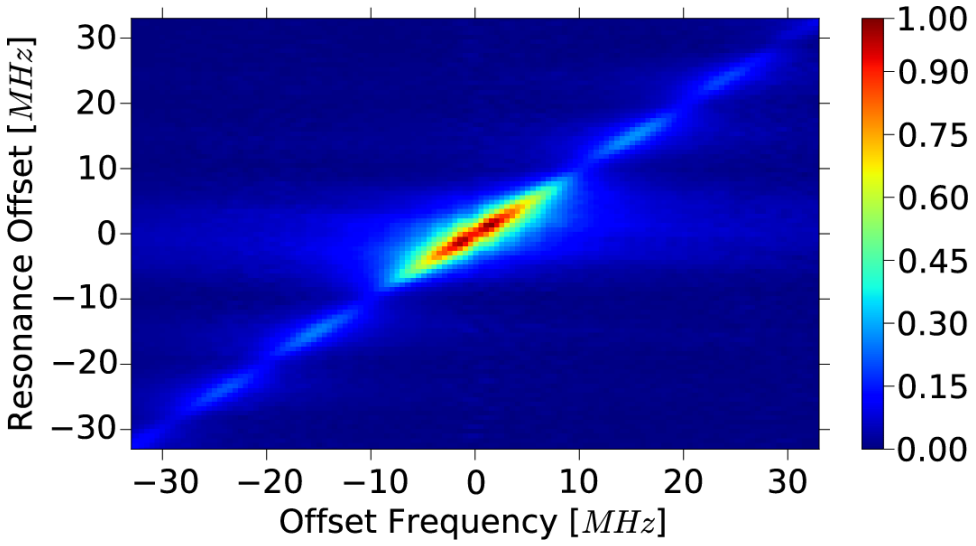

Figure 2.15 Resonance offset (field) and frequency offset (FT of direct dimension) for a 100 ns square pulse after transfer function correction has been applied. Data was zero-filled to increase resolution in frequency domain.

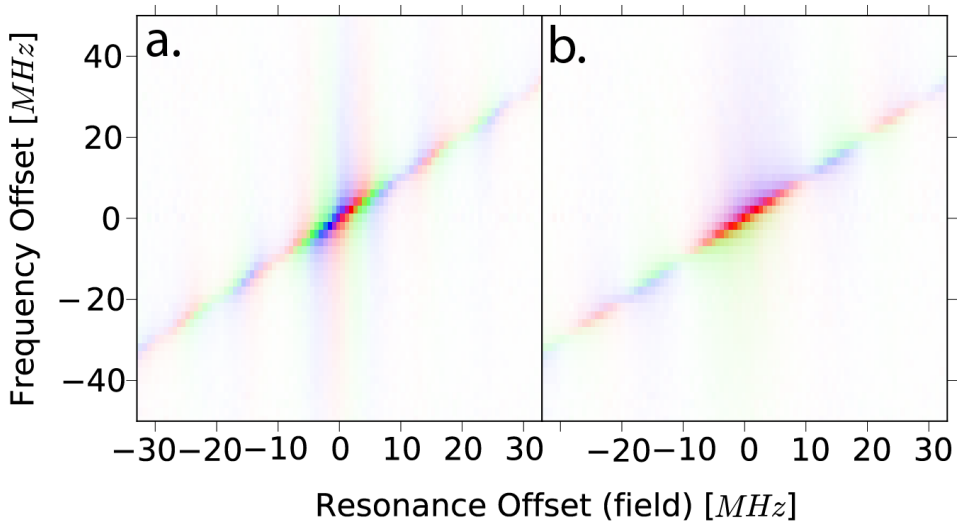

Figure 2.16 Image plot of the data before (a) and after (b) phase optimization. The intensity of the color represents magnitude and color represents phase.

t) Experiments with High Power Amplifier (1 kW TWT)

Upgrading out homebuilt spectrometer with a 1 kW TWT allows for much greater capabilities and for our spectrometer to become advantageous over commercial spectrometers which lack an AWG. To incorporate the TWT into our spectrometer, we must fully characterize the time required for the pulse amplitudes and phases to become stable (Figure 2.17).

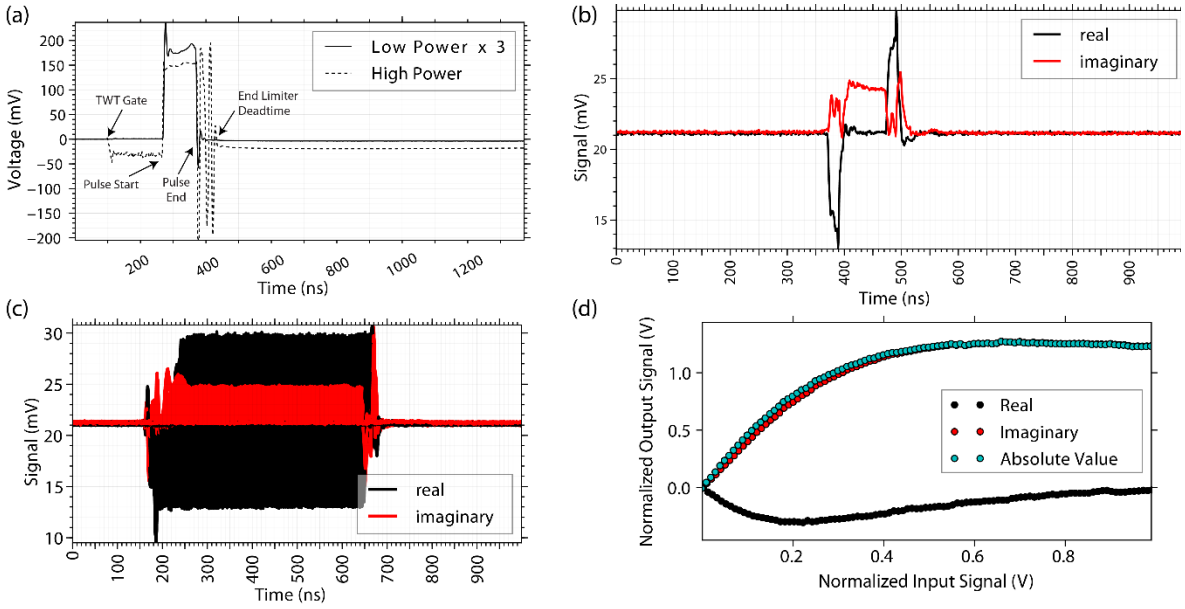

Figure 2.17 (a) Oscilloscope trace of pulse from TWT amplifier. (b) 100 ns pulse waveform amplified by TWT. The phase variations at the beginning and end of the pulse are caused by reflections. (c) 10 ns pulse swept over 500 ns TWT amplifier gate to calculate the time required for amplitude and phase stability. (d) Amplitude transfer function of the TWT amplifier.

In a similar fashion to experiments with the solid-state amplifier, we calibrate pulses and measure the excitation profiles using the linear tip angle method. With the much larger power output of the TWT, it must be verified that calibration can still be obtained with much shorter pulses and much broader bandwidths. The data in Figure 2.18 shows a dramatic

increase in pulse shape fidelity once the pulse has been calibrated for the transfer function of the resonator. It is promising that the excitation profile of the sinc pulse exceeds the bandwidth of a frozen nitroxide radical (~180 MHz).

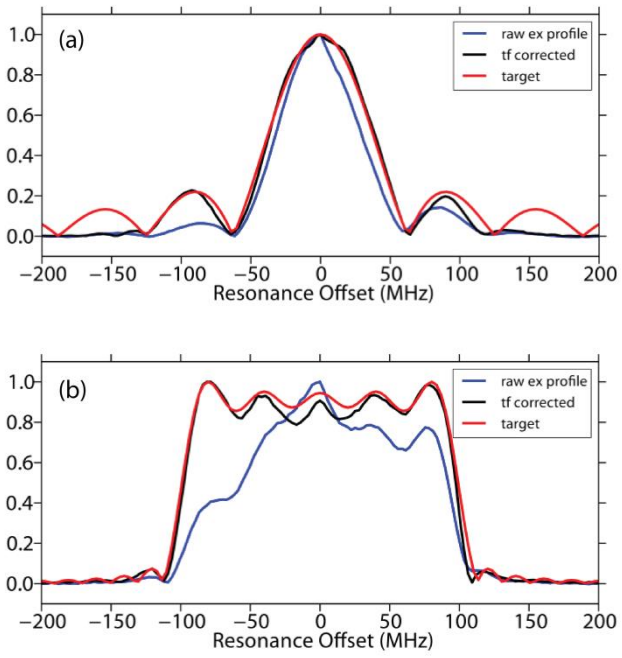

Figure 2.18 (a) Excitation profile of 16 ns square pulse. The experimental data is shown in blue and the FT of a 16 ns square pulse is shown in black. (b) Excitation profile of a 50 ns sinc pulse. As before, the data is in blue and the FT of the pulse is in black.

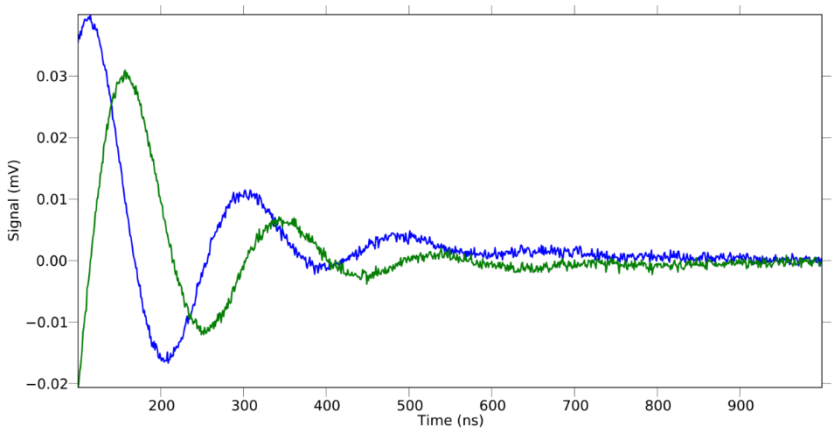

Figure 2.19 Off-resonance FID with BDPA standard. The signal to noise with the TWT amplifier is orders of magnitude better than the solid-state amplifier due to the TWT being off during detection.

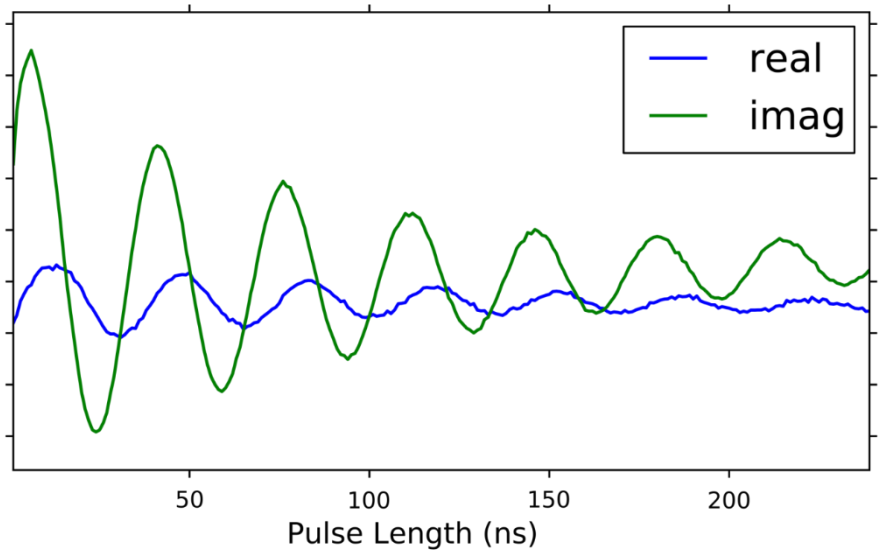

Figure 2.20 Nutation curve from BDPA standard. The 90°-time is approximately 12 ns (MD5 resonator is completely overcoupled).

The Bruker coal standard gives a strong echo signal (T_m in the µs range, T_1 in the ms range) and is useful for testing the different pulsed experiments. A comparison was performed between the AWG EPR spectrometer (MD-5 resonator) and the commercial Bruker ELEXSYS E580 spectrometer (MS-3 resonator). Differences between the data are most likely caused by 1.) experimental parameters not being identical; 2.) IQ mixer leakage, which has not been perfected; 3.) MD-5 resonator versus MS-3 resonator. The microwave power was adjusted to give a 90-time of 16-ns.

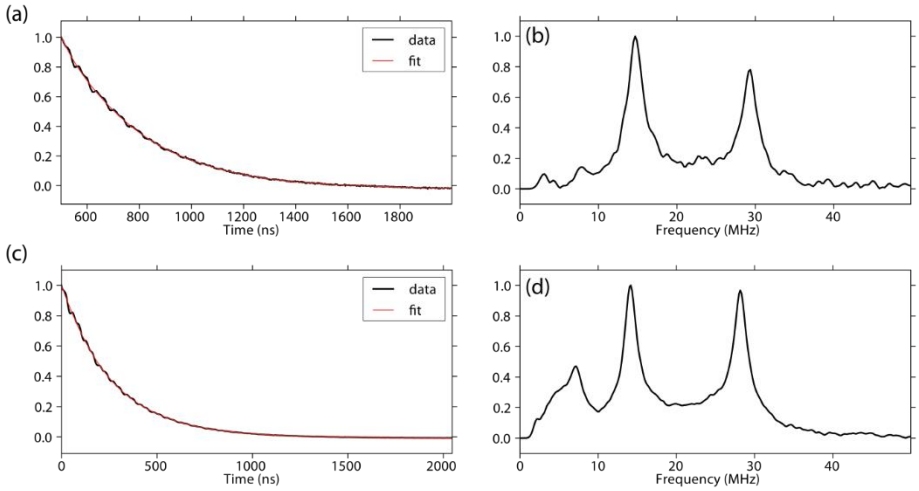

Figure 2.21 (a-b) Home-built AWG system 2-pulse ESEEM data. (c-d) ELEXSYS E580 2-pulse ESEEM data. For both instruments, it can clearly be seen that there are two proton peaks at 14 and 28 MHz. The carbon-13 peak at a few MHz is less pronounced on the home-built system.

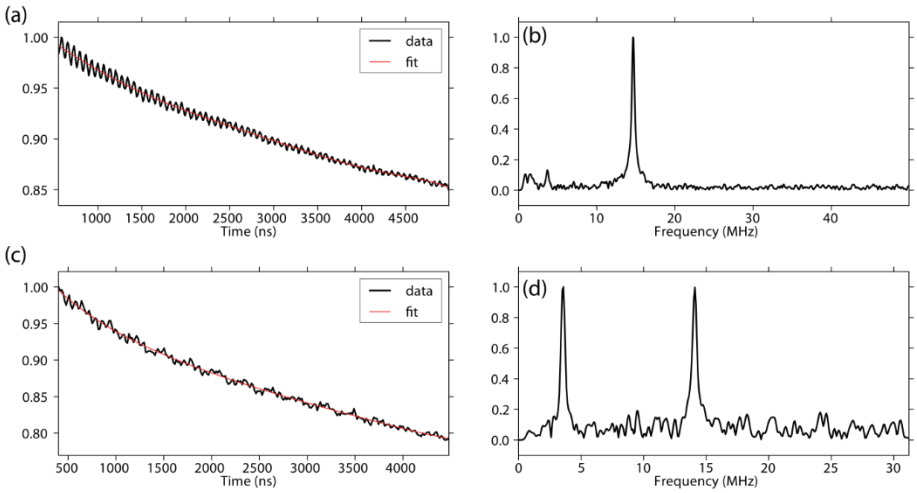

Figure 2.22 (a-b) Home-built AWG system 3-pulse ESEEM data. (c-d) ELEXSYS E580 3-pulse ESEEM data. As before, the carbon peak is suppressed on the home-built system. I suspect that this is caused by IQ mixer leakage, where the leakage has a similar effect to applying a matched pulse.

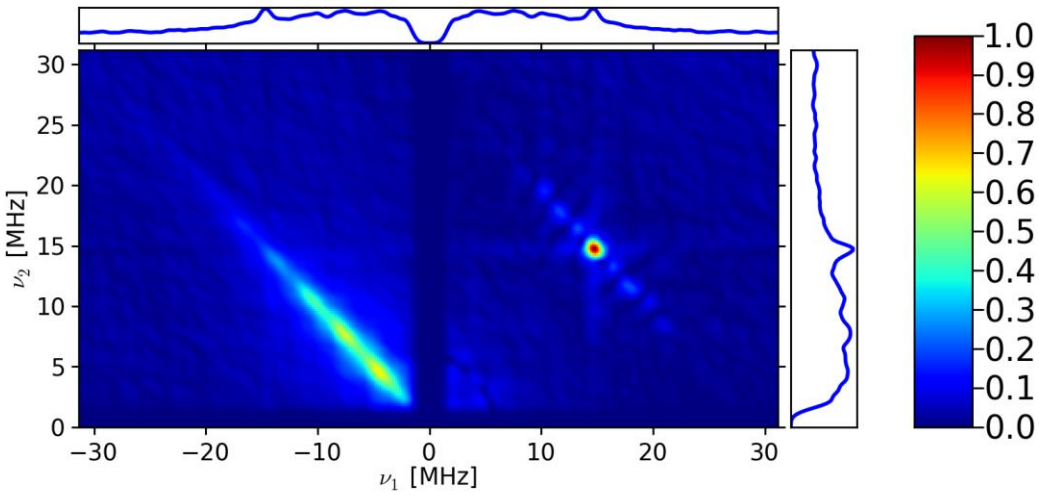

Figure 2.23 HYSCORE data from home-built AWG system. It is promising that the peaks occur in the correct positions, however, the banding in the frequency domain is a problem. I'm not sure exactly about the origin of this, however, it is possible that this is also the IQ mixer leakage.

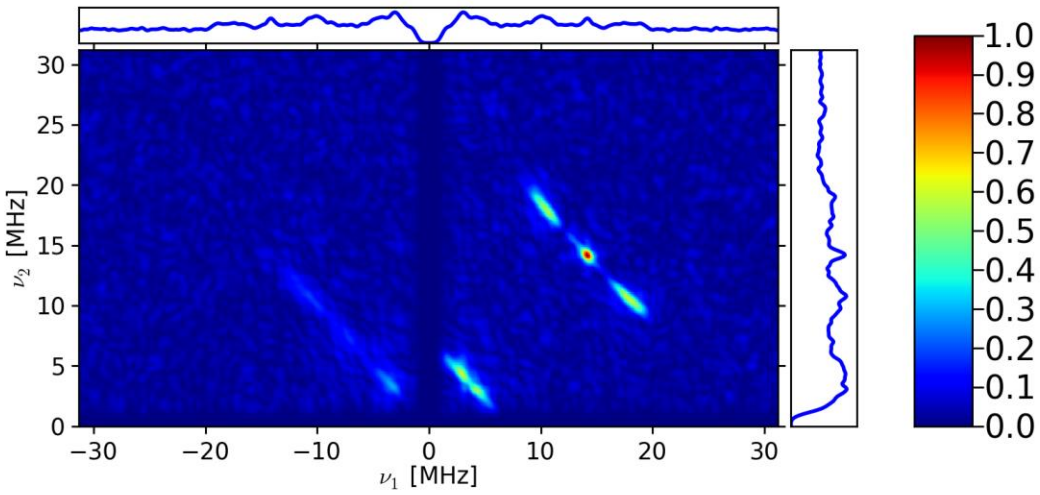

Figure 2.24 HYSCORE data from ELEXSYS. For the ELEXSYS, the 13C signal is visible in the HYSCORE spectrum.

u) Development of Software for Home-Built Spectrometer

To interface the computer with the spectrometer, a set of python libraries was written in-house. The python code controls all aspects of the spectrometer including the microwave frequency, magnetic field, programming the DAC board, and acquiring data from the oscilloscope. For individual experiments (e.g. Hahn echo decay), a python script was written to acquire the data. For long duration experiments, the script can be written to automatically save the data throughout the experiment. To make editing experimental parameters easier, a custom GUI was developed (Figure 2.26). The GUI contains a list of all parameters in a given experiment which is automatically imported once the experiment is run.

```
# Hahn Echo Pulse Program
for scan in np.arange(scans):
    agilentPosition = dx + 2*d1 + 1.5*p0 + p1 + d0
    a.position(agilentPosition)
    for ph0Ix,ph0Value in enumerate(ph0):
        for ph1Ix, ph1Value in enumerate(ph1):
            # Pulse Sequence #
            wave = p.make_highres_waveform([('delay',dx),
            ('function',lambda x: a0*np.exp(1j*ph0Value)*np.exp(1j*2*np.pi*modFreq*x),r_[0,p0]),
            ('delay',d1),
            ('function',lambda x: a1*np.exp(1j*ph1Value)*np.exp(1j*2*np.pi*modFreq*x),np.r_[0,p1]),
            ('delay',9.5e-6 - dx - d1 - p0 - p1)],
            resolution=1e-9)

            # Send pulse to DAC board
            p.synthesize(wave,autoSynthSwitch = True,autoReceiverSwitch = True,
                autoTWTSwitch = True, longDelay = 3e-4)

            # Pull data from scope
            dataTemp = a.Waveform_auto()

            # Process data: Shift to on-resonance and apply bandpass filter
            dataTemp.ft('t')
            dataTemp['t',lambda x: abs(x-modFreq) > bandpassFilter/2.] = 0
            dataTemp.ift('t')
            dataTemp.data *= np.exp(-1j*2*np.pi*modFreq*dataTemp.getaxis('t').copy())

            # Compute Receiver phase and apply
            receiverPhase = rph0[ph0Ix]+rph1[ph1Ix]
            dataTemp.data *= np.exp(1j*receiverPhase)

            # Add to data array
            data += dataTemp
```

Figure 2.25 Example of pulse program used for performing a Hahn echo.

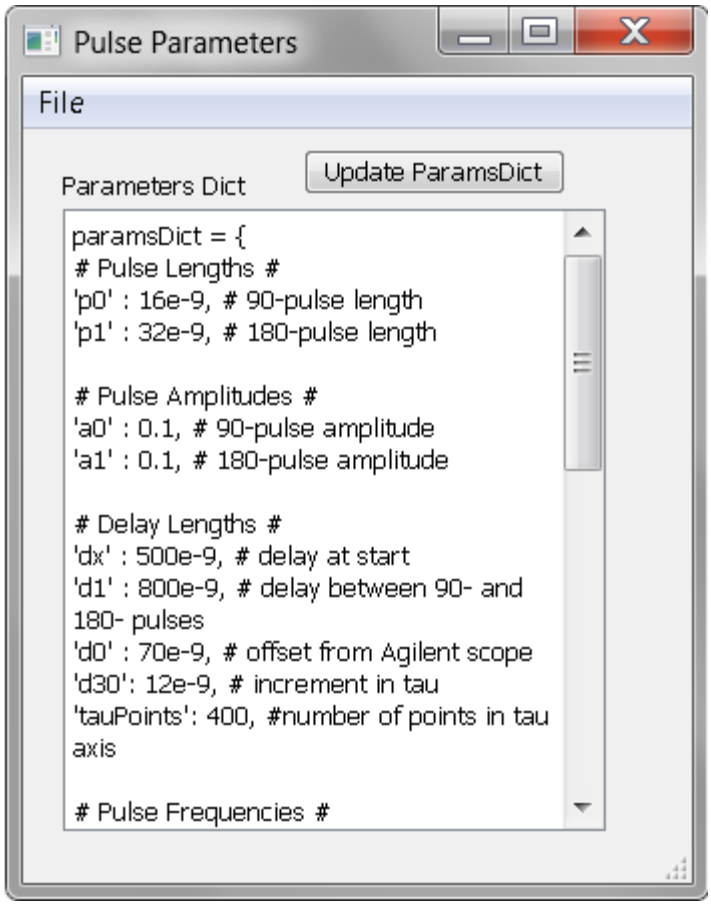

Figure 2.26 Graphical User Interface for updating pulse parameters.

3) Effect of Bandwidth compensation on pulsed EPR experiments with shaped pulses

a) Introduction

For systems lacking long range order, pulse dipolar spectroscopy (PDS) is one of the few methods for measurement of distances in the nm length range[26]. This is particularly important for biochemical applications where PDS distance measurements offer structural information on biopolymers including proteins[9] and DNA/RNA[3]. A variety of PDS techniques exist including double electron-electron resonance (DEER)[27], single-frequency technique for refocusing dipolar couplings (SIFTER)[28], and double quantum coherence (DQC)[29]. The most widely used technique is DEER, but for these measurements we are often limited in SNR and each experiment can require many hours for adequate SNR[30]. In most cases, PDS techniques suffer from limited excitation bandwidth due to the broad linewidth of the electron spins. Such experiments would benefit greatly from the increased bandwidth of pulses analogous to the broadband pulses developed in NMR years ago.[14,15]

Recent developments in arbitrary waveform generators (AWGs) have led to the widespread incorporation of AWGs into pulsed EPR spectrometers[12,13,17,31,32]. These spectrometers are now commercially available and have AWGs exceeding 1 GHz. The simultaneous development of broadband resonators will enable the full utilization of the AWG technology. The development of broadband microwave resonators will become increasingly important for pulsed EPR applications as AWG capabilities allow for broad excitation bandwidths, while still maintaining high conversion efficiency.[33] This will become particularly important as AWG capabilities are extended to the higher frequencies

of Q-band (34 GHz) and W-band (94 GHz) where linewidths are broader due g-anisotropy. For X-band and Q-band applications, the resonator bandwidth is often limited to a few hundred MHz depending on the resonator. While we have the capability of exciting the spectrum beyond the bandwidth of the resonator, we become increasingly limited in microwave power outside this range. It is therefore incumbent to characterize the resonator bandwidth to have an indication for what a reasonable excitation profile is expected for a given pulse. From the characterization of the resonator bandwidth, it is then possible to calibrate the pulse shapes to more uniformly excite the spins across the entire range of the spectrum.

In this work, we aim to characterize the bandwidth of the resonator and determine the improvement in fidelity of pulse excitation as well as impact on the signal to noise ratio (SNR) for particular experiments. Previous work has shown the necessity of characterizing the bandwidth of the resonator for optimal control pulses[17]. Additionally, the use of a resonator bandwidth correction has been shown to enhance the SNR for DEER experiments[13]. For experiments with many pulses, such as Carr-Purcell DEER[18], improving the performance of the pulses would have a much larger impact on the SNR for an experiment. The improvement in pulses is expected to have two primary effects, the improvement in SNR and the reduction in artifacts.

For all experiments, incomplete inversion over the desired frequency range results in a reduction in SNR either from incomplete refocusing of the electron spin echo or reduction in modulation depth. However, for certain experiments, incomplete inversion will result in experimental artifacts. Such is the case for SIFTER, where incomplete inversion of the 180°-pulses will result in oscillations at half the dipolar frequency. Another example is 5-pulse

DEER[34], where if the two pump pulses excite different populations of spins the signal will consist of a linear combination of 4-pulse DEER and 5-pulse DEER signals.

We focus on SIFTER and DEER measurements and investigate to what extent improvements in these experiments is possible with the calibration for the resonator bandwidth. We also show the excitation profiles of the calibrated pulses and demonstrate the improvement in the FT-echo once pulses are calibrated.

b) DEER Theory

i) Hamiltonian for weakly coupled electron spins.

In this section, we will briefly go through the key equations behind the DEER experiment. We will overview the dipolar Hamiltonian to demonstrate the DEER signal comes from an average over all orientations. Once we make the secular approximation, we can use the product operator formalism to calculate the outcome of a DEER measurement. The analytical equation for the DEER signal allows us to obtain a distance distribution from the time-domain DEER traces by Tikhonov regularization or an appropriate model fit.

The Hamiltonian for a pair of isolated spins S_A = ½ and S_B = ½ in the rotating frame is given by [35]

$$H = \Omega_A S_z^A + \Omega_B S_z^B + H_{dd} \tag{3.1}$$

In this equation, Ω_A (Ω_B) is the resonance offset for spin A (B), and S_z^A (S_z^B) is the spin operator for the z-component of the magnetization for spin A (B). H_{dd} is the familiar Hamiltonian from a magnetic dipole-dipole interaction[36]

$$H_{dd} = \frac{1}{r^3}\frac{\mu_0}{4\pi\hbar} g_A g_B \beta_e^2 \left[\boldsymbol{S}_A \boldsymbol{S}_B - \frac{3}{r^2}(\boldsymbol{S}_A \boldsymbol{r})(\boldsymbol{S}_B \boldsymbol{r})\right] \tag{3.2}$$

Where physical constants have their standard symbols, μ_0 is the magnetic permeability, $\hbar$ is Planck's constant divided by 2π, g_A and g_B are the g-factors for spin A and B, β_e is the Bohr magneton, $\boldsymbol{S}_A$ and $\boldsymbol{S}_B$ represent the spin vector operators for electron spin A and B, r is a scalar representing the distance between spin A and B, and $\boldsymbol{r}$ is a vector connecting spin A and B.

The Hamiltonian can be simplified if the difference in resonance offset for spin A and B is much greater than ω_{ee} ($|\Omega_A - \Omega_B| \gg \omega_{ee}$). In this case, we can ignore all non-secular terms in the Hamiltonian the Hamiltonian becomes diagonal

$$H = \Omega_A S_z^A + \Omega_B S_z^B + \omega_{ee} S_z^A S_z^B \tag{3.3}$$

For inter-spin distances greater than 2 nm, any contribution from exchange coupling to the dipolar frequency, ω_{ee}, can be neglected and ω_{ee} is given by

$$\omega_{ee} = \frac{1}{r^3}\frac{\mu_0}{4\pi\hbar} g_1 g_2 \beta_e^2 (3\cos^2\theta - 1) = \omega_{ee}^0 (3\cos^2\theta - 1) \tag{3.4}$$

Since the Hamiltonian in Eqn. 3.3 is already diagonal, the energy levels can be obtained directly from the diagonal elements. The energy level diagram for this system is shown in Figure 3.1(a). The line for each spin is split into a doublet separated by ω_{ee} (Figure 3.1(b)).

The angular dependence of the dipolar coupling gives rise to a Pake pattern when averaging over all possible orientations (Figure 3.2 (a-d)). The frequency difference between the two maxima in the Pake pattern, ω_{ee}^0, can be used to obtain an average distance for a given sample. Assuming a g-factor of 2.00, the distance between the two spins is:

$$r\ (\text{nm}) = \sqrt[3]{\frac{2\pi\ 52.04\ \text{MHz}}{\omega_{ee}^0}} \tag{3.5}$$

Now that we have shown the Hamiltonian for a weakly coupled pair of spin ½, we can use the result to calculate the outcome of the 4-pulse DEER pulse sequence and develop an understanding of the experiment.

ii) Pulse Sequence

The pulse sequence for 4-pulse DEER[27] uses a refocused Hahn echo sequence with an additional pump pulse (Figure 3.2). In this experiment, the positions of the observe pulses are held constant and position of the pump pulse is swept while the integral of the refocused Hahn echo is measured. To understand the pulse sequence, we begin by assuming both observe and pump pulses are selective for spins A and B, respectively. At the position of the first Hahn echo ($\pi/2$-t_1- π- t_1) all magnetization is refocused; at time t the pump pulse will invert spin B and cause a shift in the resonance offset of spin A by $\Delta\Omega_A = \omega_{ee}t$. Depending on the time, spin A will now only refocus if $\omega_{ee}t = n\pi$ ($n = 0,1,2$ ...). The resulting signal $V_{AB}(t)$ is therefore a cosine function which is indeed the result given by application of the product operator formalism

$$V_{AB}(t) = \cos \omega_{ee}t \tag{3.6}$$

The result above is only valid for an isolated spin pair. In macroscopic disordered samples, e.g. doubly labeled protein, we must consider all possible orientations (angle, θ) of the dipolar coupling. We take a powder average over a sphere to obtain the DEER signal.[35,37]

$$V_{\mathrm{DEER}}(t) = B(t)\left[1 - \lambda \int_0^{\pi/2} \sin(\theta)\,[1 - \cos(\omega_{ee}(\theta)t)]\,\mathrm{d}\theta\right] \tag{3.7}$$

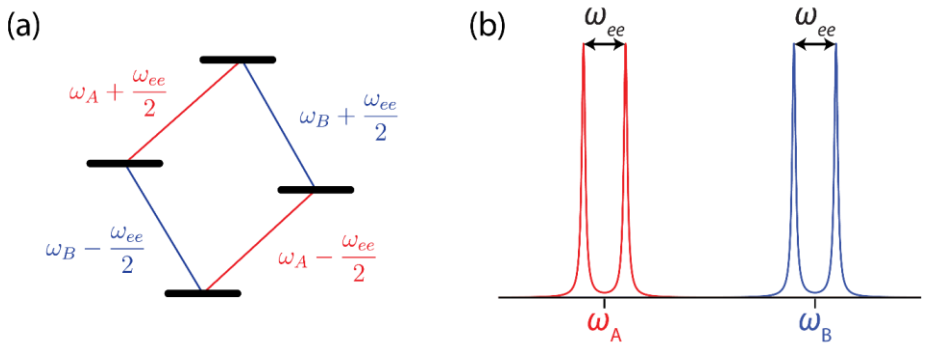

Figure 3.1 (a) Energy level diagram for two weakly dipolar coupled spins (S=1/2). Each line is split into two lines separated by $\boldsymbol{\omega_{ee}}$ (b) Typical spectrum of (a) showing each line split into doublet.*

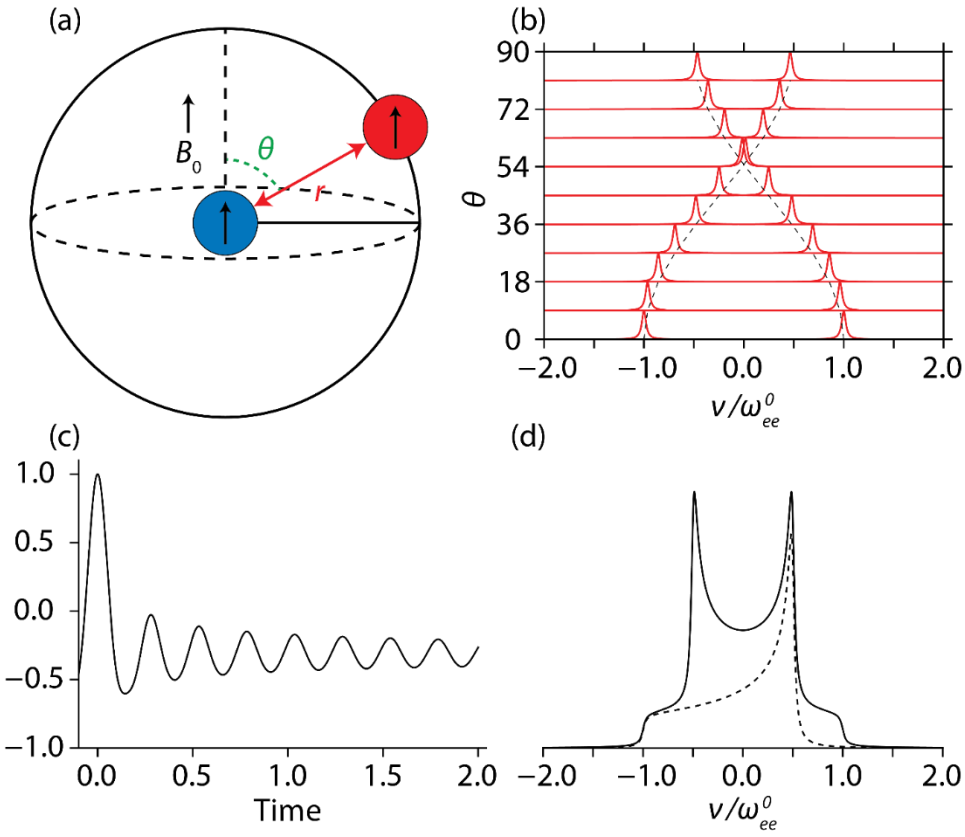

Figure 3.2 (a) Definition of $\boldsymbol{\theta}$ and $\boldsymbol{r}$. (b) Angular dependence of $\boldsymbol{\omega_{ee}}$ (c) Time domain DEER trace (d) Pake pattern (Fourier transform of time domain DEER).*

c) SIFTER Theory

The Hamiltonian for the SIFTER experiment is assumed to be the same as the DEER experiment. The SIFTER experiment is based on the solid echo experiment ($90°_x$- τ-$90°_y$-τ). This pulse sequence was developed for solid state NMR because it does not include additional relaxation from instantaneous diffusion.

Immediately after the first $90°_x$-pulse, the density matrix is given by:

$$\sigma_1 = \cos\left(\frac{\omega_{ee}}{2}\tau_1\right)\left(S_y^A + S_y^B\right) - \sin\left(\frac{\omega_{ee}}{2}\tau_1\right)(2S_z^A S_x^B + 2S_x^A S_z^B) \tag{3.8}$$

The $90°_y$-pulse at time $2\tau_1$ inverts the anti-phase coherence:

$$\sigma_2 = \cos\left(\frac{\omega_{ee}}{2}\tau_1\right)\left(S_y^A + S_y^B\right) + \sin\left(\frac{\omega_{ee}}{2}\tau_1\right)(2S_z^A S_x^B + 2S_x^A S_z^B) \tag{3.9}$$

At the detection time of $2(\tau_1 + \tau_2)$,

$$\sigma_4 = \cos\big(\omega_{ee}(\tau_1 - \tau_2)\big)\big(S_y^A + S_y^B\big) + \sin\big(\omega_{ee}(\tau_1 - \tau_2)\big) \times (2S_z^A S_x^B + 2S_x^A S_z^B) \tag{3.10}$$

The SIFTER Signal is therefore an oscillation at the dipolar frequency which depends on the difference $\tau_1 - \tau_2$.

d) Methods

i) Instrument

A commercial Bruker X-band ELEXSYS E580 spectrometer with SpinJet AWG module was used for all pulsed EPR experiments. The AWG module has 14-bit amplitude resolution

[*] Reprinted from Methods in Cell, Vol. 141, Y. Fichou, N.A. Eschmann, T.J. Keller, S. Han, Chapter 5 - Conformation-based assay of tau protein aggregation, 89-112, Copyright 2017, with permission from Elsevier.

(0-16383), a 1.6 GS/s clock (0.625 ns time resolution), +/- 400 MHz bandwidth around carrier, 80 ms of memory.

All measurements were performed with a Bruker MS3 Resonator.

A 16-step phase cycle for the SIFTER experiment will remove all unwanted echo crossings.

An 8-step phase cycle was used for DEER, but keep in mind that a 16-step phase cycle is required to remove all interfering echoes when coherent pump pulses are used.[38]

ii) Materials

Standard ruler molecules in DEER for NR118 (broadband echo and excitation profile), MS57-2 was used for DEER inversion comparison, NR119 was used for SIFTER vs DEER with calibrated pulses. For all samples 0.1 mg biradical was diluted in 1 g deuterated ortho-terphenyl. Biradical standards were heated to their melting point, then rapidly frozen in liquid nitrogen immediately before inserting into the resonator.

e) Results

i) Resonator Transfer Function

The fidelity of pulse shaping capabilities at microwave frequencies is limited by distortions to pulse shapes caused by microwave components in the pathway to the sample with the resonator accounting to the majority of the distortion. For precise control of a spin system, we must be able to account for the effects of various hardware components on the microwave pulses. From now on we will classify the transfer function as the resonator transfer function, but acknowledge this transfer function truly represents the transfer function of the entire spectrometer. In the simplest case, the microwave resonator transfer

function can be assumed to be an RLC circuit which has a Lorentzian transfer function, however, in practice, the transfer function is more complicated and should be measured empirically. The two main methods for measuring the transfer function of the resonator are by using a pick-up coil[17] or by transient nutation measurement of the B_1 as a function of frequency[13]. While the pick-up coil can measure the transfer function more rapidly by Fourier transform of the time domain response to a pulse, the pick-up coil will also have a transfer function and additionally will not account for the changes introduced by the sample. We therefore use a transient nutation method because it offers a direct measurement of the B_1 at the position of the sample and does not require any additional equipment.

The transient nutation method involves measuring the nutation frequency of the spins, ω_1, which can be directly used to calculate B_1.

$$\omega_1 = \frac{g\beta_e}{\hbar} B_1 \tag{3.11}$$

If necessary, B_1 can be related to the microwave power by the conversion factor, c, of the resonator, $P = (B_1/c)^2$. The transient nutation method will give us the absolute value of the $B_1(f)$. To obtain a complex transfer function, we can use the Kramers-Kronig (Bode) relation which with the assumption of minimum phase delay, connects the logarithm of the magnitude and phase by a Hilbert transformation.[39]

$$\angle G(\omega) = -\frac{2\omega}{\pi} P \int_0^\infty \frac{\ln|G(\omega')|}{\omega'^2 - \omega^2} d\omega' \tag{3.12}$$

Where $G(\omega')$ denotes the complex transfer function, $\angle G(\omega)$ is the phase of the transfer function, and P is the Cauchy principle value.

For systems with linear response, the time domain pulse shape is convolved with a time domain response function we call the resonator transfer function. The pulse shape at the

sample position therefore a convolution of the original pulse shape $f(t)$ and the transfer function of the system $g(t)$:

$$(f * g)(t) = \int f(t)g(t-\tau)d\tau \tag{3.13}$$

In frequency domain, we can use the property that the Fourier transform of the convolution is equal to the product of the Fourier transforms for the pulse shape and transfer function.

$$\Im\{f * g\} = \Im\{f\} \cdot \Im\{g\} \tag{3.14}$$

If the transfer function is known, we can pre-distort a pulse in frequency domain so that we achieve the desired pulse shape at the sample position.

$$f = \Im^{-1}\left\{\frac{\Im\{f * g\}}{\Im\{g\}}\right\} \tag{3.15}$$

To correct a pulse shape, we set $f * g$ equal to the desired pulse shape inside the resonator and since we have already experimentally determined $\Im\{g\}$, we can solve for f using Eqn. 3.15. Once the shape f is convolved by the transfer function of the resonator, g, it will have the desired spin response inside the resonator.

The pulse sequence for the transient nutation experiment is shown in Figure 3.3a. The length of the first pulse is incremented and followed by a Hahn echo sequence to read-out the z-magnetization. The time delay between the first pulse and the Hahn echo sequence, T, is set larger than the transverse relaxation time of the sample, T_2. Then the frequency of the microwave source (in this case the Gunn diode), ν, is stepped and the field is stepped by $\nu \times 2.83$ MHz/G to ensure the spins are always on resonance. The nutation experiment is repeated across the entire bandwidth of the resonator. Upon processing the data the nutation frequency, ν_1, is given as a function of frequency, as shown in Figure 3.3b. Figure 3.3c

shows the absolute value of the transient nutation experiments. The frequency of the nutation is obtained by Fourier transform and peak selection (Figure 3.3d).

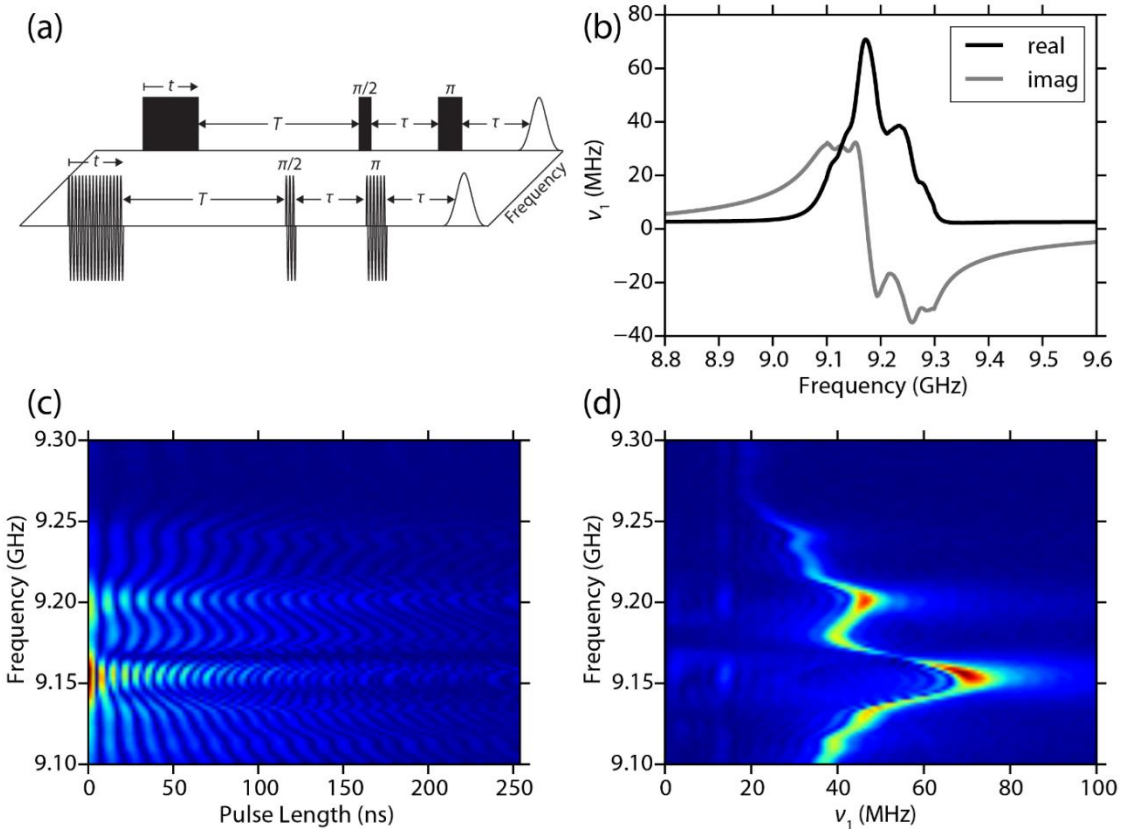

Figure 3.3 (a) Pulse sequence for transient nutation experiment used to measure transfer function of microwave resonator. The frequency of the microwave source and the field are varied simultaneously to always stay on resonance. (b) Real and imaginary components of resonator transfer function obtained by transient nutation experiment. (c-d) Experimental data from time-domain data and frequency-domain transient nutation experiment. Frequency domain data is the Fourier transform of the time domain data.

For typical samples, we find that the MS3 resonator transfer function is asymmetric with a roughly 115 MHz bandwidth (Q-factor of 80). To apply the transfer function to pulses shaped over the +/- 400 MHz bandwidth of the AWG, we fit the transfer function to a sum

of 4 Lorentzian functions and use the fit to recreate the transfer function outside the range of the experimental data. The nutation frequency is at the center of the tuning dip is 63 MHz giving a 180°-pulse length of roughly 8 ns.

Since the bandwidth of the nitroxide exceeds the bandwidth of the resonator, excitation over the full bandwidth of the resonator requires specially designed pulses which can compensate for the limited bandwidth of the resonator. In this work, we use pulses calibrated by applying the inverse transfer function of the resonator to the pulses. Measuring the excitation profiles of the pulse shapes will allow us to determine our ability to compensate for distortions of our pulse shape by the resonator transfer function.

ii) Measurement of Excitation Profiles

A pulse which is particularly useful for DEER is the adiabatic hyperbolic secant pulse. These pulses are known for their remarkable insensitivity to $\omega_1^{\max}$ beyond what is required for adiabaticity and sharp edges of the excitation profile which allow for selective excitation. The hyperbolic secant pulse is defined by:

$$\omega_1(t) = \omega_1^{\max}\left(\operatorname{sech}\left(\frac{\beta t}{t_p}\right)\right)^{1+i\mu} \tag{3.16}$$

Where t_p is the pulse length, β is a dimensionless constant defining the truncation of the pulse, and μ is a constant related to the bandwidth of excitation ($\mu = BW \times t_p/\beta$).

For a pulse to be adiabatic, the magnetization vector, $\boldsymbol{M}$, must follow the effective angular frequency vector $\boldsymbol{\omega}_{\text{eff}}$. The condition is met when the $|\boldsymbol{\omega}_{\text{eff}}|$ is much greater than, $|d\theta/dt|$, the instantaneous velocity of $\boldsymbol{\omega}_{\text{eff}}$:[13]

$$K = \frac{|\boldsymbol{\omega}_{\text{eff}}|}{|d\theta/dt|} \gg 1 \tag{3.17}$$

The relationship in Eqn. 3.17 is known as the "adiabatic condition". For hyperbolic secant pulses, the adiabatic condition varies during the duration of the pulse. In the particular case where the adiabaticity is offset-independent, the adiabaticity condition is proportional to:[14]

$$K_{\min} \propto \frac{2\pi\nu_1^2}{BW} \gg 1 \tag{3.18}$$

Although this is a specific case were the adiabaticity is independent of offset, it is still useful for analyzing the dependence of adiabaticity on power. In this case, the adiabatic condition scales with ν_1^2 and is therefore proportional to microwave power. As long as we have enough power, we can expect the adiabatic pulse to perform well and invert over the bandwidth of the pulse. However, outside the resonator bandwidth, where we are severely limited in power, the pulse will no longer be adiabatic.

To establish the performance increase obtained by calibrating pulses with the transfer function of the resonator, we measure the excitation profiles of broadband adiabatic pulses and compare with simulations. Excitation profiles are measured by a hole burning experiment. A static inversion pulse is followed by a Hahn echo read-out sequence. The microwave frequency of the source remains constant, while the frequency of the Hahn echo read-out sequence is swept simultaneously with the field. Echoes appear off-resonance from the carrier, but because the pump pulse remains constant, this allows us to measure the inversion profile of the first pulse. The data is processed by Fourier transforming the echoes, selecting an integration window around each peak, and integrating down the direct dimension. We repeat this experiment without the pump pulse, and obtain the hole burned by the inversion pulse. The Hahn echo read-out pulses are set long (100 ns and 200 ns) to ensure that we are only selecting a narrow bandwidth. One disadvantage of this method is

that the video amplifier bandwidth limits the range to a few hundred MHz where good SNR can be obtained.

For this particular experiment, we have chosen a 200 ns adiabatic pulse with a bandwidth of 300 MHz and β of $4/t_p$ (Figure 3.4a). This pulse was chosen because it exceeds the bandwidth of the nitroxide and transfer function and will allow us to determine the limits of what can be corrected.

The excitation profile (Figure 3.4b) of the uncorrected adiabatic pulse (Figure 3.4a) is highly distorted over the bandwidth of the resonator. The simulation matches the major features in the data, but appears to perform less well at negative frequencies where the transfer function is steep. Additionally, the dip in the excitation profile at 50 MHz corresponds to the dip in the transfer function and this can be used in DEER measurements to provide additional isolation between the pump and observe pulses. If the transfer function is applied to the pulse in Figure 3.4a, the effect is to scale the higher frequencies of the pulse (Figure 3.4c). This pulse has more power where the resonator would attenuate the pulse and has an excitation profile shown in Figure 3.4d. After correcting for the adiabatic pulse, the bandwidth of the pulse is greatly improved and we can exceed the bandwidth of the nitroxide spectrum at X-band. The dip is still present at 50 MHz, at this frequency where before we were not able to invert at all, we now have ≈70% inversion.

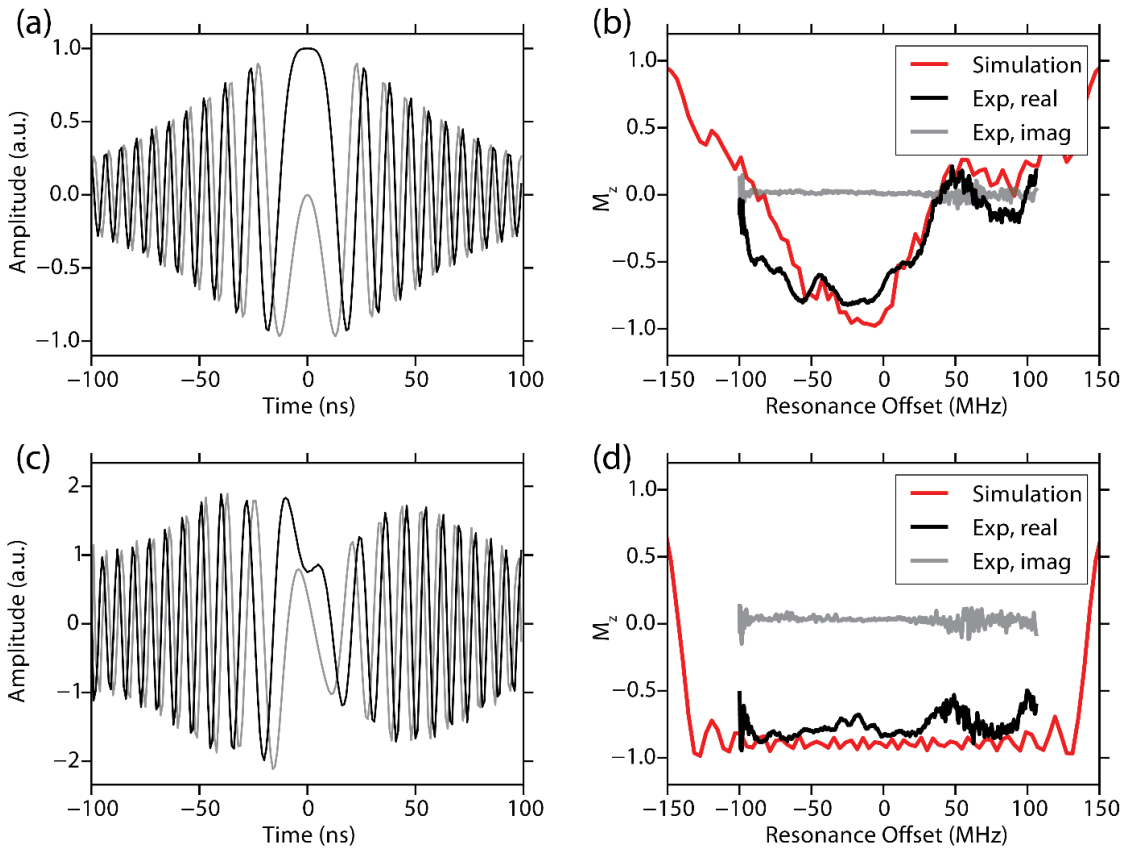

Figure 3.4 (a) Adiabatic pulse (t_p = 200 ns, BW = 300 MHz, $\beta = 4/\boldsymbol{t_p}$) uncorrected for resonator transfer function and (b) the experimental response. Simulations are shown in red. (c) Adiabatic pulse in (a) corrected for transfer function of resonator and (d) the experimental response. In all figures, black represents real part and gray represents imaginary part.

In the case where the adiabatic pulse is uncorrected, uniform excitation was not possible and inversion of the magnetization only takes place at roughly 100 MHz bandwidth, approximately half the spectral width of a nitroxide at X-band.

The calibration of pulses is useful in certain cases where we desire to excite beyond the bandwidth of the resonator, for example, the nitroxide spectrum. Experiments like DQC and

SIFTER, where each pulse must uniformly excite the same population of spins would benefit from pulses compensated for the resonator transfer function.

iii) Broadband Echo Measurements

At X-band, power limitations prevent hard pulses from fully exciting the >200 MHz bandwidth of nitroxide radicals[ref]. In fact, the full width half max even of a 180°-pulse of 6 ns that is beyond current state of the art technology would not even cover the whole spectrum. Instead, we must use excitation schemes which refocus the magnetization to the same position in time, such example is the Bohlen-Bodenhausen excitation. In this experiment (Figure 3.5a) a frequency swept 90°-pulse is followed by a 180°-pulse with the same frequency sweep in half the time and twice the amplitude. This ensures that the phase (or frequency) dispersion created by the first pulse will be completely refocused by the second pulse so that all magnetization is refocused at the same point in time. The requirement that the amplitude of the 180°-pulse is half the 90°-pulse is inconvenient because it prevents us from utilizing the full power of the amplifier, however this is the simplest pulse sequence to generate a broadband refocused echo. Additionally, the concept of Bohlen-Bodenhausen can be extended to other pulse sequences like SIFTER and DQC to refocus the magnetization with frequency swept pulses.

For nitroxides, the width of an echo is determined primarily by the bandwidth of the 180°-pulse. With the typically used 16, 32 ns pulses the width of the echo is approximately 50 ns. The Bohlen-Bodenhausen excitation scheme results in a much narrower and higher intensity echo in time domain compared to the one obtained with square pulses, conforming the successful broadband excitation. In addition a profound effect on the excitation bandwidth was observed when the transfer function correction was implemented. The

broadband echo from uncorrected pulses had a of 22 ns, while the echo from corrected pulses had a width of 12 ns based on the FWHM. In addition, the echo from calibrated pulses has more resolved features in the time domain which comes from the fact that more frequencies are recovered in the time-domain data.

The Fourier transform of the echo should resemble the field swept echo detected EPR spectrum (FSE) of the nitroxide. In Figure 3.5c, we show the absolute value of the Fourier transforms of the echo and compare with the FSE. The Fourier transforms have been scaled by the transfer function of the resonator to prevent any influence of the transfer function on the echo shape. The hard pulses produce a Gaussian excitation Fourier transform. The calibrated broadband produce a significantly broader Fourier transform spectrum than the uncalibrated pulses. This is expected based on the performance of the broadband pulses in the excitation profile (Figure 3.4d).

Improvements in the bandwidth of our pulses can be immediately applied to improve the performance of certain pulsed EPR experiments. For these experiments we will utilize the Bohlen-Bodenhausen excitation scheme where broad band frequency swept pulses are used and the pulse durations are selected such that the magnetization is refocused at the echo-time over the whole bandwidth. We will address the issue of incomplete excitation of the frequencies outside the resonator bandwidth by applying the transfer function correction and evaluate the associated performance gain.

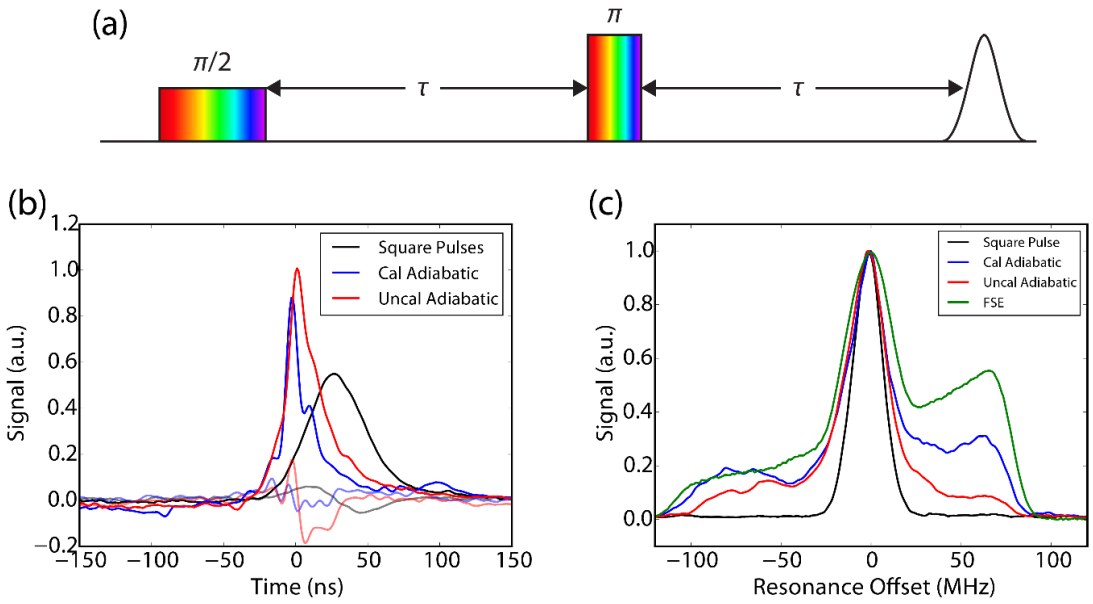

Figure 3.5 (a) Bohlen Bodenhausen excitation scheme for Hahn echo. (b) Comparison of Hahn echo shapes for square pulses, calibrated adiabatic pulses, and uncalibrated adiabatic pulses. (c) Fourier transform of Hahn echoes in (b) and compared to field swept echo.

iv) DEER with Broadband Pulses

The pulse sequence for DEER is shown in Figure 3.6a. The pulse sequence consists of a refocused Hahn echo with an additional pump pulse between the two 180°-pulses. The signal to noise ratio (SNR) for the DEER measurement is proportional to the fraction of spins excited by the pump pulse. The development of AWG capabilities immediately gives a straightforward method to improve the SNR by pumping on a larger fraction of the nitroxide spectrum using a broadband pulse. The shaped pulses for use in the DEER experiment are designed to maximize modulation depth and minimize overlap with the observe pulses.

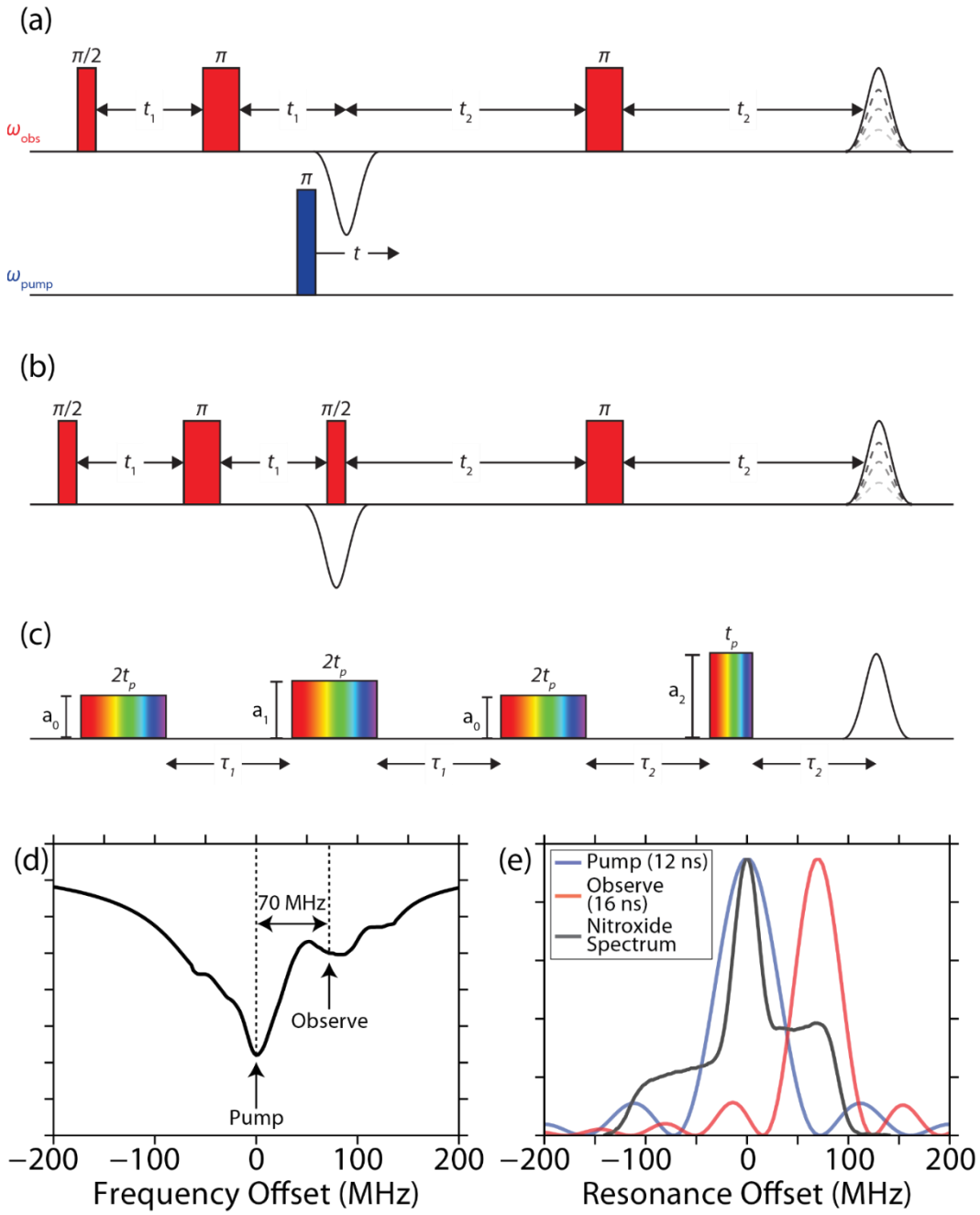

Figure 3.6 (a) Pulse sequence for 4-pulse DEER experiment. (b) Pulse sequence for SIFTER experiment. (c) Excitation scheme for the 4-pulse DEER measurement at X-band. (d) Overlap of excitation profiles of standard length square pulses and nitroxide spectrum.

Typically, the pump frequency is chosen to at the center of the tuning dip and the maximum of the nitroxide spectrum to ensure maximum modulation depth (Figure 3.6c-d). Compared with hard pulses, it is possible to more than double the modulation depth of a DEER measurement if a broadband pump pulse is chosen. Observing off the center of the tuning dip decreases the intensity of the echo signal, but this loss in SNR is made up for in increased modulation depth. In Fig 3.7, we compare the performance of a 12 ns square pulse to a 180 MHz Chirp pulse. The modulation depth for the chirp pulse is 60% where the modulation depth for the 12 ns square pulse is 30%. By simply using a shaped microwave pulse, we have doubled the SNR for the DEER measurement.

We next apply our broadband calibrated pulses to DEER measurements to test the improvement in performance of calibrated pulses. The performance increase is minimal because when the pump pulse is at the center of the tuning dip, we are already able to excite the major part of the nitroxide spectrum. Regardless, a small increase in the modulation depth from 57.1% to 57.3%. Figure 3.7a. This is because we the pump pulse is centered with the center of the resonator tuning dip where even the uncorrected chirp-pulse has high efficiency.

The distance distributions for all the fits are performed with LongDistances software and the model free fit with a smoothing parameter of 1. Both uncalibrated and calibrated pulses give the same distance distribution, however, the calibrated pulse gives a slightly cleaner distance distribution with no artifacts. The cleaner distance distribution may be due to less artifacts with calibrated pulses or perhaps a slight boost in SNR.

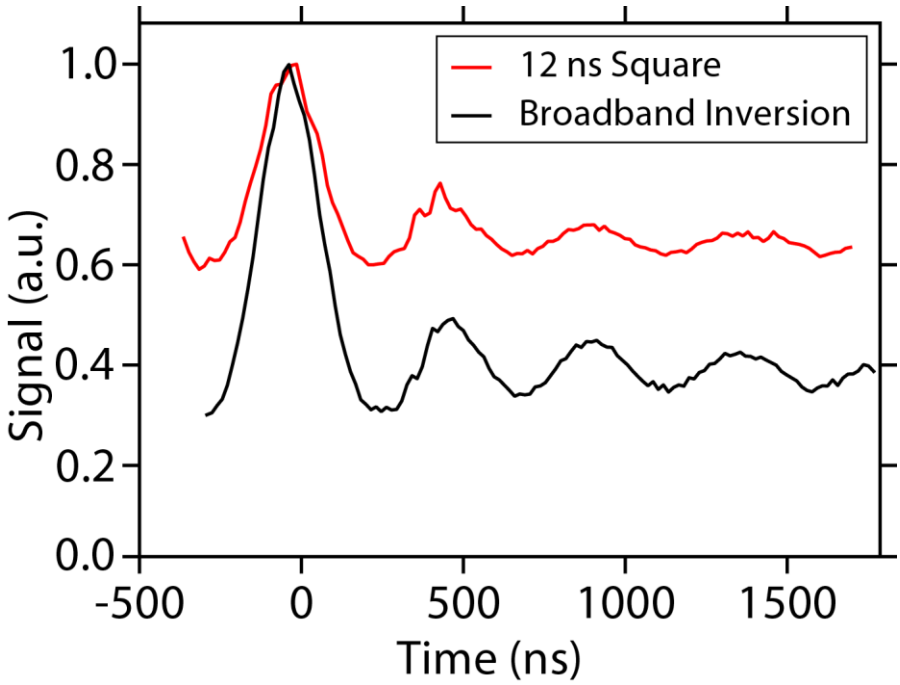

Figure 3.7 DEER traces for 2.8 nm standard ruler. Broadband inversion is able to achieve roughly a factor of 2 improvement in modulation depth. The artifact at 400 ns is caused by coherent pump pulse while using only 8-step phase cycle.

v) SIFTER with Broadband Pulses

An alternative method for measuring the inter-spin dipolar interaction is the SIFTER pulse sequence, shown in Figure 3.6b. It is based on the solid echo pulse sequence known in solid-state NMR. In this sequence, a $90_x°$-pulse is followed by a $90_y°$-pulse with two additional 180°-pulses. The addition of two 180°-pulses is necessary to make the experiment a constant time experiment so that any change in the echo intensity by incrementing $|t_1 - t_2|$ ($t_1 + t_2 = \text{constant}$) is due to dipolar coupling. The 180°-pulses also ensure that all resonance offsets are refocused at the time of the $90_y°$-pulse and the position of the echo. The spin physics behind the pulse sequence can be understood by ignoring the 180°-pulses and considering only the $90_x°$- and $90_y°$-pulses. After the first $90_x°$-pulse, the dipolar

coupling term causes anti-phase coherence to be generated, the $90_y°$-pulse is critical in inverting the sign of the anti-phase term and preventing the coherence to be completely refocused at the time of the echo. The echo will only refocus when $\cos(\omega_{ee}(t_1 - t_2)) = 1$, where ω_{ee} is the dipolar coupling frequency between the two electron spins. Similar to DEER, the dipolar frequency can be related to a distance distribution.

The SIFTER pulse sequence with broadband pulses (Figure 3.6c), is similar to the pulse sequence with hard pulses (Figure 3.6b), however, we must satisfy the criterion where all the various resonance offsets refocus at the position of the echo. Once such pulse length ratio is 2:2:2:1 and shown in Figure 3.6c. The frequency dispersion for this sequence is carried until the last 180°-pulse, where it is refocused to generate an echo at time t_2 after pulse.

One challenge associated with the introduction of AWG capabilities is the vast increase in number of parameters that determine the pulse sequence. possible and finding the global minimum can be tedious. Nevertheless, we can optimize the most important parameters first in an intuitive way. For the SIFTER experiment, we are using 400 ns and 200 ns adiabatic pulses with 300 MHz bandwidth and a β/t_p of 4. Such pulses are broad enough to excite the entire nitroxide spectrum, but still long enough to remain adiabatic. There are three pulse amplitudes, a_1, a_2, and a_3, which must be defined in the pulse program (see Fig 2.6c for definitions). In the case where $|t_1 - t_2| = 0$, we have the optimal performance when the SIFTER echo signal is maximized. For the last pulse (the half-length pulse) the echo is maximized when a_3 is 100% because this inversion pulse is half the length of the other pulses and therefore requires more power to remain adiabatic Eq 6. The other two amplitudes, a_1 and a_2, are optimized by performing a two dimenstional experiment and varying the amplitude of the pulses and observing the echo signal. Typical values for a_1 and

a_2 are 25% and 65%, respectively. It is interesting that the inversion pulse is not optimized at 100% amplitude as we would expect that from a hyperbolic sech pulse, the performance should only increase with power. However, because these pulses have limited adiabaticity due to the bandwidth of the resonator, their performance may not be expected to equal the ideal case.

For SIFTER with broadband pulses, the increase in performance and modulation depth with calibrated pulses would be expected to be much greater than DEER. The imperfections of each pulse excitation will be compounded throughout the pulse sequence, and improvement in excitation efficiency would be expected to boost both modulation depth (improvement in $90_y°$-pulse) and increased echo amplitude (more complete refocusing with 180°-pulses). As expected, the performance increase with calibrated pulses is much higher than in DEER, with an increase in modulation depth from 80.6% to 86.5% when broadband pulses are calibrated. In the calibrated experiment, the oscillations are profound enough to go negative. For this sample, the improvement in modulation depth is the main reason why the SNR is better for SIFTER than DEER. The increase in modulation depth for SIFTER compared with DEER is apparent from Figure 3.8. For uncalibrated and calibrated pulses this amounts to a 40% and 50% increase in SNR. The contribution to modulation depth for SIFTER is now from the entire nitroxide linewidth and this is one of the main advantages of SIFTER over DEER. In addition, because the contribution to instantaneous diffusion is less for SIFTER, it is particularly promising for systems with high local concentrations of spins such as aggregating systems and membrane proteins. The last subtle advantage of SIFTER is because, unlike DEER, we are observing on the center of the tuning dip, this increase the amount of echo signal we observe.

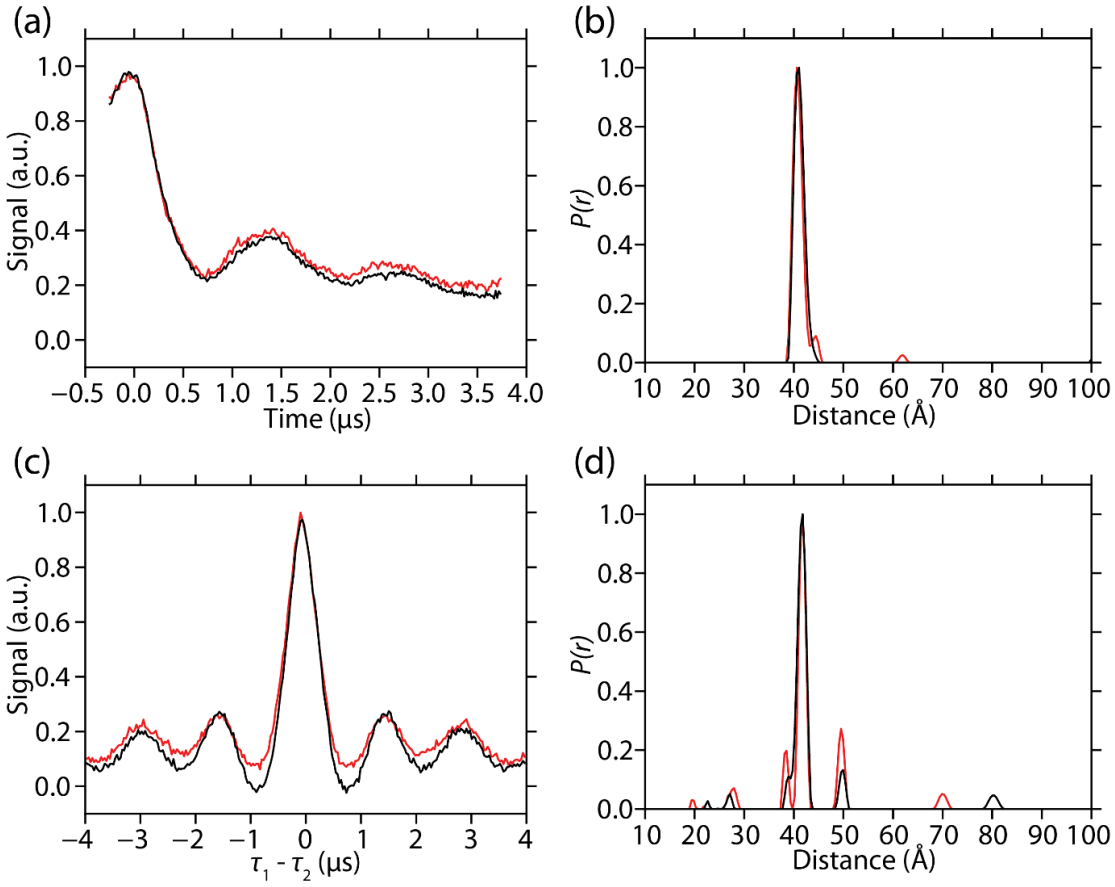

Figure 3.8 (a) DEER experiment showing difference between calibrated (black) and uncalibrated (red) adiabatic pump pulse. (b) Distance distribution from (a). (c) SIFTER experiment comparing calibrated (black) and uncalibrated (red) adiabatic pulses. (d) Distance distribution from (c).

The main disadvantage of SIFTER is the introduction of an artifact at half the dipolar frequency if the 180°-pulses do not invert the same population as the 90°-pulses. From the distance distribution in Figure 3.8d, we can see a number of small contributions outside the expected distance of 4.1 nm. The largest unwanted peak occurs at 5 nm and this is a result of the half frequency artifact. In addition, there is a peak at 2.8 nm which comes from the Larmor frequency of deuterium at X-band. Unfortunately, these artifacts in SIFTER are a result of spin physics which cannot be removed by phase cycling. One technique for

removing the ESEEM modulation is by incrementing $t_1 + t_2$ and averaging the results. The nuclear modulation is present in all traces, but the phase depends on $t_1 + t_2$. To remove proton modulations, an increment of $\Delta(t_1 + t_2)$ of 8 ns should be chosen and for deuterium modulations an increment of 56 ns should be chosen.[9] In this work, 8 increments of 56 ns were chosen to remove the deuterium modulations. A promising result is that by calibrating the pulses, we see a reduction in the number of artifacts for SIFTER and further reduction could be possible with increased pulse performance.

vi) DEER vs SIFTER on realistic samples

So far, we have shown an improvement in SNR for a biradical standard. The improvement in performance for SIFTER experiments relative to DEER must also be demonstrated on realistic protein samples. We investigate the performance of SIFTER on the challenging protein sample, tau protein which is an intrinsically disordered protein involved in the formation of amyloid plaques characteristic of Alzheimer's disease. This protein is particularly difficult to study because of its broad distance distribution and short T_m after aggregation.

The comparison between DEER and SIFTER on tau is shown in Figure 3.9a. In both cases, pulses are calibrated by the resonator transfer function. The modulation depth is not as large as the biradical standard because the spin labeling efficiency for these samples is only ≈50%. The SNR is better by a factor of 2.5 for SIFTER compared to DEER. The primary reason for the improvement in SNR in this case is that for SIFTER we are observing the echo at the center of the tuning dip and also at the center of the nitroxide spectrum.

The advantage of SIFTER over DEER is improved modulation depth and overall SNR improvement because of an increased observe echo amplitude. For protein samples with

limited SNR, the maximum dipolar evolution time is limited. In cases with short maximum dipolar evolution times, the nuclear modulation artifact is much more pronounced (Figure 3.9b). The signal to noise for SIFTER is significantly better than DEER by a factor of 2.5. However, the nuclear modulation artifacts in the SIFTER are pronounced.

While the SNR is better for SIFTER, the artifacts make the determination of distance distribution unreliable for this sample. Until the performance of the pulses is improved to a point where the artifacts are removed, SIFTER will not be a reliable method for measuring the distance distribution on protein samples. At X-band nuclear modulation artifacts are present in both DEER and SIFTER. In DEER it arises from frequency domain overlap of the pump and observe pulses. For SIFTER, because it is always pumping on the same spins, the ESEEM is an intrinsic part of the experiment and arises from spin physics.

Removing the y-pulse and repeating the experiment to only obtain ESEEM is possible way to remove ESEEM artifacts, the other method is the do an average of 8 sweeps with an increment in 56 ns (X-band deuterium).

f) Discussion

The development of broadband microwave resonators will become increasingly important for pulsed EPR applications as AWG capabilities allow for broad excitation bandwidths, while still maintaining high conversion efficiency.[33] This will become particularly important as AWG capabilities are extended to the higher frequencies of Q-band (34 GHz) and W-band (94 GHz). For X-band measurements, the bandwidth of the Bruker MS3 resonator has a Q-factor of approximately 50-100 at maximal overcoupling depending on the particular resonator and sample. With this Q-factor, the bandwidth of the resonator

approaches the bandwidth of the nitroxide radical and it is possible to obtain FT-EPR spectra for nitroxides with broadband echoes.

Measurement of the resonator transfer function offers an insight into the range with which pulse shapes can be corrected. If the B_1 at a certain frequency is too low, no amount of correction will be able to recover the ability to invert spins at this frequency. For our measurement of the transfer function, a Q-factor of 80 indicates that within a window of +/- 57.5 MHz (ν_1 FWHM = 115 MHz), where the pulse is attenuated by at most half, we should be able to invert very well. Outside this bandwidth, the calibration of pulses becomes increasingly important for broadband pulses. The bandwidth of our maximally overcoupled MS3 resonator is fairly typical, however, it is sometimes possible to have a Q-factor of 50.[13] A interesting advantage of this resonator is the bimodal character of the tuning dip offers an advantage for DEER measurements because the dip in power can be used to increase isolation between the pump and observe pulses.

For measurement of the excitation profiles, we use a hole burning experiment where the pump pulse is held constant and the echo detection sequence is swept simultaneously with the field. We argue this is a better measurement of the "true" excitation profile of the spins because we directly measure the M_z as a function of microwave frequency. Alternatively, sweeping the pump pulse directly while fixing the Hahn echo detection sequence can also provide an indication of the pulse bandwidth[13], this does not offer an indication of performance outside the bandwidth of the resonator. Alternatively, an attenuated pulse with a small tip angle pulse in the linear regime will generate an excitation profile.[12] Measurement of the excitation profiles allows us to gauge the performance of the pulses. This is particularly important in experiments where uniform excitation over the entire

bandwidth of the pulse is important to eliminate artifacts in the signal (e.g. FT-EPR and SIFTER).

Since the bandwidth of the nitroxide exceeds the bandwidth of the resonator, excitation over the full bandwidth of the resonator requires specially designed pulses which can compensate for attenuation outside the bandwidth of the resonator. Measuring the transfer function by transient nutation and directly correcting the pulse shape can be shown to improve the performance of adiabatic pulses for a number of pulsed EPR experiments including broadband echoes and SIFTER.

Broadband echo measurements on nitroxides are approaching comparable consistency with field swept echo measurements. One advantage of broadband echo measurements is the larger amplitude and narrower width of the echo enables the integration window for certain experiments to be reduced and potentially offers an improvement in SNR. The signal to noise improvements will be better for experiments which don't have complications for swept pulses, for example the DEER experiment at higher fields. The improvement in echo amplitude of 1.6 and 1.8 relative to square pulses is consistent with previous broadband echoes using the Bohlen-Bodenhausen excitation scheme.[40] The improvement in calibrated broadband pulses shows that the inversion pulse performs much better outside the 115 MHz bandwidth of the microwave resonator.

The minimal improvement in performance of DEER with calibrated pulses is due to the fact that we are pumping on the maximum nitroxide signal and center of the tuning dip already where we are already inverting spins very efficiently. While the improvement in performance is not substantial for X-band, it is possible that at higher frequencies (e.g. Q-band) where the spectrum is even broader, could have more of an improvement by exciting

more efficiently outside the bandwidth of the resonator. In addition, the bimodal character of the MS3 resonator transfer function works in the favor of DEER measurements, because when we observe +65 MHz off of the center of the tuning dip, we actually are at a maximum of the 2nd mode of the resonator.

For the case of SIFTER, the improvement in SNR over DEER is highly desirable, however, we cannot compromise SNR for the introduction of artifacts into the distance distribution. Further optimization of the inversion pulses would be necessary to make this experiment competitive with DEER on protein samples. The nuclear modulation artifacts present in SIFTER would be less prominent at Q-band, which offers a promising. The calibration of pulses used for SIFTER can be easily other distance measurements such as "2+1", RIDME, and DQC.

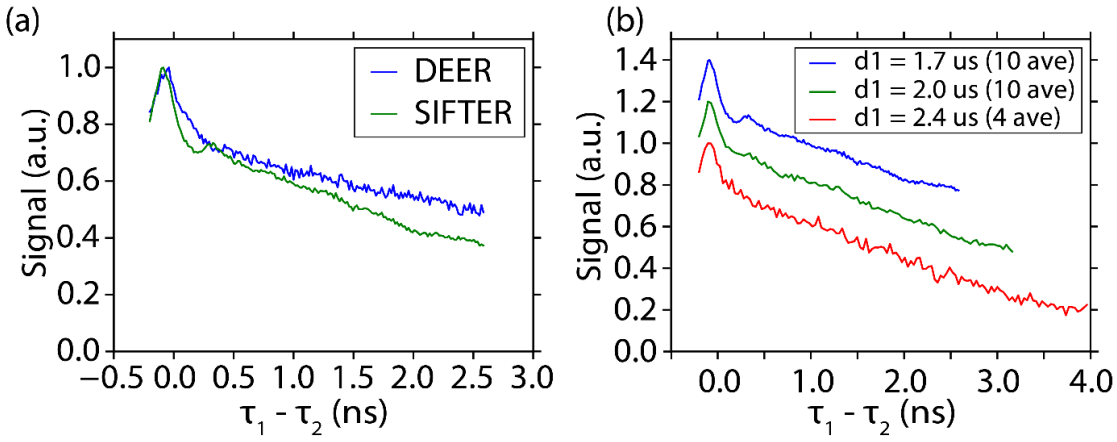

Figure 3.9 (a) DEER and SIFTER on tau187 G272C S285C. Artifacts are caused by deuterium ESEEM. (b) SIFTER traces on tau187 obtained by extending the length of the SIFTER experiment and showing the gradual removal of deuterium ESEEM artifact.

g) Conclusion

The advancement in sub-nanosecond arbitrary waveform generators has allowed for pulse shaping capabilities to be extended to pulsed EPR measurements. These pulse shaping capabilities have already shown significant improvement to distance measurements like DEER[13,16] where simple improvement in pulse bandwidth can have significant improvements on the experiment. For experiments like SIFTER and 5-pulse DEER[34] where complete inversion is necessary to reduce the number of artifacts, ensuring that the pulses are performing over the entire bandwidth of the resonator is critical. By characterizing the resonator transfer function, pulse shapes will be corrected by the Characterizing the resonator transfer function and correcting the corresponding pulses is necessary to prevent experimental artifacts.

Once we have developed the capabilities of AWG pulses, it becomes possible to use experiments otherwise not possible or improve experiments that were previously not possible. The difference in SIFTER and DEER is a very interesting one because it prevents us from fully understanding the limitation in SNR between SIFTER and DEER. There are a few technical reasons why SIFTER would be expected to give better SNR than DEER, but the primary reason is improved modulation depth and also observing on the center of the tuning dip (and nitroxide radical) where more signal can be detected. The greatest improvement in SNR is often going to be the case for samples with higher spin label concentration or less dimensionality. For example, sifter has less instantaneous diffusion than DEER, which may account for the improvement in SNR for high spin label concentrations.

4) Optimization of Q-band DEER Experiments

DEER distance measurements on nitroxide radical pairs at Q-band (34 GHz) have vastly improved SNR over X-band (10 GHz).[30] To further push the capabilities of pulsed EPR experiments on the most challenging protein systems, it is therefore necessary to develop AWG capabilities at Q-band. We therefore optimize the performance of Q-band pulsed EPR experiments with a 300 W TWT amplifier. This is the first Q-band pulsed AWG EPR spectrometer with a 300 W TWT (instead of 150 W) and showcase the improvements possible by optimization of the pump pulse and tuning procedure.

a) Excitation Scheme for Q-band DEER

The nitroxide spectrum is broader at Q-band than X-band due to increased g-anisotropy (Figure 4.1). While this makes exciting the entire nitroxide spectrum more challenging, experiments like DEER where we pump and observe on different regions of the spectrum. The typical method for excitation at Q-band involves only pumping on a small percentage of the spins, however, with arbitrarily shaped pulses, a frequency swept pump pulse covering 80-90% of the entire spectrum can be achieved (Figure 4.2).

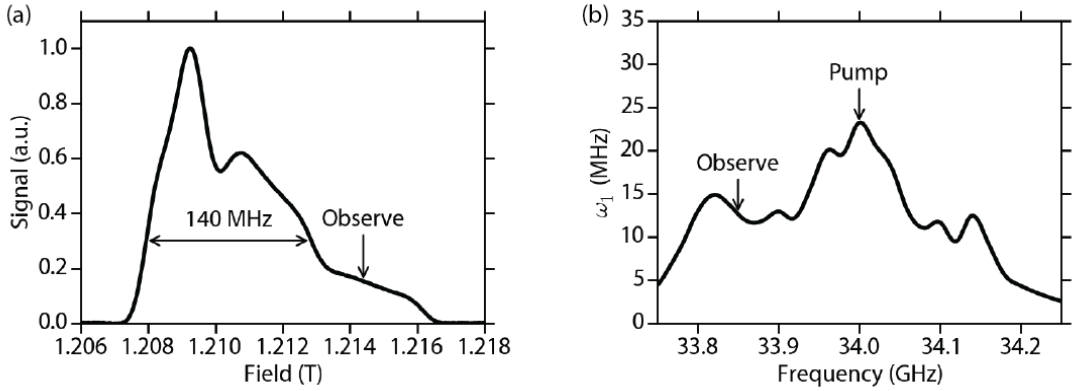

Figure 4.1 (a) Q-band field swept echo for typical nitroxide spectrum. (b) Typical resonator transfer function for Bruker QT-II resonator.

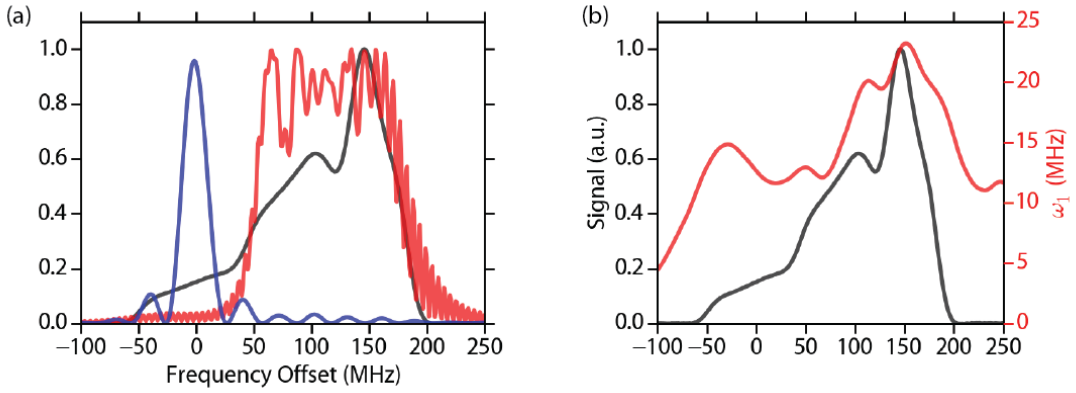

Figure 4.2 (a) In frequency domain, the Q-band nitroxide spectrum (black) overlapped with the excitation profile of a 40 ns square observe pulse (blue), and a 100 ns chirp pump pulse (red). (b) The frequency domain nitroxide spectrum (black) overlapped with the transfer function of the Bruker QT-II resonator (red).

b) Optimization of Tuning Procedure

The Bruker QT-II resonator profile is a bimodal and the two dips can to a large extent be independently positioned by adjusting the coupling arm and cavity length. DEER was performed with chirp pulses with three different mode separations (Figure 4.3). A summary of SNR and modulation depth for the DEER experiments is shown in Figure 4.4. The overall SNR for a DEER experiment depends on both the modulation depth and the intensity of the detected echo. For all experiments, the modulation depth increased as the length of the pump pulse was increased which resulted in a corresponding increase in SNR. The best SNR overall was obtained when the mode separation was 180 MHz, however, this was only approximately 5% better than the 200 MHz separation. This result can be explained by a balance between the power for the two modes being approximately equal when the separation is 180 MHz (Figure 4.3). If the modes are brought closer or further apart, one mode begins to dominate, so that the DEER signal no longer has as large of modulation depth or echo intensity.

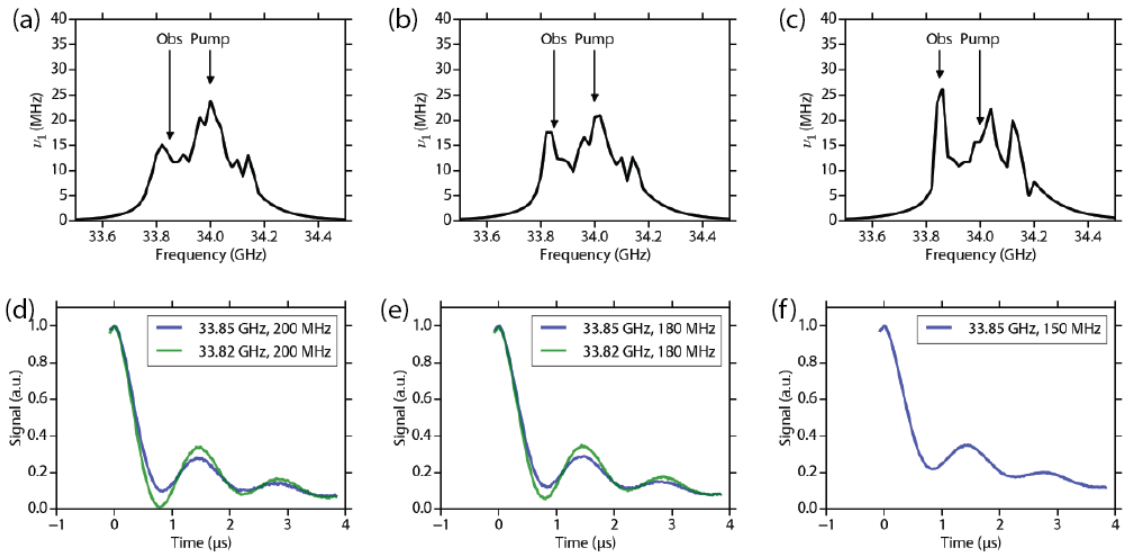

Figure 4.3 (a)-(c) Bruker QT-II resonator transfer function for three different separations of the two resonator modes. The separations are (a) 200 MHz, (b) 180 MHz, and (c) 150 MHz. (d)-(f) DEER signal with 200 ns chirp pump pulse for corresponding mode separations in (a)-(c).

c) Optimization of Pulse Shape

Some of the most common shaped pulses for broadband excitation in magnetic resonance include tanh/sech adiabatic pulses, chirp pulses, and WURST pulses. We have tested each of these pulses as pump pulses for the DEER experiment at Q-band in an effort to optimize the overall SNR of the DEER experiment.

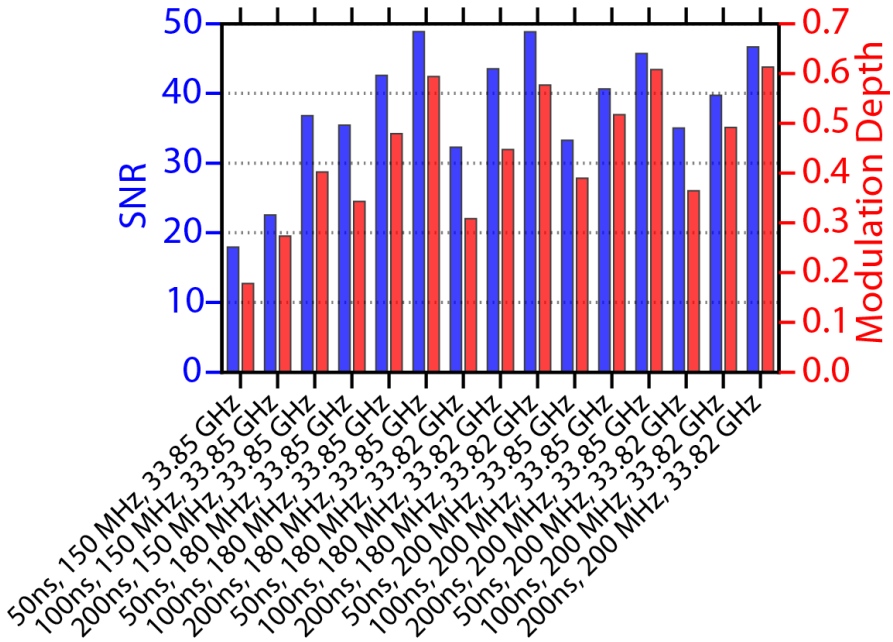

Figure 4.4 Bar graph showing the signal to noise and modulation depth for each tuning procedure. The x-axis labels indicate the pulse length, tuning mode separation, and observe frequency, respectively.

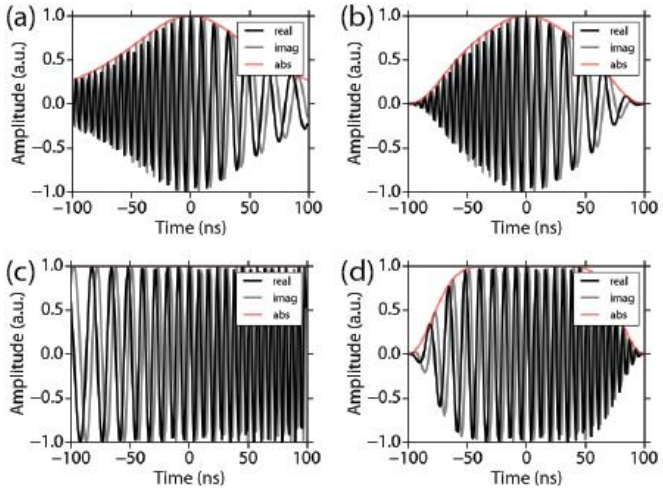

Figure 4.5 Pulse shapes chosen for optimization of DEER experiment. (a) Adiabatic (b) Adiabatic WURST (c) Chirp (d) WURST.

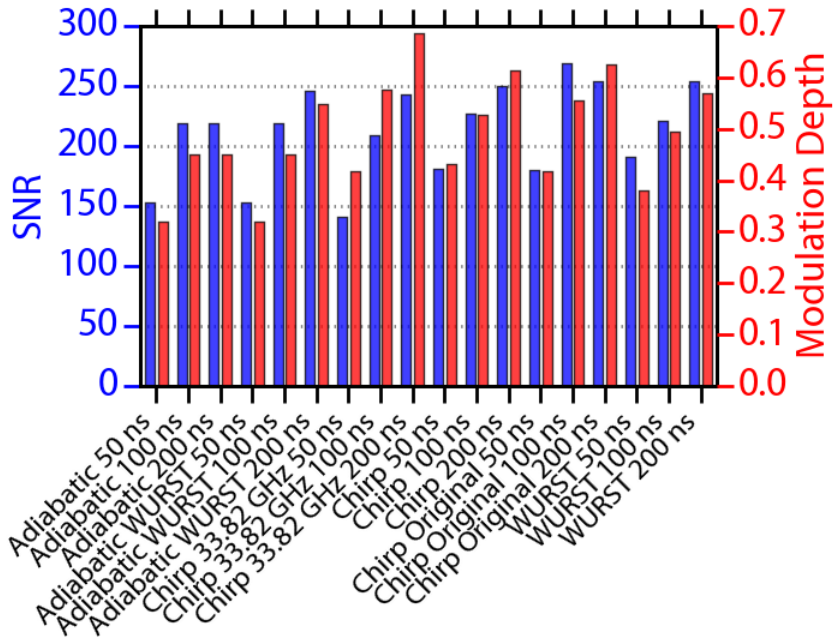

Figure 4.6 Bar graph showing the signal to noise and modulation depth for various DEER pump pulses.

d) Reliability of Distance Distributions

The maximum reliable distance which can be measured by DEER is related to the maximum dipolar evolution time (Figure 4.7). To be able to distinguish the dipolar oscillations from the background signal, we must have at least a full oscillation within the time domain DEER signal. More oscillations will improve our ability to resolve the width and the shape of the distance distributions. As a general rule, distances above 5 nm are challenging to resolve the width and shape of a distance distribution, however, the mean peak position reliable up until 6-7 nm.[9]

The dipolar frequency scales with $1/r^3$ which means that to measure twice the distance, one bust acquire $2^3 = 8$ times the maximum dipolar evolution time. For example, a 4 nm

distance distribution can be measured with a ~4.5 us dipolar evolution time, but a 5 nm distance requires a 9 us dipolar evolution time.

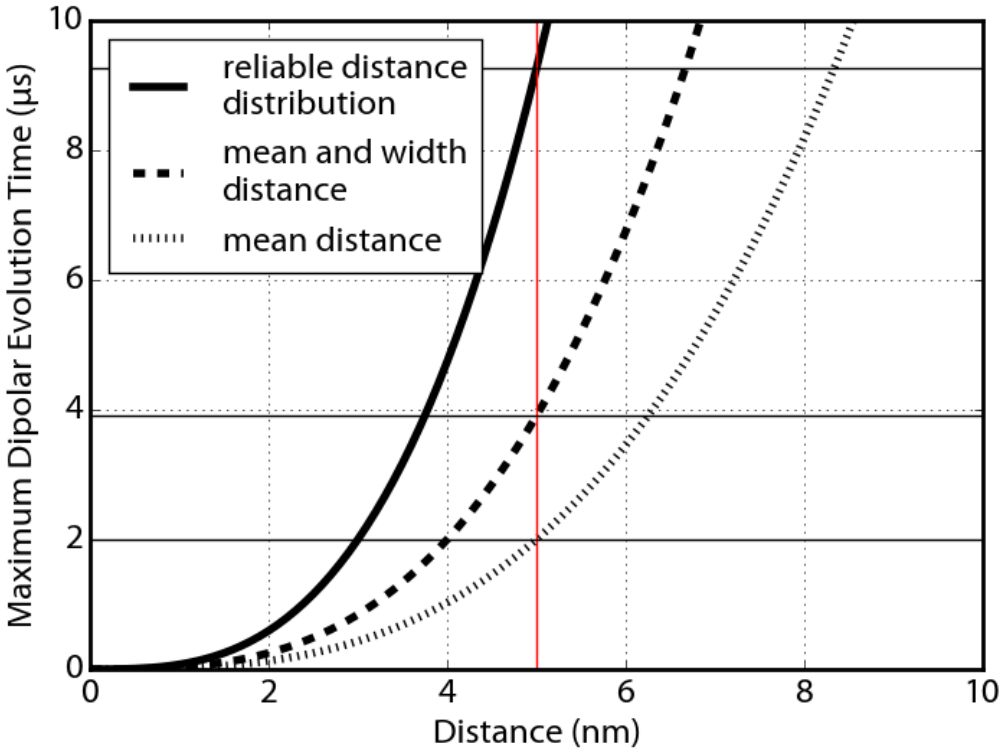

Figure 4.7 Maximum dipolar evolution time required to accurately measure "reliable distance distribution", "mean and width distance" and "mean distance." These values are calculated based on the number of dipolar oscillations (periods at a given dipolar frequency).

e) Optimization of protein concentration

The optimum protein concentration is obtained by optimizing the impact of the background function on the DEER signal (Figure 4.8).[26] For spins homogenously distributed, the background signal is an exponential decay with a time constant inversely proportional to the spin concentration in the sample. Therefore, if one wants to measure

extremely long distances, one must reduce the protein concentration to decrease the effect of the background on the DEER trace.

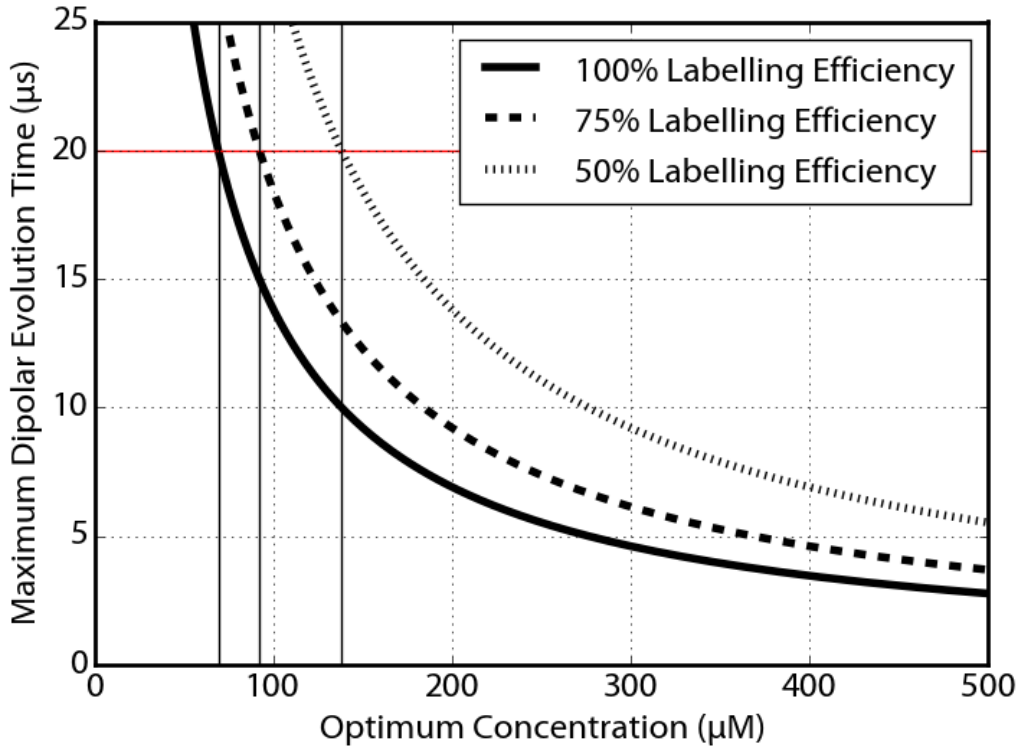

Figure 4.8 Optimum doubly labelled protein concentration for a desired dipolar evolution time.

f) Increasing Maximum Dipolar Evolution Time

The maximum dipolar evolution time which is possible to measure is determined primarily by the T_2 relaxation time. It is therefore a concern to find a method to increase the T_2 if possible. The T_2 is primarily determined by the electron spin concentration and the hyperfine interaction between the electron spins and the nuclei in the sample. Decreasing the concentration of electron spins and substituting deuterium for protons in the sample are the most common ways of extending the T_2 for the sample. In addition, increasing the amount of

cryoprotectant prevents ice crystals from forming upon freezing which cause spins in the sample to bunch closer together.

The effect of deuterated glycerol on extending the T_2 for a deuterated tau protein sample is shown in Figure 4.9. The T_2 does not increase above a glycerol concentration of 30%.

The effect of sample deuteration on the T_2 is shown in Figure 4.10. All samples contained deuterated water, but note how the deuteration of the glycerol cryoprotectant has a dramatic increase in the overall T_2 of the sample. Further increase in T_2 is observed if full deuteration of the protein is achieved, however the impact on the SNR improvement is minimal until maximum dipolar evolution times > 8 us are required.

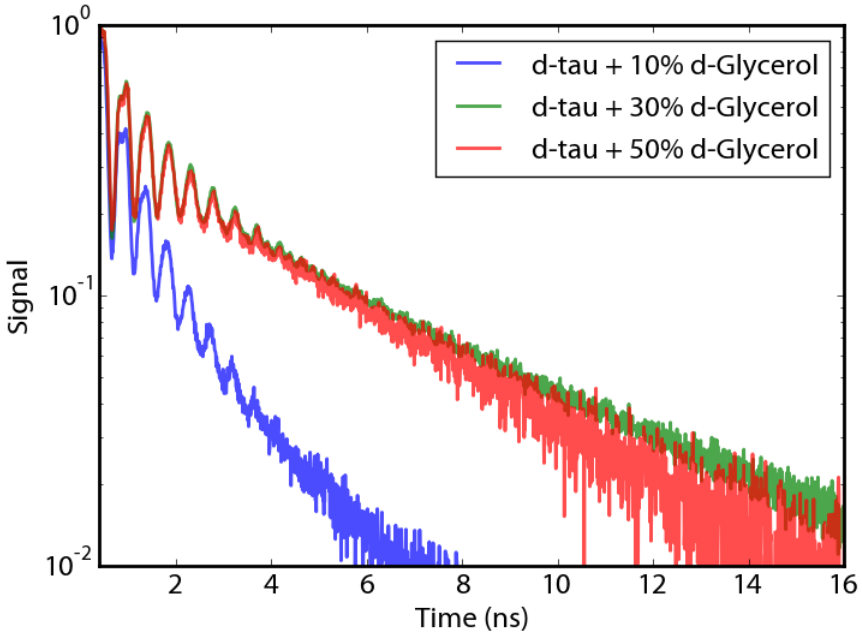

Figure 4.9 Hahn echo decays for difference concentrations of deuterated glycerol.

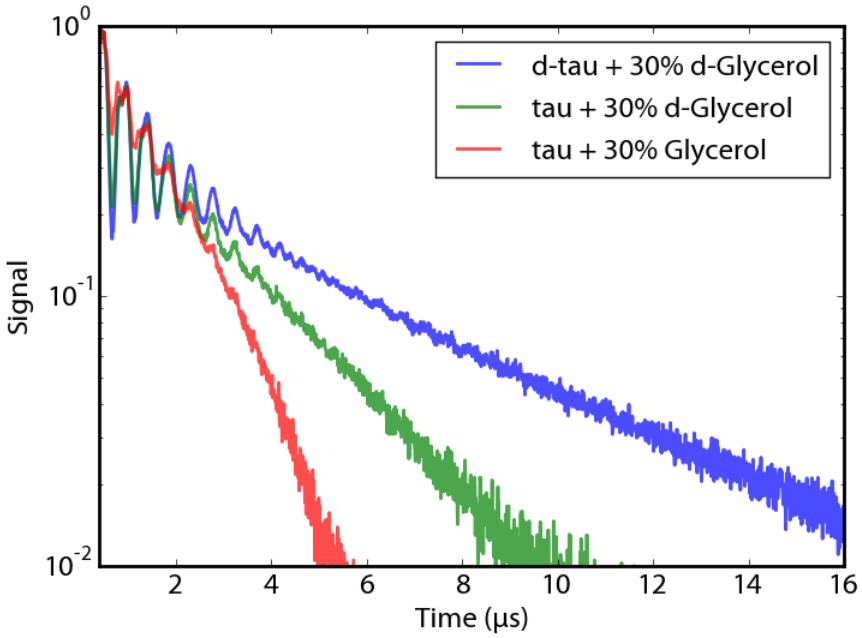

Figure 4.10 Hahn echo decays showing difference in relaxation times due to extent of deuteration.

5) ODNP and ESEEM Water Accessibility Measurements

In the search for unraveling functional properties from the structure or surface chemistry of biomolecules, the role of the structure and dynamics of the solvent water dynamically coupled to the biological surface is widely regarded as an important or even critical link. Here, the combination of Overhauser dynamic nuclear polarization (ODNP) and electron spin echo envelope modulation (ESEEM) at 0.35 Tesla magnetic field of ^{1}H nuclear spins of water is employed to study both the translational diffusion dynamics and the local density of water within sub-nanometer distances of a stable nitroxide radical-based spin probes. In this study we aim to answer the simplest question whether and to what extent global changes in ^{1}H density within the same bulk water mixtures of H_2O and D_2O affects ^{1}H ODNP-derived diffusion dynamics of water, as probed with 4-hydroxy TEMPO probes dissolved in this aqueous bulk solution. This simple model system allows us to vary the concentration of ^{1}H while keeping the hydration dynamics largely unaltered. The ESEEM results show that the distance of closest approach is independent of the H_2O/D_2O concentration (~3.8 Å), while the number of proximal water molecules increases approximately linearly with H_2O concentration, as expected. Concurrently, we find the ^{1}H ODNP coupling factor of water to be insensitive to H_2O concentration above 30% (v/v), but to rapidly decrease and approach zero below this threshold concentration. This shows that ^{1}H ODNP reports on the dynamics of water and is not sensitive to the extent of hydration, as long as the spin probe is located on fully solvent-exposed locations and environments, but that it is very sensitive to ^{1}H density in local environments devoid of H_2O, which may be globally or locally confined environments, including surface crevices. This clarifies the outlook for ODNP as a precise

tool for probing surface water dynamics and ESEEM for concurrently reporting on the surface hydration number of the same spin-labeled system.

a) Introduction

Although the exact role of water in facilitating protein function is highly debated and controversial, the importance of water in modulating biomolecular structure and function is unequivocal.[41] Specifically, the layer of water in the immediate vicinity of a biological molecule, termed biological water, yields distinctly different properties from bulk water.[42–47] The shell of water around a biological molecule constitutes a matrix that facilitates the inter- and intra- molecular interactions between biomolecules and surfaces, and without it the description of the interacting system would be incomplete.[48] It is of course this layer of water that must be relinquished for substrates to bind, oligomers to form, and protein folding to take place. The stronger the dynamic coupling between the hydration water and the surface—requiring adhesive and cohesive interactions involving the hydration water, the greater the retardation in the diffusivity of hydration water; this is expected to concur with the observation of a repulsive hydration layer whose dehydration is energetically costly. An example of such a surface is found with the charged unilamellar liposome surface. Differences in the retardation factor for surface water diffusivity is expected to influence the kinetics and/or favorability for protein folding, aggregation or binding events that require local or concurrent dehydration at the interface. Thus, both the diffusion dynamics and density of the water around the biomolecular site of interest are relevant reporters of binding and folding processes and of the nature of the hydrated surfaces themselves.[49–52]

However, experimental methods for directly reading out the solvent density and dynamics—reflecting on the dynamic structure—of hydration water coupled to biomolecular

surfaces in dilute solution-state and with site-specificity are still in their infancy and require further developments. Here, the combination of Overhauser dynamic nuclear polarization (ODNP) and electron spin echo envelope modulation (ESEEM) at 0.35 Tesla magnetic field of ^{1}H nuclear spins of water provides the opportunity to study both the translational diffusion dynamics, and the local density, of water within sub-nanometer distances of stable nitroxide radical-based spin probes specifically tethered to the molecular surface of interest. ODNP has proven a powerful tool for studying the local hydration dynamics around a spin label.[53,54] Still, it is uncertain is to what extent the coupling factor obtained by ^{1}H ODNP is purely reporting on the dynamics of the local hydration water, or is convoluted with the distance or accessibility of the electron spin probe relative to the water's ^{1}H nuclei. This knowledge is especially important in the case of partially buried spin labels, where the local diffusivity of water and the average spin label-water distance may be altered. In fact, the effect of water accessibility at different length scales from several nanometers down to several Angstrom may be fundamentally different, especially when the length scale of surface accessibility competes with the size of the water molecule or bond. The question is whether ODNP can report on local water diffusivity in partially confined or dehydrated environments, and if so, down to what level of water depletion? In the limit where the local environment of the electron spin label is sufficiently devoid of water, ODNP effects are sensitive to the distance of closest approach of water according to the dependence of the dipolar correlation time between the electron spin probe and ^{1}H nuclei, as will be discussed. This illustrates the importance of concurrently measuring and knowing the effect of the electron spin-^{1}H nuclear spin distance of closest approach, as well as the local ^{1}H water number density. This is, in fact, provided with a powerful pulsed EPR technique, electron

spin echo envelope modulation (ESEEM), that uniquely reports on the local water structure in disordered systems and specifically allows us to obtain the average number of waters around the spin label, as well as an approximate Van der Waals distance to non-hydrogen bonded waters.[55] Specifically, ESEEM allows for quantification of the hyperfine couplings to solvent nuclei around an electron spin. Therefore, the water density of the given solvent, local volume or surface site of interest is localized using an intrinsic paramagnet, an extrinsically introduced spin probe or a surface tethered spin label—the latter two cases typically achieved with stable nitroxide radical-based molecules. The modulation depth (k) of the ESEEM signal is proportional to the number of nuclei (N) divided by the distance (r) to the 6th power ($k \propto N/r^6$).[35,55] Additionally, the distance from the electron spin to the nuclei can be inferred from the dampening of the ESEEM signal. Thus, we can simultaneously determine both the distance and number of nuclei using an appropriate model.[56] The use of a "ratio analysis" model was used by Ichikawa, et al. to extract structure information from solvated electrons in 2-methyltetrahydrofuran glass.[57] More recently, ESEEM has been applied to investigate a number of systems including the local environment/solvent around metal ions[57–59], inside membranes[60,61], around proteins[55,62,63], inside nanochannels[64], and in bulk solution[57,65]. Also, the complimentary use of ODNP and ESEEM has been showcased to study the nanocavity of chaperoin protein GroEL, to find that the cavity inner wall is weakly hydrated, and that the water density and dynamics does not change upon closing of the nanocavity with GroES[62]. However, a systematic investigation that addresses the sensitivity of the ODNP-derived local water diffusivity on the local water number density and electron spin-^{1}H number density versus the local water diffusivity.

In this study we aim to answer first the simplest question whether and to what extent global changes in ^{1}H density within the same bulk water mixtures of H_2O and D_2O affects ^{1}H ODNP data, as probed with 4-hydroxy TEMPO probes dissolved in this aqueous bulk solution. Answering this is the prerequisite for studying the effect of variation in surface topology on ^{1}H ODNP-derived hydration dynamics data in the future. This simple model system allows us to vary the concentration of ^{1}H while keeping the hydration dynamics largely unaltered. We find the ^{1}H ODNP coupling factor of water to be insensitive to H_2O concentration above 30% (v/v), but to rapidly decrease and approach zero below this threshold concentration. This shows that ^{1}H ODNP reports on the dynamics of water and is not sensitive to the extent of hydration, as long as the spin probe is located on fully solvent-exposed locations and environments, but that it is very sensitive to ^{1}H density in local environments devoid of H_2O, which may be globally or locally confined environments, including surface crevices. To analyze the ESEEM data, we assume a spherical shell of water molecules around the spin label and verify that the distance of closest approach is independent of the H_2O/D_2O concentration (~3.8 Å), while the number of proximal water molecules increases approximately linearly with H_2O concentration—yielding the expected result. This clarifies the outlook for ODNP as a precise tool for probing surface water dynamics and ESEEM for concurrently reporting on the surface hydration number of the same spin-labeled system.

b) Theory

i) ODNP

The translational (and rotational) motion of water molecules in liquid water allows for polarization transfer from the spin label to water ^{1}H. Upon microwave irradiation, the modulation of the hyperfine interaction due to the relative translational diffusion of a spin label and ^{1}H nuclei in water allows forbidden transitions which result in the polarization transfer from the spin label and ^{1}H. The transfer in polarization results in enhancement of the ^{1}H NMR signal which can be measured and related to the dynamics of the water. Experimentally, we measure the enhancement in NMR signal, E, as a function of microwave power. If we extrapolate to infinite microwave power, the enhancement approaches a maximum value at which the electron spin is saturated and the electron saturation factor, s, reaches a maximum value.

$$1 - E = k_\sigma s T_1 C_{SL} \left|\frac{\omega_e}{\omega_H}\right| \tag{5.1}$$

$$k_\rho = \frac{1}{T_1} - \frac{1}{T_{10}} \tag{5.2}$$

$$\frac{k_\sigma}{k_\rho} = \xi \tag{5.3}$$

The enhancement of ^{1}H signal is measured in the presence and absence of microwave can be measured

Where ξ, the coupling factor, is the ratio of the electron-nuclear spin cross relaxation rate and the nuclear spin relaxation rate from the electron. This term contains all the dynamical information of the coupled electron-^{1}H spin system, e.g. the translational correlation times of water molecules. The coupling factor can be understood as the

efficiency of the dipolar cross relaxation between the nuclear spins and the electron spin. The parameter f is referred to as the leakage factor and accounts for the additional relaxation of protons in close proximity to electron spins. The parameter s is the electron saturation factor which ranges from zero in the case of no saturation to unity in the case of complete saturation. The saturation factor depends on both microwave power and spin label concentration. At low spin label concentration (<100 μM) the saturation factor has a value of approximately 1/3, and strong Heisenberg exchange will drive the saturation factor to approximately 1 at high concentrations of spin label (>100 mM).[53,66] The term $\left|\frac{\omega_e}{\omega_H}\right|$ is the ratio between the electron and proton Larmor frequencies and is approximately 659 for nitroxides in aqueous solution.[53,67]

To obtain the value for the enhancement, we measure the ^{1}H NMR signal as a function of microwave power. By extrapolating the enhancement to infinite microwave power, we obtain the maximum value for the enhancement at the maximum value for s. The maximum value for s is known for a given concentration of spin label[53]. The leakage factor is given by $f = 1 - T_1/T_{10}$ where T_1 and T_{10} represent the longitudinal relaxation times in the presence and absence of spin label, respectively.

Once *E*, *f* and *s* are quantified, the coupling factor can be obtained and related to the translational correlation time of the water, τ_c (or more specifically protons on water molecules):

$$\xi = \frac{6J(\omega_e - \omega_H; \tau_c) - J(\omega_e + \omega_H; \tau_c)}{6J(\omega_e - \omega_H; \tau_c) + 3J(\omega_H; \tau_c) + J(\omega_e + \omega_H; \tau_c)} \qquad (5.4)$$

Where $J(\omega;\tau_c)$ is the spectral density function for the system, which we assume to be the spectral density function given by the force free hard sphere model of Hwang and Freed.[68,69]

Solving the above equation for τ_c, allows us to obtain the translational correlation time. The translational correlation time depends on both the distance to which the ^{1}H can approach the spin label, called the distance of closest approach d, and the relative diffusion coefficient of the water and spin label $D_I + D_S$:

$$\tau = \frac{d^2}{D_I + D_S} \tag{5.5}$$

The distance of closest approach has been previously determined to be roughly 3.4 Å. To interpret the translational correlation time as a quantity which purely reflects the water dynamics, we must be sure that the distance of closest approach is invariable for a given spin label regardless of the system studied.

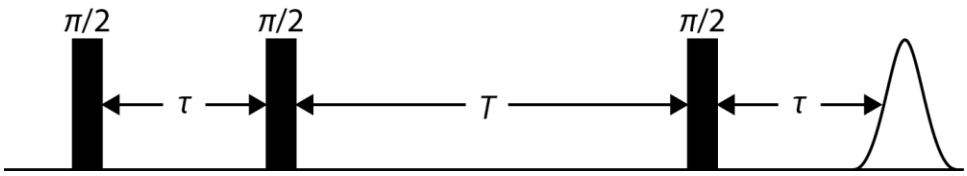

Figure 5.1 Pulse sequence for 3-pulse ESEEM measurement. All pulses are π/2 pulses. The value of $\boldsymbol{\tau}$ is fixed while $\boldsymbol{T}$ is incremented. The height of the center of the echo is monitored as a function of $\boldsymbol{T}$.

ii) ESEEM

The 3-pulse ESEEM sequence is shown in Figure 5.1. ESEEM allows for the quantification of weak hyperfine couplings which are normally too small to observe in the

CW-EPR spectra of radicals. ESEEM relies on forbidden transitions. One of the few techniques which is able to obtain local structure information in disordered systems.

We will consider the 3-pulse ESEEM signal for a S=1/2 electron spin and a I=1 spin nuclei (e.g. deuterium). If we neglect the quadrupolar interaction, which is a reasonable assumption for matrix nucleus around the nitroxide radical, the 3-pulse ESEEM signal for a single interacting nuclei is given by:[65]

$$V_{3p}(\tau,T)=\frac{1}{2}\left[V_{\alpha}(\tau,T)+V_{\beta}(\tau,T)\right] \tag{5.6}$$

Where V_{α} and V_{β} are given by[56,61]

$$V_{\alpha}(T)=1-\frac{16}{3}k\sin^{2}\left(\frac{\omega_{\alpha}\tau}{2}\right)\sin^{2}\left(\frac{\omega_{\beta}(\tau+T)}{2}\right)+\frac{16}{3}k^{2}\sin^{4}\left(\frac{\omega_{\alpha}\tau}{2}\right)\sin^{4}\left(\frac{\omega_{\beta}(\tau+T)}{2}\right) \tag{5.7}$$

$$V_{\beta}(T)=1-\frac{16}{3}k\sin^{2}\left(\frac{\omega_{\beta}\tau}{2}\right)\sin^{2}\left(\frac{\omega_{\alpha}(\tau+T)}{2}\right)+\frac{16}{3}k^{2}\sin^{4}\left(\frac{\omega_{\beta}\tau}{2}\right)\sin^{4}\left(\frac{\omega_{\alpha}(\tau+T)}{2}\right) \tag{5.8}$$

The parameters k, ω_{α}, and ω_{β} have their standard definitions[35]

$$k=\left(\frac{\omega_{\mathrm{I}}B}{\omega_{\alpha}\omega_{\beta}}\right)^{2} \tag{5.9}$$

$$\omega_{\alpha}=\sqrt{\left(\omega_{I}+\frac{A}{2}\right)^{2}+\frac{B^{2}}{4}} \tag{5.10}$$

$$\omega_{\beta}=\sqrt{\left(\omega_{I}-\frac{A}{2}\right)^{2}+\frac{B^{2}}{4}} \tag{5.11}$$

Where,

$$A = a_{iso} + T_d(3\cos^2\theta - 1) \tag{5.12}$$

$$B = 3T_d \sin\theta \cos\theta \tag{5.13}$$

$$T = \frac{\mu_0}{4\pi\hbar}\frac{g_e\beta_e g_n\beta_n}{r^3} \tag{5.14}$$

For our system, we must consider the effect of many interacting nuclei. In most cases inter-nuclear interactions are much weaker than electron-nuclear interactions, in this case, the ESEEM signal from N nuclei is given as the product of the individual ESEEM signal from each spin manifold (α and β). The ESEEM signal for N interacting nuclei then becomes:

$$V_{3p,N}(\tau, T) = \frac{1}{2}\left[\prod_{i=1}^{N} V_{\alpha,i}(\tau, T) + \prod_{i=1}^{N} V_{\beta,i}(\tau, T)\right] \tag{5.15}$$

For our simulations, we will assume that the ensemble signal is given by nuclei which are evenly distributed on a spherical shell with radius r:[35,57]

$$\begin{aligned}\langle V_{3p,N}(\tau, T)\rangle = \frac{1}{2\pi}\int_0^{\pi/2} \sin\theta\, d\theta \int_0^{2\pi} \frac{1}{2}\left[\prod_{i=1}^{N} V_{\alpha,i}(\tau, T, \theta, \phi)\right. \\ \left. + \prod_{i=1}^{N} V_{\beta,j}(\tau, T, \theta, \phi)\right] d\phi\end{aligned} \tag{5.16}$$

If the positions of the nuclei are uncorrelated, as is expected for a random matrix, we can take the product over all nuclei outside the integral and the expression becomes:

$$\langle V_{3p,N}(\tau,T)\rangle = \frac{1}{2}\prod_{i=1}^{N}\int_0^{\frac{\pi}{2}}\sin\theta\, V_{\alpha,i}(\tau,T,\theta,\phi)\,d\theta + \frac{1}{2}\prod_{i=1}^{N}\int_0^{\frac{\pi}{2}}\sin\theta\, V_{\beta,i}(\tau,T,\theta,\phi)\,d\theta \tag{5.17}$$

Finally, we assume all nuclei lie at the same distance from the electron spin and can simplify this expression to:

$$\langle V_{3p,N}(\tau,T)\rangle = \frac{1}{2}\left\{\left[\int_0^{\frac{\pi}{2}}\sin\theta\, V_{\alpha}(\tau,T,\theta,\phi)d\theta\right]^{N} + \left[\int_0^{\frac{\pi}{2}}\sin\theta\, V_{\beta}(\tau,T,\theta,\phi)d\theta\right]^{N}\right\} \tag{5.18}$$

The ESEEM data is modelled by the above equation, were the number of nuclei by numerically integrating over the spherical shell, we are able to model the ESEEM data and simultaneously obtain both the number of nuclei,N, and the distance from the electron spin to the nuclei, *r*.

There are a number of assumptions which are made in the derivation of the ESEEM signal which require further comment. First, the positions of the nuclei should be uncorrelated; An assumption which is not necessarily valid for glasses which retain long range order. Also, the assumption that all nuclei are equidistant from the electron spin is certainly contentious; however, we expect that the first solvation shell will contribute to ~90% of the total ESEEM signal. This can be argued by the fact that the modulation depth (k) of the ESEEM signal is proportional to N/r^6 and the number of nuclei on a spherical shell increases with the area of the sphere goes with r^2. The net effect is that the ESEEM

signal will depend roughly on $1/r^4$.[35,55] In closing, the reasonableness of assumptions and model is judged by how well our model fits the data.

c) Experimental

i) Chemicals

All samples were prepared with 500 μM 4-hydroxy TEMPO (Sigma-Aldrich 176141). Deuterated water (99.9% deuterium) was purchased from Cambridge Isotope Laboratories, Inc. (DLM-4-100). For pulsed EPR measurements, samples were prepared with 10% glycerol to act as a glassing agent during liquid nitrogen quench. Preparation of spin labelled polystyrene and silica beads can be found in the supplementary information of a previous publication.[70] All materials were used as purchased without further purification.

ii) Pulsed EPR

Pulsed EPR measurements were performed on an ELEXSYS E580 spectrometer with an Oxford Instruments cryostat (CF935P) and temperature controller (ITC503). All pulsed EPR measurements were performed at 50 K. For a resonator, a commercial Bruker MS3 resonator was used. The pulse lengths for 90- and 180-pulses were set to 16, and 32 ns, respectively, and the attenuation was adjusted to give the maximum echo signal. For 3-pulse ESEEM measurements ($\pi/2$-τ- $\pi/2$-T- $\pi/2$-τ-echo) the delay between 2nd and 3rd pulses was incremented from a starting value of 400 ns to 8160 ns in steps of 32 ns for 256 total points. The delay τ between 1st and 2nd pulses was fixed to 140 ns, which corresponds to a blind spot for proton ESEEM. A 4-step phase cycle was used to remove DC offset and unwanted echoes. The ESEEM data was corrected for background decay by fitting to a 5th degree

polynomial, subtracting the polynomial fit, and then dividing by the polynomial fit. The ESEEM data was modelled according the spherical shell model with in-house Python code.

iii) ODNP

Overhauser DNP measurements were performed with an X-band Bruker EMX 0.35 T electromagnet and Bruker 4119HS resonator, corresponding to a 14.8-MHz proton Larmor frequency and 9.8 GHz electron Larmor frequency. The NMR signal was acquired with a Bruker Avance 200 NMR spectrometer with X-channel. A sample volume of 3.5 µL was loaded into a 0.6 mm ID quartz capillary (VitroTubes CV6084Q-100). One end of the capillary was sealed with critoseal and the other end was sealed with wax. The sample tube was inserted into a home-built U-shaped NMR coil and the coil was placed into the microwave resonator. The home-built NMR coil has been described previously.[53,71] The center transition of the nitroxide spectrum was irradiated continuously with linear power while the proton NMR signal was recorded. To cool the sample during microwave irradiation, air was continuously flowed around the sample through the EPR cavity. The diffusion coefficients of H_2O and D_2O are very similar, however, to account for small differences the ODNP data was corrected using a viscosity of 1.0016 mPa·s for H_2O and 1.2467 mPa·s for D_2O.

d) Results

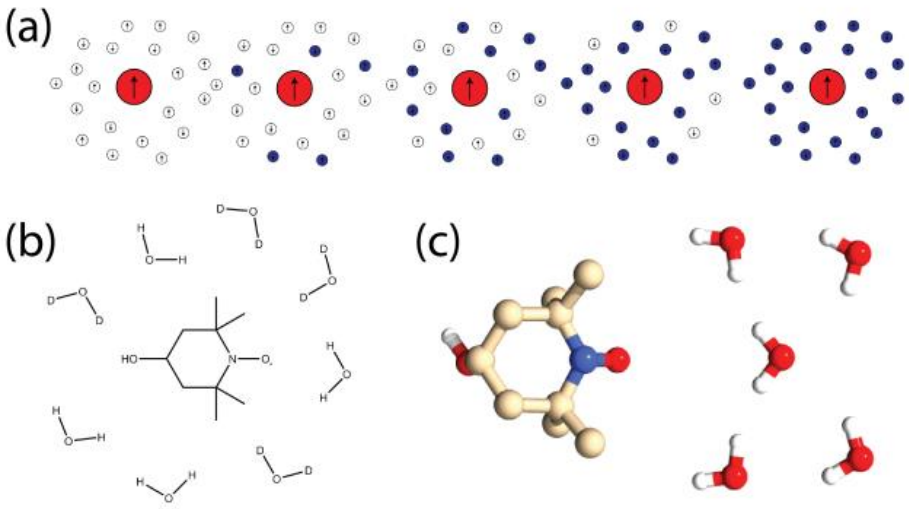

Figure 5.2 Simplified representations of model system, 4-hydroxy TEMPO in mixtures of H_2O/D_2O. (a) Pictorial representation of electron spin surrounded by protons (white) and deuterium (blue) (b) 4-hydroxy TEMPO structure surrounded by H_2O and D_2O (c) 3-dimensional structure of 4-hydroxy TEMPO molecule and water molecules.

i) ESEEM

The time-domain ESEEM traces for different D_2O concentrations gave identical shape, with different modulation depths. The modulation depth was approximately proportional to the concentration of D_2O, as has been shown in previous studies.[65] Each ESEEM trace was fit to the spherical shell model. The robustness of the spherical shell model relies on the first solvation shell contributing much more strongly to the ESEEM signal. Since the modulation depth for a given nuclei with fall off as $1/r^6$, the number of nuclei on a spherical shell increases with the radius of the shell as $4\pi r^2$ integrating over a sphere. For all concentrations of D_2O, the spherical shell model gave good agreement with data, indicating that the

assumption of a single spherical shell is reasonable. Figure 5.3 shows the fit of the spherical shell model for 50% D_2O (40% H_2O, 10% Glycerol). Note that in this work, we are only focusing on the matrix deuterium nuclei, since the much more strongly coupled hydrogen bonded deuterium requires incorporation of the quadrupolar interaction into the analysis. The fit is improved when an isotropic hyperfine coupling term is included, however, this is because the isotropic part of the hyperfine interaction has the same effect on the ESEEM signal as a weak quadrupolar interaction.[56]

As the D_2O concentration increases, we find that the modulation depth increases approximately linearly, as has been noted previously.[60,65] The number of nuclei and distance to the spherical shell for each concentration of D_2O is given in Figure 5.3. The number of deuterium nuclei increases linearly with concentration, which is expected based on the average density of deuterium nuclei. The distance to the spherical shell remains constant (Figure 5.3b). The distance to the spherical shell is based on a Van der Waals distance, which is not expected to change based on the density of D_2O.

ii) ODNP

The ODNP coupling factor is constant to within error at H_2O concentrations above 30% as shown in Figure 5.5a. Below 30% H_2O, the coupling factor decreases dramatically and approaches a value of zero. The coupling factor was corrected for differences in viscosity between H_2O and D_2O, which otherwise would lead to a 25% reduction in coupling factor. The dramatic decrease in coupling factor indicates that in the limit of very low proton density, the distance of closest approach must be replaced by an "effective" distance of closest approach, shown in Figure 5.5b. This new "effective" distance of closest approach is no longer the closest distance that the ^1H can approach the spin label, but the average

distance that the ^{1}H are allowed to approach the spin label. In this case, the coupling factor no longer becomes an indication purely of the dynamics of the water, but also measure of how closely the water molecules are allowed to approach the spin label.

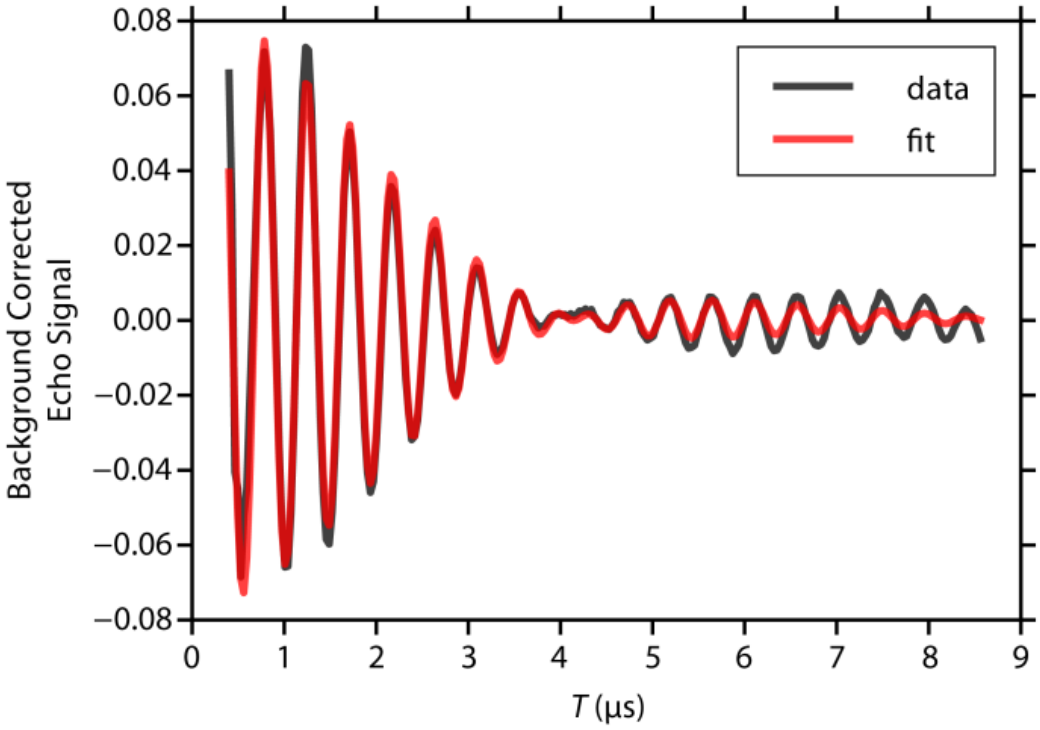

Figure 5.3 Fit of spherical shell model for 50% D_2O, 40% H_2O, and 10% glycerol. The fit (red) is quite good at short times, but deviates from the data (black) at longer times. The deviation is either caused by neglecting the quadrupolar interaction or not including more distant nuclei in the model.

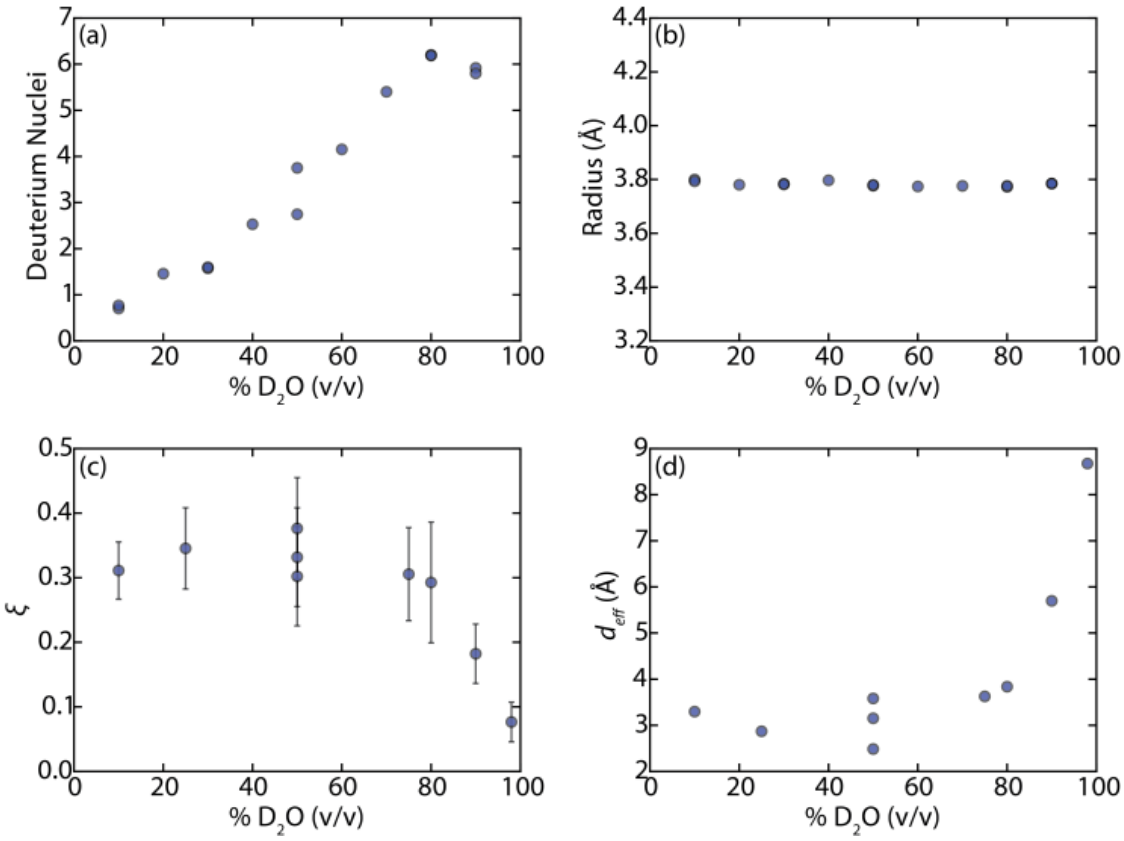

Figure 5.4 (a-b) Parameter from the ESEEM spherical shell model as a function of D_2O concentration. (a) Number of deuterium nuclei in solvation shell from assuming spherical shell. (b) Radius of spherical shell from spherical shell model. (c-d) ODNP parameters as a function of D_2O concentration. (c) Coupling factor determined from ODNP. (d) Effective distance of closest approach determined from coupling factor. To calculate the value of $\mathbf{d_{eff}}$ the diffusion coefficients of H_2O and spin label were chosen to be 2.3×10^{-9} $m^2 \cdot s^{-1}$ and 4.1×10^{-10} $m^2 \cdot s^{-1}$, respectively.

Table 5.1 ESEEM and ODNP parameters from surfaces

	N	τ (ps)
4-Carboxy TEMPO	6 ± 0.5	50 ± 10
Silica	3 ± 0.5	350 ± 10
Polystyrene	2 ± 0.5	300 ± 10

e) Discussion

The accessibility information from ESEEM is contained in both the modulation depth and the dampening of the ESEEM oscillations. An increase in the modulation depth (keeping distance constant), is correlated with an increase in number of deuterium nuclei, whereas increases in distance of matrix nuclei will have a pronounced impact on the rate the oscillations are dampened as well as modulation depth of the oscillations. Because the modulation depth is proportional to N/r^6, and the number of nuclei at a given radius increases with r^2, the overall effect on the modulation depth is $1/r^4$. This implies that modeling the data as a single spherical shell should account for >90% of all the ESEEM data.

Our values for the number of deuterium nuclei is approximately 7 deuterium nuclei at distance 3.8 Å from the electron spins in ~100% deuterated solution which would correspond to around 3.5 deuterated water molecules on average in the first solvation layer (excluding hydrogen bonded water). The distance of the spherical shell was consistently 3.8 Å and this corresponds reasonably well to the expected Van der Waals distance from the spin label to the water molecules. The distance also agrees with previous work using similar models.[55,57]

Unlike the ESEEM data, the coupling factor contains information about the dynamics as well as accessibility. The coupling factor is exclusively an indication of the dynamics as long as the concentration of protons is above 30%. As the concentration of protons is lowered below this value, the density of protons is so low that the distance of closest approach to the spin label must be replaced with an "effective" distance of closest approach which is no longer equal to the Van der Waals distance between the water molecules and the spin label. The "effective" distance of closest approach can be equivalently rationalized by an increase in the average distance between protons and spin label. As the number of protons approaches zero, the average distance between spin label and solvent protons increases; eventually, the probability that a proton will reside in the first solvation shell is lowered to a point where these protons have a negligible contribution to the coupling factor.

f) Conclusions

In summary, the two techniques we applied, ODNP and ESEEM, individually give information about accessibility, but combined can provide much moreprovide an additional layer of information where the accessibility and dynamics information can be obtained in conjunction.

In summary, we have applied two techniques, ODNP and ESEEM, to our model system of 4-hydroxy TEMPO in mixtures of H_2O and D_2O. Our results show that the ODNP coupling factor is highly independent of H_2O concentration above 30% H_2O (v/v). However, below 30% H_2O, the coupling factor alone cannot be used to reliably predict the translational correlation times of water. In this regime, it would be necessary to measure the water density by other means (e.g. with ESEEM) and calibrate the coupling factor to properly obtain a translational correlation time.

The number of deuterium nuclei extracted from the spherical shell model is linear as a function of D_2O concentration, which indicates it can function as a method for obtaining the hydration number around a spin label. An advantage of the ESEEM measurements is the high degree of precision with which the hydration number can be found. For the system studied, the spherical shell model gave very good agreement with data, although this may not be as applicable for buried or highly asymmetric samples. In these cases the modulation depth can still be related to obtain relative densities of water different sites when spherical shell model is not applicable.

Based on this study, we expect that for surface or other relatively exposed sites, the coupling factor will provide a reliable indication of the hydration dynamics. For sites that are buried, the coupling factor is no longer a reliable reflection of the translational correlation time, but primarily an indication of accessibility. Furthermore, ESEEM provides a means to obtain the hydration number for various sites around biomolecules.

6) Wavelet Denoising and SVD for Improved Pulsed EPR Distance Distributions

a) Tikhonov Regularization

Once we have obtained our DEER signal $V_{DEER}(t)$, we must convert this into a distance distribution $P(r)$. First the DEER signal is corrected to remove the background signal which comes from a homogenous distribution of spins throughout the sample. The background signal is given by:

$$B(t) = \exp\left(-kt^{d/3}\right) \tag{6.1}$$

where d is the dimensionality of the system (d = 3 for homogeneously distributed system) and k is a constant.

Once the background signal is removed, finding the distance distribution is equivalent to solving the equation for $P(r)$:

$$V(t) = \int_{R_{min}}^{R_{max}} K(r,t)\, P(r) dr \tag{6.2}$$

Where $K(r,t)$ is the kernel function which represents the ensemble average over all dipolar couplings for a given r. This problem takes the form of the Fredholm equation and is an example of an inverse problem.[72,73] Solving this problem is approached by discretizing $K(r,t)$ into a matrix and using an appropriate algorithm to find $P(r)$.

The problem in Eqn. 6.2 can be re-written in matrix form:

$$S = KP \tag{6.3}$$

Where S is the signal array. If we take the inverse of K, and multiply by both sides we obtain:

$$P = K^{-1}S \tag{6.4}$$

However, the solution to this problem depends strongly on the array S. In fact as shown in Figure 6.1, while the inverse gives a high quality time domain fit, even a small amount of noise produces an oscillatory distance distribution which doesn't make physical sense.

One method of solving ill-posed problems is Tikhonov regularization.[74,75] This is a common method for obtaining distance distributions from DEER. Tikhonov regularization assumes that the underlying distribution must be smooth. A regularization parameter determines the smoothness of the solution and therefore acts as a low pass filter. As shown in Figure 6.1, the Tikhonov regularization time domain fit, now is a much better representation of the data and produces the same mean distance as the exact solution.

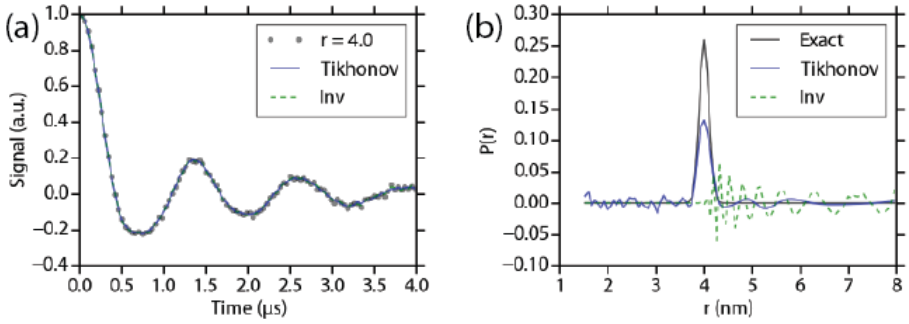

Figure 6.1 Simulated data to demonstrate the inverse problem. (a) Fit obtained by multiplying the inverse kernel and the signal array (dashed green) and Tikhonov regularization (blue). (a) Distance distributions obtained by corresponding distance distribution.

Alternatively, a model based fit (e.g. Gaussian) can also be used, particularly in cases with broad distance distributions as well as limited SNR. The advantage of model-based fit is the ability to obtain error-bars on fits. Several software packages exist to model DEER data including DeerAnalysis[72,73], LongDistances, and DEFit.

b) Wavelet Denoising

Even with the signal to noise improvements from arbitrarily shaped pulses and other methods of optimization, some of the most significant DEER experiments are very difficult if not impossible without averaging for unreasonable amounts of time. A significant example of this is "seeded" tau fibrils, where aggregation is induced using fibrils extracted from mouse brain. Because of the limited amount of sample, broad distance distribution, and short T_2 times, averaging for > 48 hours can produce poor quality data.

Recently developed wavelet denoising techniques[76] have the potential of allowing a new range of possible experiments either with reduced protein concentrations or greater accessible distance ranges.[77]

c) Validation of Wavelet Denoising

For DEER data with high SNR, the results from denoising and the results from standard Tikhonov regularization of the raw data are expected to be the same. This is validated in Figure 6.2. The more interesting cases occur where SNR is highly limited.

To test cases of limited SNR, DEER data is taken from a system with a distance distribution obtained to a high degree of certainty by averaging a large number of times and compare the results to denoising the same sample with far less averages. As can be seen from Figure 6.3, when the signal to noise level is particularly low, the tendency is to generate narrow peaks. This is a very difficult case where the distance distribution is broad and the dipolar evolution is only acquired out to 2 us.

The denoising method performs much better in the case of a standard ruler Figure 6.4, where the distance distribution is very narrow and significantly longer dipolar evolution

times can be measured. In this case, a peak is observed at the correct distance of 4.1 nm, however, the peak is not visible in the raw data.

It must also be noted that in order for the denoising method to work, a large enough number of samples must be taken to obtain good statistics. It could be argued in the case of Figure 6.3 that one of the primary reasons the denoising distance distribution differed from the "accepted" distance distribution was the limited number of points in the time domain data.

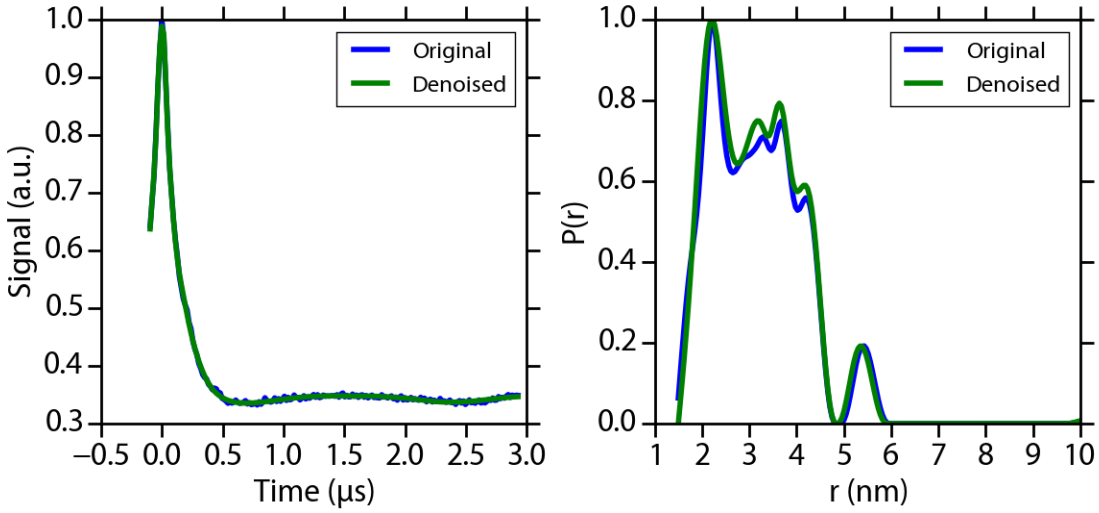

Figure 6.2 Tau 272/285 before aggregation with good SNR to demonstrate reliability of distance distributions after denoising.

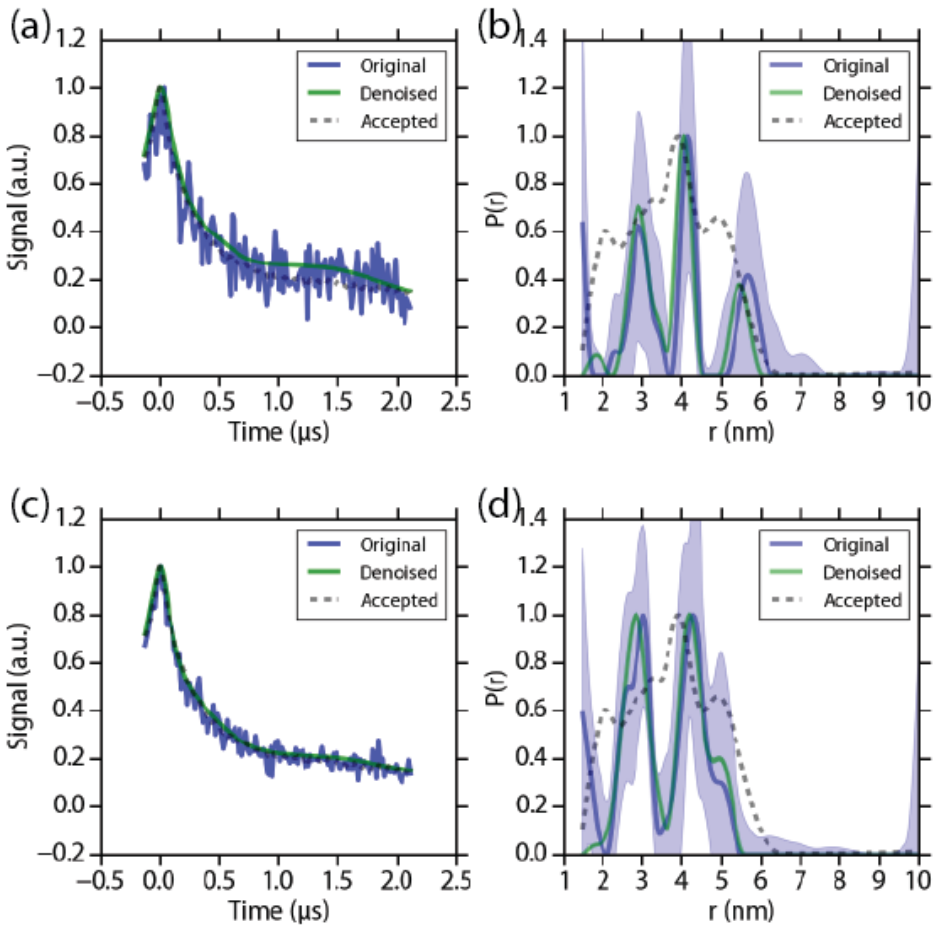

Figure 6.3 Tau 272/285 demonstrating the denoising method and using Tikhonov regularization to obtain distance distributions.

d) Details about background correction

LongDistances software uses Tikhonov regularization to aid in fitting the background signal. A cutoff distance is chosen, above which the distance distribution is forced to be near zero. I'm not sure exactly how the cutoff distance is chosen, but it is somehow based on the dipolar evolution time. The concept behind this is that the background correction is indistinguishable from longer distances in the distribution, so it will just set all the long distances to zero and model the background function assuming a generic distance distribution obtained from Tikhonov regularization.

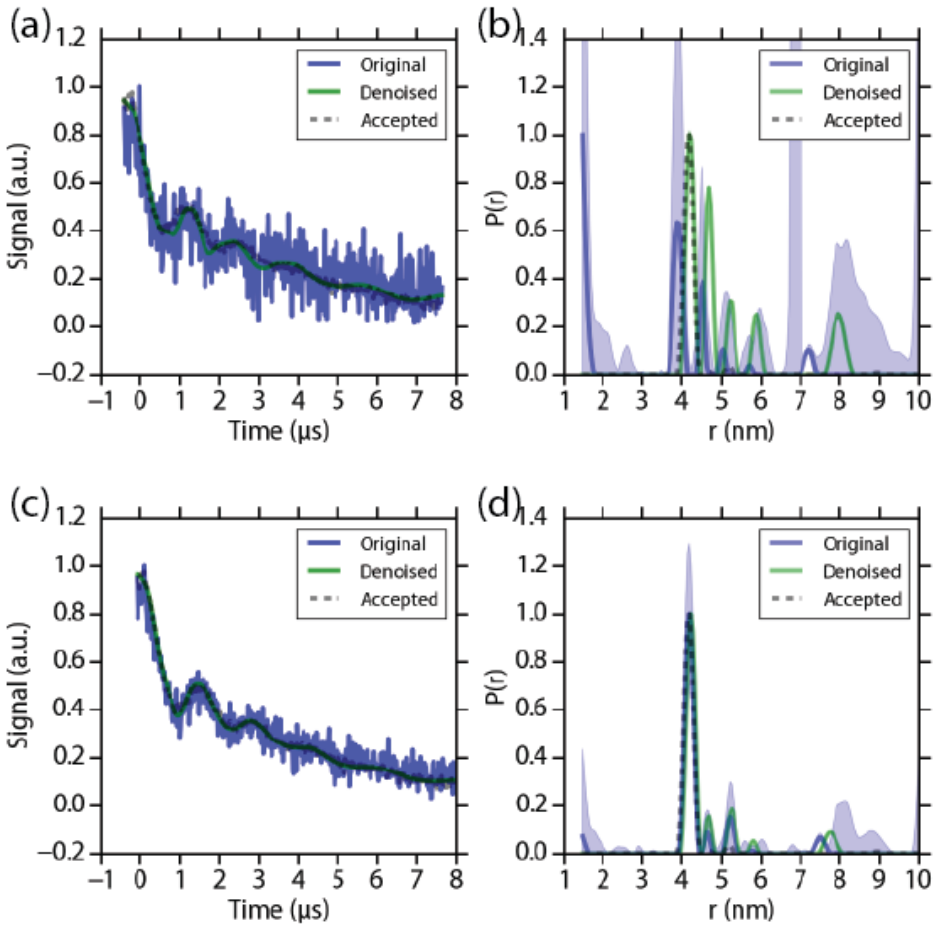

Figure 6.4 Standard ruler molecule (4.1 nm) showing the time domain data (a) and distance distribution (b) for 1 average (top) and 5 averages (bottom).

This method is more sophisticated than that performed by DeerAnalysis, where the background function is fit using a user specified range of values where the baseline is assumed to be the dominant contributing factor to the signal. Both of these methods will obviously distort distances above a certain threshold in the distribution because they are indistinguishable from background.

What is less obvious is that the background function can also shift the position of shorter distances in the distribution. For distributions which are both broad and short, the most

relevant information from the DEER trace is contained in the initial slope of the DEER signal. If the background function is not reliable, it can shift the position of a peak. For example, if the slope of the background is too great near time zero, it will shift the peak to longer distances.

Prior to performing DEER, the dipolar evolution time required to measure the longest desired distance should be considered. In the ideal case, the solution would be to simply measure DEER with longer maximum dipolar evolution time. For cases with poor SNR, this is not possible. In these cases, one could potentially measure DEER with two different maximum dipolar evolution times, using the long dipolar evolution time for a background correction and the short dipolar evolution time to calculate the distance distribution. It may also be possible to improve the SNR by only measuring 3-pulse DEER when determining the background (because there is one less 180-pulse and less loss in delay times).

e) Introduction to SVD based PICASSO Method

Singular value decomposition is a technique for decomposing a matrix into a set of orthonormal basis vectors. A new method for determining the distance distribution from using SVD. This method, which has been termed Piccard Sliding Scale Optimized (PICASSO), decomposes the Kernel into basis vectors and uses an eigenvalue cutoff to construct the distance distribution. For data with noise, this method would not work, but in conjunction with the wavelet denoising, it is possible to obtain distance distributions from this method. In addition, it is possible to estimate the error in the fitting by a method with Piccard plots. This new method has been termed

In Figure 6.5 and Figure 6.6, the distance distributions obtained by the SVD based method PICASSO are shown. There are a few observations about the distance distributions.

Certain artifacts will result in certain features in the distance distribution. For example, a "peak" or "oscillation" which occurs at the end of the DEER trace is not a physical property of the DEER traces. Therefore, the observed oscillations in the distance distribution to compensate for the non-physical features in the time-domain data. The solution will not be able to produce the correct result, so instead it will constructively and destructively add parts of the kernel to reconstruct the time-domain data. The primary advantage of the SVD method is that there is no assumption about the smoothness of the distance distribution as there is in Tikhonov regularization. This is a major advantage if the distance distributions have a large amount of structure, or it can have a distance distribution with multiple peaks that have different widths.

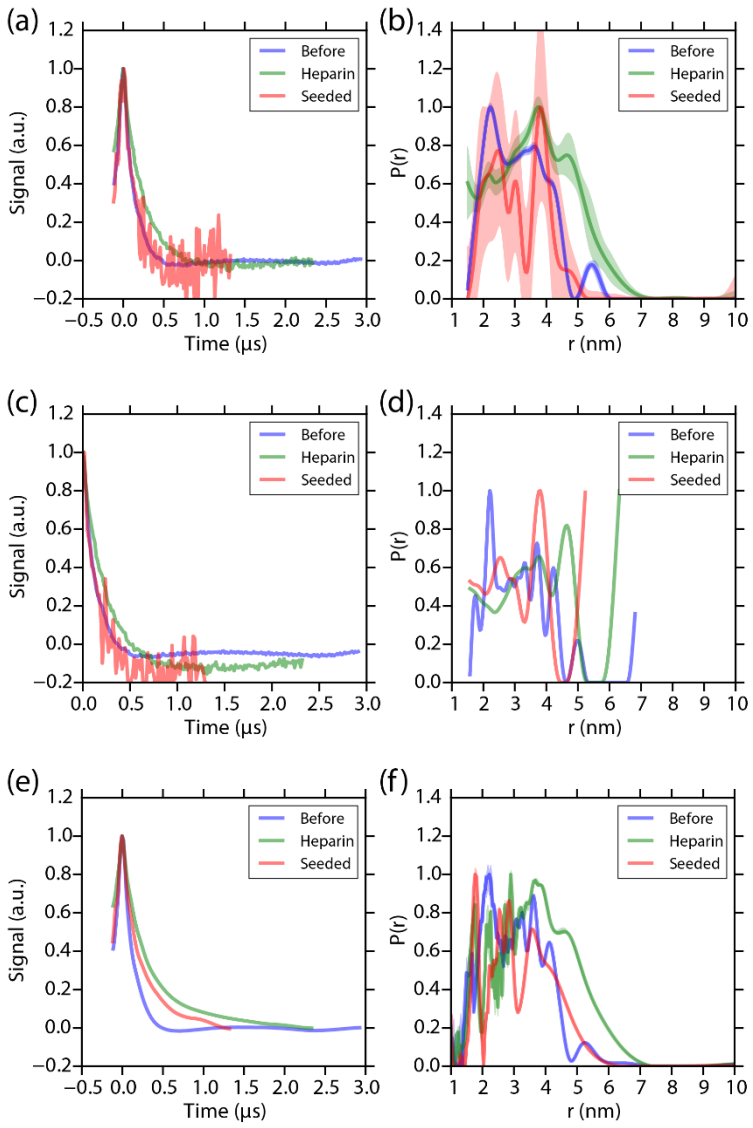

Figure 6.5 Tau protein 272/285 before aggregation, after aggregation with heparin, and after aggregation with seeded fibrils. Time-domain background corrected DEER data (left column) and distance distributions (right column) obtained by processing with LongDistances software (a-b), DeerAnalysis software (c-d), and the WavPDS (e-f).

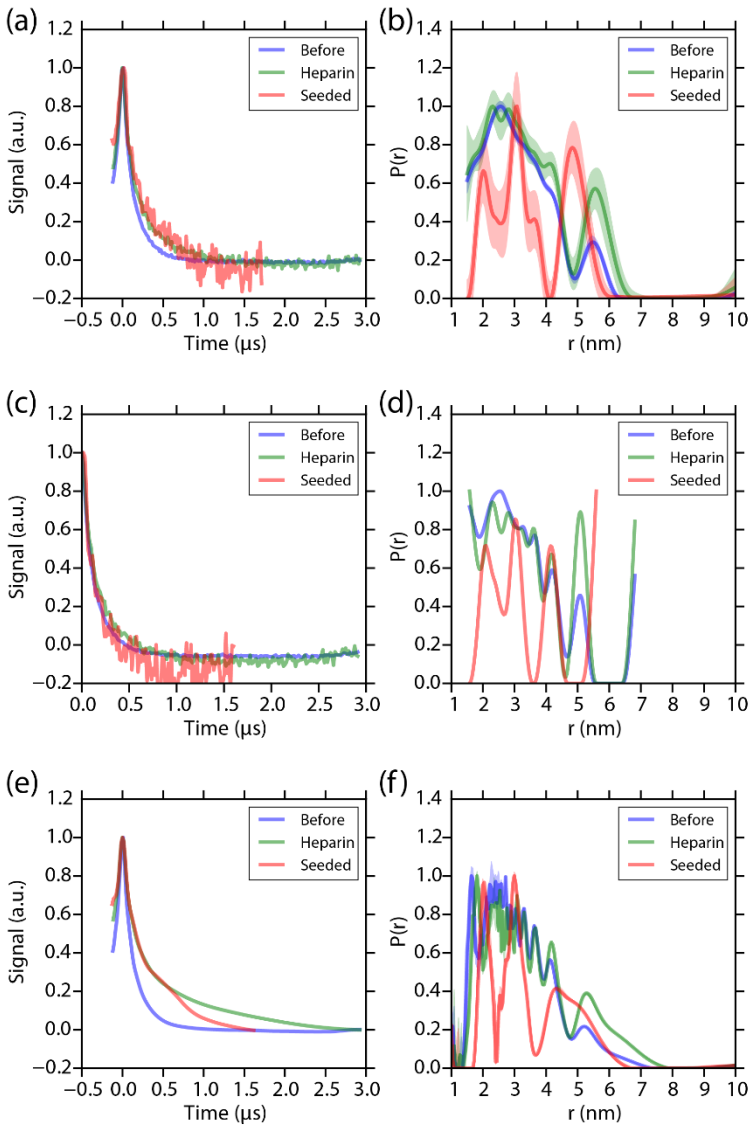

Figure 6.6 Tau protein 351/373 before aggregation, after aggregation with heparin, and after aggregation with seeded fibrils. Time-domain background corrected DEER data (left column) and distance distributions (right column) obtained by processing with LongDistances software (a-b), DeerAnalysis software (c-d), and the WavPDS (e-f).

f) Conclusion

Our investigations of the wavelet denoising and PICASSO analysis show initial promising results. Ideally, all the noise in an experiment is distributed normally, however, in certain cases where there is systematic noise or non-uniformly distributed noise throughout the DEER trace, the denoising method cannot be expected to produce the correct result. The quality of the denoising analysis can be improved by averaging long enough to ensure good statistics so that the noise is distributed normally about the mean as well as increasing the number of data points in the DEER trace. The number of data points is significant because if a single point is an outlier, it will contribute more significantly in a DEER trace with less points. In this sense, the points before and after an outlier can act as validation that this point should be excluded or regarded as less significant.

While initially promising, the wavelet denoising method must be performed and validated to ensure the correct result is produced. One of the main applications of the wavelet denoising method and PICASSO is that it can be used in cases to decide if further investigation is warranted. For example, if proposing to study a particular protein, but lack the resources to produce it in large quantities, it is possible to perform DEER with limited SNR and use denoising to obtain a result. If the result is interesting, one can argue that further investment of time and resources is justified.

More work must be done to validate the error bars of the PICASSO analysis and additional circumstances should be tested to determine the limits of the denoising and PICASSO methods.

7. Conclusion

As pulse shaping capabilities are expanded into the field of EPR the shear potential of feasible experiments is vastly expanded. It adds an entirely new dimension to the landscape of pulsed EPR which must be carefully and precisely investigated to determine the benefits and limitations of this newly developed technology. Any experiment which incorporates broadband pulses or selective pulses can immediately benefit from shaped pulses in a straightforward manner. The pulse desired to be more broadband/selective is exchanged with a pulse designed for the application. The challenge begins when one has an enormous library of potential pulse shapes and investigating what pulse shape produces the most optimal result for each scenario. In addition, the complication of pulse distortion by the microwave resonator must be considered in some form to ensure the actual pulse shape produced by the microwave hardware is being considered instead of an “ideal” pulse shape programmed by the experimenter.

In this work, the development of a first of its kind home-build DAC board-based AWG EPR spectrometer is described. The spectrometer demonstrates unprecedented fidelity and precision is exciting spin systems even in the presence of a resonator transfer function. The resonator transfer function can be experimentally determined and pulses can be calibrated so that they compensate for the distortions caused by the transfer function. Experiments first performed with a 10 W solid-state amplifier are validated again at higher power with a 1 kW TWT amplifier. The TWT amplifier dramatically reduced the noise during acquisition and enabled our spectrometer to be highly competitive with state-of-the-art commercial spectrometers.

The optimization and calibration of pulse shapes was demonstrated for both DEER and SIFTER distance measurements at X-band, where the benefits of calibrating for resonator transfer function become apparent for SIFTER. Calibration of the pump pulse is less relevant for DEER; however, shaped pulses still offer an improved modulation depth of approximately a factor of 2. The potential for SIFTER is great because it produces better signal to noise than DEER for the cases investigated, however, the artifacts in SIFTER caused by ESEEM inhibit one from currently applying SIFTER to realistic protein samples. Once the ESEEM artifact is suppressed, it is possible for SIFTER to replace DEER in many cases.

It is well known that Q-band DEER measurements offer superior signal to noise to X-band DEER measurements. To further improve the potential for the most challenging protein samples, the investigation was extended to optimization of DEER at Q-band. Various tuning procedures and pump pulses were investigated to optimize the DEER experiment. A tuning protocol with 180 MHz mode separation and 200 ns chirp pulse were shown to produce the most optimized Q-band DEER measurements.

The water accessibility measurements of ODNP and ESEEM can be used in conjunction to simultaneously measure both the translational diffusion and number of water molecules around a spin label of interest. ODNP offers a reliable indicator of the water dynamics until the water layer is significantly depleted around the spin label by more than 70%. This indicates that the dynamical properties of biological water around proteins can be measured by ODNP and the accessibility can be measured by ESEEM where each offer a complementary picture of the local water structure and dynamics.

The improvements in hardware and experimental design are coupled with developments in data processing where wavelet denoising and the SVD based PICASSO method are used to further optimize the measurement of distance distributions from pulsed dipolar spectroscopy data. The PICASSO method showed promise with its ability to determine a distance distribution without the assumption of smoothness used in the case of Tikhonov regularization, but further investigation of PICASSO is necessary to validate this method as a reliable replacement for Tikhonov regularization.

References

1. Poole, C. P. *Electron Spin Resonance*. (John Wiley & Sons, Inc, 1983).
2. Chang, K. *Microwave Solid-State Circuits and Applications*. (John Wiley & Sons, Inc, 1994).
3. Weil, J. A. & Bolton, J. R. *Electron Paramagnetic Resonance*. (John Wiley & Sons, Inc, 2007).
4. Schweiger, A. & Jeschke, G. *Principles of pulse electron paramagnetic resonance*. (Oxford University Press, 2001).
5. Ikeya, M. Use of Electron Spin Resonance Spectrometry in Microscopy, Dating and Dosimetry A Review. *Anal. Sci.* **5,** 5–12 (1989).
6. Barriga-González, G. *et al.* Spin trapping: an essential tool for the study of diseases caused by oxidative stress. *Curr. Top. Med. Chem.* **15,** 484–495 (2015).
7. Ahmad, R. & Kuppusamy, P. Theory, Instrumentation, and Applications of EPR Oximetry. *Chem. Rev.* **110,** 3212–3236 (2010).
8. Mchaourab, H. S., Steed, P. R. & Kazmier, K. Toward the Fourth Dimension of Membrane Protein Structure: Insight into Dynamics from Spin-Labeling EPR Spectroscopy. *Structure* **19,** 1549–1561 (2011).
9. Jeschke, G. DEER Distance Measurements on Proteins. *Annu. Rev. Phys. Chem.* **63,** 419–446 (2012).
10. Stoll, S. & Kasumaj, B. Phase Cycling in Electron Spin Echo Envelope Modulation. *Appl. Magn. Reson.* **35,** 15–32 (2008).
11. Gemperle, C., Aebli, G., Schweiger, A. & Ernst, R. R. Phase cycling in pulse EPR. *J. Magn. Reson. 1969* **88,** 241–256 (1990).

12. Kaufmann, T. *et al.* DAC-board based X-band EPR spectrometer with arbitrary waveform control. *J. Magn. Reson.* **235,** 95–108 (2013).

13. Doll, A., Pribitzer, S., Tschaggelar, R. & Jeschke, G. Adiabatic and fast passage ultra-wideband inversion in pulsed EPR. *J. Magn. Reson.* **230,** 27–39 (2013).

14. Garwood, M. & DelaBarre, L. The Return of the Frequency Sweep: Designing Adiabatic Pulses for Contemporary NMR. *J. Magn. Reson.* **153,** 155–177 (2001).

15. Hwang, T.-L., van Zijl, P. C. M. & Garwood, M. Fast Broadband Inversion by Adiabatic Pulses. *J. Magn. Reson.* **133,** 200–203 (1998).

16. Spindler, P. E., Glaser, S. J., Skinner, T. E. & Prisner, T. F. Broadband Inversion PELDOR Spectroscopy with Partially Adiabatic Shaped Pulses. *Angew. Chem. Int. Ed.* **52,** 3425–3429 (2013).

17. Spindler, P. E. *et al.* Shaped optimal control pulses for increased excitation bandwidth in EPR. *J. Magn. Reson.* **218,** 49–58 (2012).

18. Spindler, P. E. *et al.* Carr–Purcell Pulsed Electron Double Resonance with Shaped Inversion Pulses. *J. Phys. Chem. Lett.* **6,** 4331–4335 (2015).

19. Garwood, M. & Uğurbil, K. B1 Insensitive Adiabatic RF Pulses. in *In-Vivo Magnetic Resonance Spectroscopy I: Probeheads and Radiofrequency Pulses Spectrum Analysis* (ed. Rudin, M.) 109–147 (Springer Berlin Heidelberg, 1992). doi:10.1007/978-3-642-45697-8_4

20. Spindler, P. E., Schöps, P., Bowen, A. M., Endeward, B. & Prisner, T. F. Shaped Pulses in EPR. in *eMagRes* (John Wiley & Sons, Ltd, 2007). doi:10.1002/9780470034590.emrstm1520

21. Devasahayam, N. *et al.* Tailored sinc pulses for uniform excitation and artifact-free radio frequency time-domain EPR imaging. *J. Magn. Reson.* **168,** 110–117 (2004).

22. Tait, C. E. & Stoll, S. ENDOR with band-selective shaped inversion pulses. *J. Magn. Reson.* **277,** 36–44 (2017).

23. Rinard, G. A., Quine, R. W., Song, R., Eaton, G. R. & Eaton, S. S. Absolute EPR Spin Echo and Noise Intensities. *J. Magn. Reson.* **140,** 69–83 (1999).

24. Hoult, D. I. & Richards, R. E. The signal-to-noise ratio of the nuclear magnetic resonance experiment. *J. Magn. Reson. 1969* **24,** 71–85 (1976).

25. Borneman, T. W. & Cory, D. G. Bandwidth-limited control and ringdown suppression in high-Q resonators. *J. Magn. Reson.* **225,** 120–129 (2012).

26. Jeschke, G. & Polyhach, Y. Distance measurements on spin-labelled biomacromolecules by pulsed electron paramagnetic resonance. *Phys. Chem. Chem. Phys.* **9,** 1895–1910 (2007).

27. Pannier, M., Veit, S., Godt, A., Jeschke, G. & Spiess, H. W. Dead-Time Free Measurement of Dipole–Dipole Interactions between Electron Spins. *J. Magn. Reson.* **142,** 331–340 (2000).

28. Jeschke, G., Pannier, M., Godt, A. & Spiess, H. W. Dipolar spectroscopy and spin alignment in electron paramagnetic resonance. *Chem. Phys. Lett.* **331,** 243–252 (2000).

29. Borbat, P. P. & Freed, J. H. Double-Quantum ESR and Distance Measurements. in *Distance Measurements in Biological Systems by EPR* 383–459 (Springer, Boston, MA, 2002). doi:10.1007/0-306-47109-4_9

30. Polyhach, Y. *et al.* High sensitivity and versatility of the DEER experiment on nitroxide radical pairs at Q-band frequencies. *Phys. Chem. Chem. Phys.* **14,** 10762–10773 (2012).

31. Kaminker, I., Barnes, R. & Han, S. Arbitrary waveform modulated pulse EPR at 200GHz. *J. Magn. Reson.* **279,** 81–90 (2017).

32. Bahrenberg, T. *et al.* Improved sensitivity for W-band Gd(III)-Gd(III) and nitroxide-nitroxide DEER measurements with shaped pulses. *J. Magn. Reson.* **283,** 1–13 (2017).

33. Denysenkov, V., Os, P. van & Prisner, T. F. Q-Band Loop-Gap Resonator for EPR Applications with Broadband-Shaped Pulses. *Appl. Magn. Reson.* 1–10 (2017). doi:10.1007/s00723-017-0930-9

34. Borbat, P. P., Georgieva, E. R. & Freed, J. H. Improved Sensitivity for Long-Distance Measurements in Biomolecules: Five-Pulse Double Electron–Electron Resonance. *J. Phys. Chem. Lett.* **4,** 170–175 (2013).

35. Schweiger, A. & Jeschke, G. *Principles of Pulse Electron Paramagnetic Resonance*. (Oxford University Press, 2001).

36. Weil, J. A. & Bolton, J. R. *Electron Paramagnetic Resonance: Elementary Theory and Practical Applications*. (John Wiley & Sons, 2007).

37. Fichou, Y., Eschmann, N. A., Keller, T. J. & Han, S. Chapter 5 - Conformation-based assay of tau protein aggregation. in *Methods in Cell Biology* (eds. Feinstein, S. C. & LaPointe, N. E.) **141,** 89–112 (Academic Press, 2017).

38. Tait, C. E. & Stoll, S. Coherent pump pulses in Double Electron Electron Resonance Spectroscopy. *Phys. Chem. Chem. Phys.* (2016). doi:10.1039/C6CP03555H

39. Bechhoefer, J. Kramers-Kronig, Bode, and the meaning of zero. *Am. J. Phys.* **79,** 1053–1059 (2011).

40. Schöps, P., Spindler, P. E., Marko, A. & Prisner, T. F. Broadband spin echoes and broadband SIFTER in EPR. *J. Magn. Reson.* **250,** 55–62 (2015).

41. Ball, P. Water as an Active Constituent in Cell Biology. *Chem. Rev.* **108,** 74–108 (2008).

42. Pal, S. K., Peon, J., Bagchi, B. & Zewail, A. H. Biological Water: Femtosecond Dynamics of Macromolecular Hydration. *J. Phys. Chem. B* **106,** 12376–12395 (2002).

43. Nandi, N. & Bagchi, B. Dielectric Relaxation of Biological Water. *J. Phys. Chem. B* **101,** 10954–10961 (1997).

44. Oleinikova, A., Sasisanker, P. & Weingärtner, H. What Can Really Be Learned from Dielectric Spectroscopy of Protein Solutions? A Case Study of Ribonuclease A. *J. Phys. Chem. B* **108,** 8467–8474 (2004).

45. Vinh, N. Q., Allen, S. J. & Plaxco, K. W. Dielectric Spectroscopy of Proteins as a Quantitative Experimental Test of Computational Models of Their Low-Frequency Harmonic Motions. *J. Am. Chem. Soc.* **133,** 8942–8947 (2011).

46. Otting, G. NMR studies of water bound to biological molecules. *Prog. Nucl. Magn. Reson. Spectrosc.* **31,** 259–285 (1997).

47. Conti Nibali, V. & Havenith, M. New Insights into the Role of Water in Biological Function: Studying Solvated Biomolecules Using Terahertz Absorption Spectroscopy in Conjunction with Molecular Dynamics Simulations. *J. Am. Chem. Soc.* **136,** 12800–12807 (2014).

48. Pal, S. K., Peon, J. & Zewail, A. H. Biological water at the protein surface: Dynamical solvation probed directly with femtosecond resolution. *Proc. Natl. Acad. Sci.* **99,** 1763–1768 (2002).

49. Levy, Y. & Onuchic, J. N. Water mediation in protein folding and molecular recognition. *Annu. Rev. Biophys. Biomol. Struct.* **35,** 389–415 (2006).

50. Cheng, C.-Y., Varkey, J., Ambroso, M. R., Langen, R. & Han, S. Hydration dynamics as an intrinsic ruler for refining protein structure at lipid membrane interfaces. *Proc. Natl. Acad. Sci.* **110,** 16838–16843 (2013).

51. Jao, C. C., Hegde, B. G., Chen, J., Haworth, I. S. & Langen, R. Structure of membrane-bound α-synuclein from site-directed spin labeling and computational refinement. *Proc. Natl. Acad. Sci.* **105,** 19666–19671 (2008).

52. Song, J., Allison, B. & Han, S. Local water diffusivity as a molecular probe of surface hydrophilicity. *MRS Bull.* **39,** 1082–1088 (2014).

53. Franck, J. M., Pavlova, A., Scott, J. A. & Han, S. Quantitative cw Overhauser effect dynamic nuclear polarization for the analysis of local water dynamics. *Prog. Nucl. Magn. Reson. Spectrosc.* **74,** 33–56 (2013).

54. Armstrong, B. D. & Han, S. A new model for Overhauser enhanced nuclear magnetic resonance using nitroxide radicals. *J. Chem. Phys.* **127,** 104508 (2007).

55. Volkov, A., Dockter, C., Bund, T., Paulsen, H. & Jeschke, G. Pulsed EPR Determination of Water Accessibility to Spin-Labeled Amino Acid Residues in LHCIIb. *Biophys. J.* **96,** 1124–1141 (2009).

56. Kevan, L. & Schwartz, R. *Time Domain Electron Spin Resonance*. (John Wiley & Sons, Inc, 1979).

57. Ichikawa, T., Kevan, L., Bowman, M. K., Dikanov, S. A. & Tsvetkov, Y. D. Ratio analysis of electron spin echo modulation envelopes in disordered matrices and application to the structure of solvated electrons in 2-methyltetrahydrofuran glass. *J. Chem. Phys.* **71,** 1167–1174 (1979).

58. Hoogstraten, C. G. & Britt, R. D. Water counting: Quantitating the hydration level of paramagnetic metal ions bound to nucleotides and nucleic acids. *RNA* **8,** 252–260 (2002).

59. Deligiannakis, Y., Louloudi, M. & Hadjiliadis, N. Electron spin echo envelope modulation (ESEEM) spectroscopy as a tool to investigate the coordination environment of metal centers. *Coord. Chem. Rev.* **204,** 1–112 (2000).

60. Erilov, D. A. *et al.* Water Concentration Profiles in Membranes Measured by ESEEM of Spin-Labeled Lipids. *J. Phys. Chem. B* **109,** 12003–12013 (2005).

61. Carmieli, R. *et al.* Utilizing ESEEM Spectroscopy to Locate the Position of Specific Regions of Membrane-Active Peptides within Model Membranes. *Biophys. J.* **90,** 492–505 (2006).

62. Franck, J. M. *et al.* Probing Water Density and Dynamics in the Chaperonin GroEL Cavity. *J. Am. Chem. Soc.* **136,** 9396–9403 (2014).

63. Cieslak, J. A., Focia, P. J. & Gross, A. Electron Spin-Echo Envelope Modulation (ESEEM) Reveals Water and Phosphate Interactions with the KcsA Potassium Channel,. *Biochemistry (Mosc.)* **49,** 1486–1494 (2010).

64. Lai, Y.-C., Chen, Y.-F. & Chiang, Y.-W. ESR Study of Interfacial Hydration Layers of Polypeptides in Water-Filled Nanochannels and in Vitrified Bulk Solvents. *PLOS ONE* **8,** e68264 (2013).

65. Milov, A. D., Samoilova, R. I., Shubin, A. A., Grishin, Y. A. & Dzuba, S. A. ESEEM Measurements of Local Water Concentration in D2O-Containing Spin-Labeled Systems. *Appl. Magn. Reson.* **35,** 73–94 (2008).

66. Türke, M.-T. & Bennati, M. Saturation factor of nitroxide radicals in liquid DNP by pulsed ELDOR experiments. *Phys. Chem. Chem. Phys.* **13,** 3630–3633 (2011).

67. Hausser, K. H. & Stehlik, D. Dynamic Nuclear Polarization in Liquids. in *Advances in Magnetic and Optical Resonance* (ed. Waugh, J. S.) **3,** 79–139 (Academic Press, 1968).

68. Freed, J. H. Dynamic effects of pair correlation functions on spin relaxation by translational diffusion in liquids. II. Finite jumps and independent T1 processes. *J. Chem. Phys.* **68,** 4034–4037 (1978).

69. Hwang, L. & Freed, J. H. Dynamic effects of pair correlation functions on spin relaxation by translational diffusion in liquids. *J. Chem. Phys.* **63,** 4017–4025 (1975).

70. Akdogan, Y. *et al.* Intrinsic Surface-Drying Properties of Bioadhesive Proteins. *Angew. Chem. Int. Ed.* **53,** 11253–11256 (2014).

71. Armstrong, B. D. *et al.* Portable X-band system for solution state dynamic nuclear polarization. *J. Magn. Reson.* **191,** 273–281 (2008).

72. Hansen, P. C. Numerical tools for analysis and solution of Fredholm integral equations of the first kind. *Inverse Probl.* **8,** 849 (1992).

73. Hansen, P. Analysis of Discrete Ill-Posed Problems by Means of the L-Curve. *SIAM Rev.* **34,** 561–580 (1992).

74. Chiang, Y.-W., Borbat, P. P. & Freed, J. H. The determination of pair distance distributions by pulsed ESR using Tikhonov regularization. *J. Magn. Reson. San Diego Calif 1997* **172,** 279–295 (2005).

75. Chiang, Y.-W., Borbat, P. P. & Freed, J. H. Maximum entropy: A complement to Tikhonov regularization for determination of pair distance distributions by pulsed ESR. *J. Magn. Reson.* **177,** 184–196 (2005).

76. A New Wavelet Denoising Method for Selecting Decomposition Levels and Noise Thresholds - IEEE Journals & Magazine. Available at: https://ieeexplore.ieee.org/document/7505903/. (Accessed: 19th September 2018)

77. Srivastava, M., Georgieva, E. R. & Freed, J. H. A New Wavelet Denoising Method for Experimental Time-Domain Signals: Pulsed Dipolar Electron Spin Resonance. *J. Phys. Chem. A* **121,** 2452–2465 (2017).